LAND COVER/USE CHANGE AND CHANGE PATTERN DETECTION USING RADAR AND OPTICAL IMAGES : AN INSTANCE OF URBAN ENVIRONMENT(Dissertation_全文)

AUTHOR(S):

Bhogendra Mishra

LAND COVER/USE CHANGE AND CHANGE PATTERN DETECTION USING RADAR AND OPTICAL IMAGES: AN INSTANCE OF URBAN ENVIRONMENT

Bhogendra Mishra

2014

LAND COVER/USE CHANGE AND CHANGE PATTERN DETECTION USING RADAR AND OPTICAL IMAGES: AN INSTANCE OF URBAN ENVIRONMENT

By

Bhogendra Mishra

A dissertation submitted in partial fulfillment of the requirements for the degree of Doctor of Philosophy

Examination Committee: Dr. Junichi Susaki (Chairperson)
Prof. Masayuki Tamura
Prof. Katsuaki Koike

Department of Civil and Earth Resources Engineering
Graduate School of Engineering
Kyoto University, Japan
2014

I dedicate this research effort, the crop of my thoughts, to my parents and family.

Bhogendra Mishra

ACKNOWLEDGEMENTS

I am indebted to my dissertation advisor Dr. Junichi Susaki, for his assiduous effort on guiding me during my dissertation research. Without his support, my doctoral study would not have been so precious. I have gained inestimable experiences with him that will guide me throughout my future endeavors. I would like to express my heartfelt thanks to Prof. Masayuki Tamura, co-chair of the dissertation committee, for his valuable ideas, constructive criticism, constant motivation, and suggestions to keep track this dissertation. Similarly, my sincerely thanks to Prof. Katsuaki Koike for being on my committee and his insightful comments and suggestions to improve the dissertation.

I would like to express my wholehearted thanks to the staff of the Kyoto University, Graduate School of Engineering, Department of Civil and Earth Resources Engineering, Geoinformatics laboratory for their help and for providing the splendid environment in the lab and supports. Similarly, my sincere gratitude goes to all fellows, friends and colleagues for their kind suggestions and supports throughout my research.

I would like to extend my sincere thanks to the Japanese Government for providing the Monbukagakusho (MEXT) Scholarship during my study at Kyoto University, without this support, it would not be possible.

My unlimited gratefulness goes to my parents. I would never have completed my research without love and inspiration from my father, Hari Nath Mishra, and mother, Surya Devi Mishra. I dedicate this work to them. I must express my deep gratitude to my wife, Shobha Poudel. Her love and continues support has been a driving force of my research. Finally, thanks to my family for their encouragement, inspiration and moral support to make me successful.

EXECUTIVE SUMMARY

Change detection is the process of identifying differences in the state of an object or phenomenon in the earth's surface by observing it at different times. Primarily, it needs the ability to quantify temporal effects using multi-temporal data sets. Because of the availability of the image in a regular interval and consistent image quality, the imageries acquired by the Earth-orbiting satellite are being used for detecting changes such as land change analysis, urban extension mapping and monitoring, crop monitoring, assessment of deforestation, the study of the seasonal vegetation changes, disaster monitoring, tracking the glacier and snow cover dynamics and other environmental changes etc.

In case of optical images, the basic premise in using remote sensing data for change detection is that changes in land cover must result in changes in reflectance values and changes in reflectance due to land cover change must be large with respect to reflectance changes caused by other factors. However, in the case of the Synthetic Aperture Radar (SAR) images, it is the result of changes in backscatter and changes in the backscatter value due to the land cover change must be larger with respect to the changes in backscatter caused by other factors.

Optical images have already seen very effective for the diverse types of changes, however, due to its inherent shortcoming, light and cloud condition, limits the image availability significantly in several parts of the world. Thus, as an alternative, SAR images have attracted a greater attention in the remote sensing community with its operational advantage of all-time, all weather capacity.

Currently, mainly three types of change detection procedures are in practice, namely, binary change detection, multi-class change detection and change detection in long time series of images. For the binary change detection, several supervised and unsupervised methods for multi-temporal optical, SAR or fusion of both images have been developed and published in several journal articles. However, several problems are there need to address for better change and change pattern detection. Therefore, this thesis focuses on solving such problems while using SAR images, PolSAR images and the fusion of SAR and optical images in urban environments.

In the context of SAR image analysis, the problems of change detection are de-speckling, change image generations from multi-temporal images, optimum thresholding, and inclusion of spatial information etc. Some methodologies were found in the literature for change detection using SAR images. Most of them start from generating the change image using multi-temporal intensity or amplitude images. They then used the supervised or unsupervised thresholding algorithm to segment the change and no-change areas but extremely few works have been done by including spatial information in the SAR change detection when moderate to low resolution images were used.

In the first part of this thesis, we propose supervised and unsupervised change detection methodologies focused on the analysis of multi-temporal SAR images. These approaches are based on three main steps: (1) a comparison of multi-temporal image was carried out by the normalized difference ratio (NDR) operator; which is using in this work for the first time in the SAR image and appear to be better than ratio and difference operators (2) implementing a novel supervised or unsupervised thresholding approaches and (3) generating the change map by coupling of thresholding along with a region growing algorithm. In the first step, two filtered multi-temporal images were used to generate NDR image that was subjected to analysis. In the second step, by assuming a Gaussian distribution in the no-change area, we identified the pixel range that fits the Gaussian distribution better than any other range iteratively to detect the no-change area that eventually separates the change areas. In the supervised method, several sample no-change pixels were selected and the mean (μ) and the standard deviation (σ) were obtained. Then, $\mu \pm 3\sigma$ was applied to select the best threshold values. Finally, threshold values obtained in previous step (step 2) was modified and implemented with the coupling of the region growing algorithm to consider the spatial information to generate the change map. The Gaussian distribution was assumed because it fits better in the no-change class than any other distribution while implementing the NDR image. The effectiveness of the proposed methods was verified with the simulated images and the real images associated with geographical locations. The results were compared with the manual trial and error procedure (MTEP) and traditional unsupervised expectation-maximization (EM) method. Both proposed methods gave similar results with MTEP and significant improvement in Kappa coefficient in comparison to the traditional EM

method in a simulated image and two SAR images associated with geographical locations. The coupling of the modified thresholding with a region growing algorithm is very effective with all methods.

With the advancement of the SAR technology, in addition to the single polarized SAR images, dual and (quad) fully-polarized SAR (PolSAR) images are available. The fully PolSAR images allow the generation of several very useful pieces of information and descriptors. These descriptors could supplement the results derived from single polarization images by adding several unique features, reflecting the complex nature of man-made structures, that could be sensitive to different types of changes in urban environments. The availability of the processing techniques and the possibility of generating several descriptors from fully PolSAR images have created a good opportunity to conduct a sensitivity study to find the most effective descriptors for detecting several types of the change. In this part of the study, we have the opportunity to identify the best pairs of complementary components of these polarimetric descriptors as well. Furthermore, a scope of an information fusion approach to combine information from the unique features found in complementary component in order to generate a better change map for urban and suburban environments is also created.

Thus, the objective of this study is twofold: first, to identify the most effective descriptors for each change type and ascertain the best complementary pairs from the selected polarimetric descriptors; and second, to develop an information fusion approach to use the unique features found in each polarimetric descriptor to obtain a better change map for urban and suburban environments. The effectiveness of each descriptor was assessed through statistical analysis of the sensitivity index in selected areas and through change detection results obtained by using the supervised thresholding method. A good agreement was found between the statistical analysis and the performance of each descriptor. Finally, a polarimetric information fusion method based on the coupling of modified thresholding with a region-growing algorithm was implemented for the identified complementary descriptor pairs. The mapping accuracy, as measured by the Kappa coefficient, was improved by 0.09 (from 0.76 to 0.85) with a significant reduction of false and missing alarm rates compared to single polarimetric SAR images.

In these two studies, I came to the conclusion that SAR images are very good for change detection, however they are not able to delineate the proper shape of the change area. Thus, in order to overcome such limitation, a SAR and optical information fusion approach is used. Several data fusion techniques are available which allow better analysis and interpretation by making use of complementary information obtained from multiple sensors. However, such works are mainly found to be motivated from the pan sharpening rather than the change detection or automatic change patter detection.

Several evidences are there which make use of multi-spectral image (MSI) information for change detection using CVA, and received a very good result. Similarly, it is being used for automatic multi-class change detection based on MSI, but the discriminated classes are very limited due to the lack of enough information. The major problem is that the indicators developed from MSI are linearly dependent and not the problem of the methodology i.e. CVA itself. As SAR and optical sensors have different signature of the same feature, they are assumed to be independent and can have complementary information. Thus, CVA could be a very good approach for SAR and optical information fusion. Additionally, it is known that the unique signature of SAR and optical images for each land use/cover feature is stable and site independent, in the similar weather and light condition for optical imagery and same acquisition configuration in case of SAR images, it is possible to develop a relationship between them and can deploy for an automatic change tracking.

In this study, a change magnitude image is generated through CVA based SAR and optical information fusion and segmented the change no-change area using thresholding. The fusion is motivated to use the complementary information without losing the inherent information that comes from either SAR or optical images for better change detection. Specifically, it improves the sharpness of the detected feature, or be able to detect the changed features that were otherwise not possible from a single data source.

Automatic change pattern mapping in urban and sub-urban area is important but challenging due to the diversity of urban land cover pattern. With the availability of multi-sensor (SAR or optical) imagery, it is possible to generate multidimensional unique information of Earth surface features from different sensors that allow

developing a relationship between a response of each feature to SAR and optical sensors to track the change automatically. Accordingly, an empirical relationship is developed by using the unique response from major features in the Earth's surface in SAR and optical imagery and deployed for automatic change pattern detection.

Thus, a SAR and optical data integration framework for change detection and a relationship for automatic change labeling were developed and deployed in this part of the study. It was carried out in three steps: (i) Computation of two indicators from SAR and optical images, namely: normalized difference ratio (NDR) from multi-temporal SAR images and the normalized difference vegetation index difference (NDVI difference) from multi-temporal optical images, (ii) computing the change magnitude image from NDR and NDVI difference and delineating the change area and (iii) the development of an empirical relationship, for automatic change labeling, in between NDR and the NDVI difference while changing a land use/cover feature from one type to another. The experiment was carried out in the outskirts part of Ho Chi Minh City, one of the fastest growing cities in the world. The improvement of the change detection results by making use of the unique information on both sensors, optical and SAR, is also noticeable with a visual inspection and the kappa index was increased by 0.13 (0.75 to 0.88) in comparison to only optical imageries. The empirical relationship between the response of surface feature to optical and SAR imagery has successfully delineated six changed classes in a very complex urban sprawl area that was otherwise impossible with multi-spectral optical imagery.

While summarizing all the works done in this dissertation, change detection from multi-temporal SAR images, PolSAR images and optical and SAR information fusion for automatic change pattern detection was done successfully. This research was based on the PolSAR image acquired by the Advanced Land Observing Satellite (ALOS) Phased Array type L-band Synthetic Aperture Radar (PALSAR) level 1.1 products and the optical images acquired by the Landsat 7, Enhanced Thematic Mapper Plus (ETM+).

TABLE OF CONTENT

LIST OF TABLES

LIST OF FIGURES

LIST OF ABBREVIATIONS

LC	Land Cover
SAR	Synthetic Aperture Radar
NDVI	Normalized Difference Vegetation Index
POLSAR	Polarimetric Synthetic Aperture Radar
EM	Expectation Maximization
MTEP	Manual Trial and Error Procedure
HIS	Intensity Hue Saturation
PCA	Principle Component Analysis
WT	Wavelet Transformation
MODIS	Moderate-Resolution Imaging Spectroradiometer
ENVI ASAR	Environmental Satellite Advanced Synthetic Aperture Radar
MSI	Multi-Spectral Image
ALSO	Advanced Land Observation Satellite
GCP	Ground Control Point
SLC	Single Look Complex
DEM	Digital Elevation Model
NCI	Neighborhood Correction Image
UTM	Universal Transverse Mercator
GDEM	Global Digital Elevation Model
NDR	Normalized Difference Ratio
AVNIR	Advanced Visible and Near Infrared Radiometer
QQ-PLOT	Quantile-Quantile Plot
ID	Image Differencing
LIDAR	Light Detection and Ranging
VR	Visible Red
NIR	Near Infrared
ETM+	Enhance Thematic Mapper Plus
SAVI	Soil-Adjusted Vegetation Index
EVI	Enhance Vegetation Index

ENVI	Exelis Visual Information Solutions
DN	Digital Number
CVM	Change Vector Magnitude
HR	High Resolution
VHR	Very High Resolution
UN HABITAT	United Nations Human Settlements Program
FAO	Food and Agriculture Organization
IPCC	Intergovernmental Panel on Climate Change

1 GENERAL INTRODUCTION

1.1 Introduction

Change detection is the process of identifying the state of a feature or phenomenon in the earth's surface from multi-temporal images acquired by same or different sensors [1]. Hundreds of thousands of people are moving to the urban area from rural area every year around the World. Thus, urbanization is in the highest increasing rate ever experienced in the word and it is likely to increase in the coming years [2]. Development associated with urbanization not only decrease the proportion of agricultural land, forest, open space and other land cover types but also affects the local as well as global environments. Consequently, information on land use/cover and their changing patterns is always a hot topic. The monitoring of land use/cover is extremely necessary due to its importance in several applications such as land policy development, site selection, demographic and environmental monitoring at national, regional or global scale as well as in promoting better decision-making.

Collecting the changed information from the ground-based survey would always better than any other options in terms of accuracy. However, it is impractical to do a ground based survey or the change mapping regularly in a short interval in rapidly growing urban areas. The remote sensing is the best available technique to update the changes [3]. Therefore, land cover and use change detection using a satellite based remote sensing is a very promising topic. The change detection in multi-temporal images has attracted increasing concern, especially in environmental monitoring, land-use/cover dynamics, disaster assessment, infrastructure planning and development etc.

1.2 Remote sensing for change detection: a historical perspective

Space borne sensor images have been extensively used to provide up-to-date land cover (LC) maps economically [4]. The use of high and very high resolution optical images for accurate change mapping is well accepted [4], but due to the inherent problems of the optical imageries – dependency on cloud and light condition, the optical images are not available all the time in all areas specially in humid tropical region and higher mountainous region. As an alternative, synthetic aperture radar (SAR) images would be an alternative in several parts of the earth.

Different types of change detection approaches are available in the literature. They can be categorized in several ways. If the change classes were segmented from unchanged classes without having prior information about the land cover status in the associated geographical locations (i.e. no ground truth available for modeling the data) is the unsupervised method [1], [5], [6]. Conversely, if some of the prior information about change and no-change area were provided and classify based on the provided sample, then the method is called supervised [1], [6]. In terms of the number of change classes and data nature, currently three types of change detection procedure are in practice namely, binary change detection [1], [5], [6], multi-class change detection [7], [8] and change detection in long time series of images [9], [10].

For the binary change detection, several supervised and unsupervised methods for multi-temporal optical, SAR or fusion of both images have been developed and published in several journal articles. Fig. 1.1 shows a schematic view of change detection. The process begins from the data collection, preprocessing steps and then goes for the data analysis that gives the change map. Even though the majority of the works in preprocessing and analysis part are similar, SAR and optical dataset have

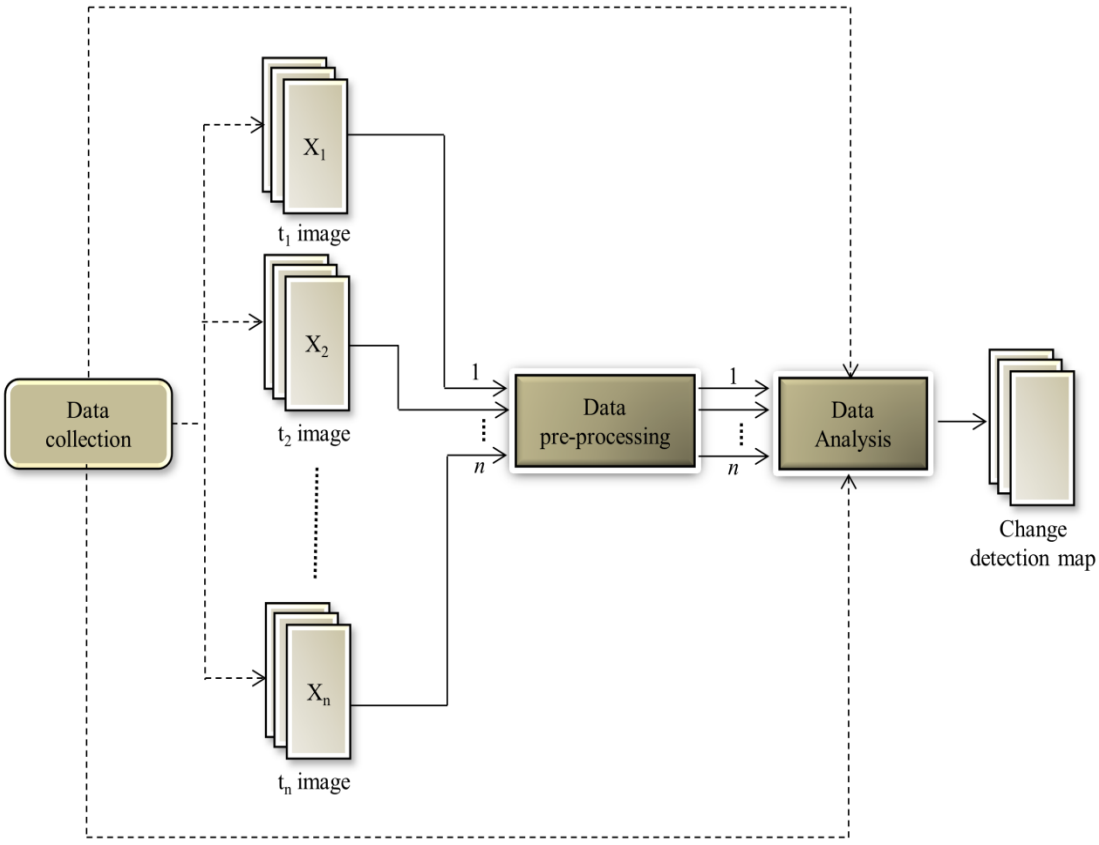

Figure 1.1 Schematic view of change detection.

some data specific radiometric corrections, image registration and image filtering. The actual change detection process includes in the analysis that may include developing a change image from multi-temporal images and then for pixel based thresholding or context based approaches.

1.3 Change detection in optical images

The most common way for change detection using optical images are: image differencing (ID) and followed by thresholding [1], [5], [6]. The NDVI is the major index while the change in vegetation is a major concern [9], [10]. However, while considering all kinds of changes the change vector analysis (CVA) with Tasseled cap transformation is one of the most common approaches [1], [5], [8] for multi-spectral images. The basic idea for change vector analysis is to subtract the vector generated from a multispectral image in one date to that with another date[7]. The changed and unchanged classes were then segmented through the threshold value of the vector magnitude image [5], [8]. The threshold values were identified either empirically or unsupervised theoretical thresholding strategy [6]. The CVA is recommended for change detection from a comparative study done by [11] among the most common four methods including: image differencing, image rationing, image regression, and CVA. In addition to that the CVA is able to detect the change direction automatically i.e. change pattern, as well [12].

1.4 Change detection in SAR images

Because of the several inherent shortcomings in optical imagery, for example weather and light condition, etc., SAR images are being used as an alternate data sources. They are less exploited in comparison to the optical images [6], this may be due to the complexity caused by speckle noise or may be the unavailability to common users. In spite of the less exploit, SAR images have already proven their usability for urban change detection because of their unique features and operational advantages over optical imageries. Several very good methods can be found for the automatic change detection through the SAR images [6], [13], [14], nevertheless several unresolved problems are still there.

In the context of SAR image analysis, problems of change detection are de-speckling, change image generations from multi-temporal images, optimum

thresholding, and inclusion of spatial information etc. Several methodologies are available in the literature for change detection using SAR images. Most of them start from generating the change image using multi-temporal intensity or amplitude images [6], [15], [16]. They then used the supervised or unsupervised thresholding algorithm to segment the change and no-change areas but very few or no-works have done by including spatial information in the SAR change detection when moderate to low resolution images were used.

With its all-time, all-weather capability, synthetic aperture radar (SAR) technology has been receiving considerable attention in the remote sensing community. Some studies of SAR imagery over urban areas have been carried out; however, most of them deal with mapping urban extension rather than urban land use and land cover patterns [16]. Due to the complex nature of manmade structures, polarimetric SAR (PolSAR) analysis becomes highly challenging. This is, perhaps, one reason why very few studies have been done for urban applications of SAR data in comparison to other aspects [16], [17].

In [18] Rignot and VanZyl, suggested to use ratio operator to compare multi-temporal SAR images. They mentioned that the ratio operator is more effective in minimizing the speckle noise. A few other similar papers [15], [16], [19], also recommended the ratio method as it is better to reduce the speckle presence in SAR image. Paper [20] implemented controlled adaptive iterative filtering and comparing the multi-temporal images using the log-ratio operator; finally an expectation-maximization (EM) thresholding algorithm was implemented. Paper [16] examines the effective methods for urban change detection using multi-temporal space borne SAR images. They used the modified ratio operator with an EM thresholding algorithm for automatic classification of the change image into two classes, viz., change and no-change. They concluded that the change detection accuracy obtained using the modified ratio operator and Kittler-Illingworth algorithm depends on how the assumed conditional class density function fits the histogram of change and no-change classes [16]. In another work, the difference of backscattering coefficients of the pre and post events and correlation coefficients between the pre and post events were implemented. A manual trial and error method was used to obtain the appropriate threshold value to detect the change in both indicators [21].

In pager [13] Dierking and Skrivel, suggested that the intensity images were better for change detection than phase difference and power correlation coefficient between the multi-temporal co-polarized images. They used the ratio operator to obtain the change image and decision mechanisms based on a desired value of probability of false alarm. The paper [6] presents an automatic change detection approach based on Generalized Gaussian model. They used the log-ratio operator to obtain the change image and the threshold value was obtained using the Kittler-Illingworth minimum-error thresholding by assuming the Generalized Gaussian model.

Some very good unsupervised methods to obtain two-way thresholding are also available; however, they work under the assumption of same distribution in the change and no-change areas of the image [16], [20]. Paper [20] proposed an algorithm under the Generalized Gaussian distribution in the change and no-change areas. Similarly, paper [16] evaluates the goodness of fit for several distributions. A threshold value was obtained using the EM thresholding and it manages to discriminate the increase and decrease intensity areas. However, the same distribution in both the change and no-change areas may not be valid in all cases. Thus, the most important lack here is the absence of any technique that can give two threshold values to segment all the possible cases of change in the SAR images, when there is not same distribution in change and no-change areas that that expect to happen often.

Regarding the supervised thresholding methods, the manual trial and error procedure (MTEP) is the only accepted method,[15], [22]. A log-ratio operator was implemented to generate a change image followed by an adaptive filtering, and manual selection of the decision threshold for change detection was presented in [22]. In another paper [21] MTEP was implemented to obtain the appropriate threshold for detection of the change area by using the difference of backscattering coefficients between the pre and post event images. Similarly, METP has been used as the base method to compare the outcome of the proposed two-way unsupervised thresholding method in [20].

1.5 Fusion of SAR and optical images for change detection

With the availability of multi-sensor images and their unique signature for each ground feature, potentially new research scope is created to enhance the change

detection and labeling automatically. Accordingly, to use the complementary information from multi-sensor images, several data fusion techniques have already been in practice. Data fusion of multi-sensor optical imagery has been exploited widely. Majority of such fusion techniques is motivated to pan sharpening [23]–[26]. The most common pan-sharpening methods include: an intensity-hue-saturation (IHS) transformation, [27], principal component analysis (PCA) [24], high pass filter [26] and wavelet transformation (WT) [23].

Even though, SAR and optical image fusion is not widely exploited in comparison to the multi-sensor optical images, some good approaches are already in practice. The motivation behind these fusion approaches is also to enhance the spatial resolution by preserving spectral information [25], [28]. In addition to that, SAR and optical fusion is driven from better land cover classification or some specific structure detection. Tupin and Roux [29] have used the SAR and optical data for building outline detection using feature based fusion approach in their study. Their study showed that SAR images are capable to show the building presence and optical images are good for the shape delineation – complementary information about building presence and proper shape extraction. They carried out it in two steps: first, extraction of partial potential building footprints on the SAR image and then shape delineation in the optical one.

In [28], Hong et al. proposed a fusion method based on wavelet-IHS transformation for SAR and optical MS images that was mainly motivated to preserve the spectral information of MS images and spatial detail of high resolution SAR image. In another work for grassland and alfalfa segmentation, the same fusion technique was implemented [29]. The fusion results gave spatial details of relatively high spatial resolution SAR imagery and spectral detail was obtained from low-resolution Moderate-resolution Imaging Spectroradiometer (MODIS) imagery. Major concern was again to improve the spatial detail.

In another research, [30] integrated optical and SAR imagery for developing annual crop inventories. They used two SAR (Envisat ASAR) and one optical (Landsat 5) imagery for crop classification and achieved above 80% of accuracy. The work was motivated to reduce the risk associated with operational implementation even though three optical imageries give acceptable results. Multi-temporal SAR

images alone are unable to achieve such high accuracy. Paper [25] integrates the pan sharpening and decision level fusion to develop a new change detection framework based on two-stage sequential fusion. And, others mainly work on the pixel level or decision level fusion.

As presented, several data fusion techniques are available which allow better analysis and interpretation by making use of complementary information. They mainly focused on pan sharpening rather than using the unique signature possible from different sensors. On the other hand the CVA approach was successfully used to making use of MS information for change detection. Therefore, it could be a very good approach for information fusion that can be obtained from optical and SAR imagery as well.

1.6 Multi class change detection

In addition to binary change detection, some works were inspired by automatic multi-class change detection [7], [8], [31]. They were mainly based on CVA on MS images. Here all the bands in MSI are highly correlated to each other, therefore, the discrimination of the number of land cover pattern is limited. As an alternative, the information acquired by SAR and optical images are not correlated and therefore have a good prospect to get the change pattern information in a considerable depth. It is known that the unique signature of SAR and optical images for each land use/cover feature is stable and site independent, in the similar weather and light condition for optical imagery and same acquisition configuration in case of SAR images. That allows to develop an empirical relationship between them in order to track the multi-class change pattern automatically.

1.7 Problem statement

An automatic thresholding is an important part of unsupervised land cover change detection and segmentation. As discussed in section 1.4, several algorithms are available and they seem to be very efficient in some applications. However, several shortcomings are there. Most of these algorithms are intended for bi-level thresholding. The histogram of the image is assumed to have one valley between two peaks. The peaks represent the background and objects respectively. And they

identified the threshold value using some statistical distributions. In this case there are mainly two unsolved issues:

- The majority of the automatic or semi-automatic change detection methods are under the assumption of specific distribution in change and no-change area, however, the assumption of the distribution in changed area is unpredictable, that is not valid in all cases and thus could be erroneous.
- Due to the dynamic nature of the earth's surface, some area has increased the backscattering intensity whereas in others it is decreased. Consequently, the histogram of the change image has at least two valleys and three peaks and often the middle peak is the highest as shown in Fig. 1.2. It needs a tri-level thresholding i.e. two threshold values one discriminate the increase in intensity and another decrease in intensity from unchanged background. Therefore, the conventional thresholding algorithms are not able to deal with this situation.

With the advancement of the SAR sensor, a fully polarimetric image is available. It allows the development of several descriptors through different image processing algorithms. The representation and fundamental methods are based on incoherent analysis, which works with an ensemble average of several pixels to give second order statics of polarimetric information. This allows the generation of several very useful pieces of information and descriptors. These descriptors could supplement

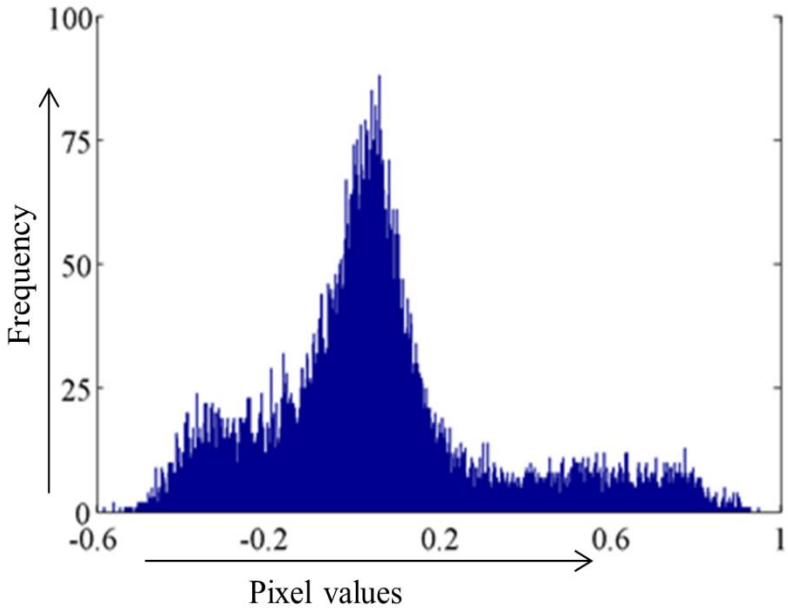

Figure 1.2 Histogram of the change image with change and no-change area.

the results derived from single polarization images by adding several unique features, reflecting the complex nature of man-made structures, that could be sensitive to different types of changes in urban environments. Therefore, it is important to identify the most effective components for each change type. In addition to that, an information fusion approach to combine such information about the unique features found in each polarimetric descriptor in order to generate a full-fledge change map for very complex urban and sub-urban environments.

A detailed study done for change detection for thematic mapping using PolSAR imagery suggests that intensity images are better for change detection than power correlation coefficient and phase difference between the co-polarized information [13]. And several other works [6], [16] and others were carried out based on intensity information, therefore we have considered only intensity information of the PolSAR images in this dissertation.

The fully polarimetric images may be a good source of information for the change detection, and several polarimetric descriptors may have complementary information. However, the SAR images often suffer from multiplicative nature of speckle noise. And, not detect some areas properly, mainly the boundary line of each change area is suffering from the clarity. In addition to that, some change occurred in the ground surface are not sensitive to the SAR backscattering due to the wavelength of a particular frequency of the SAR signal eventually SAR image cannot give a perfect result. Thus, information fusion between optical and SAR images can greatly enhance the change detection capability due to the complementary information available in these sources of images.

The usual method for the land cover change area along with change type detection is the post-classification overlay. However, due to various reasons the accuracy is very low and time consuming. It generates huge errors of change indications because the classification error in either date gives the false results of the change. The probability of accurate change detection is the product of probability of accurate classification in two dates. For example, the probability of correctly classification in either date is 0.8, while identifying the change area by overlying two classification results, the probability to get accurate change area is $0.8 \times 0.8 = 0.64$. Thus, accuracy will degrade greatly. This motivates to work in an automatic change

pattern detection to enhance the performance. A relationship between unique signature of SAR and optical images for each land use/cover feature can develop and deploy for an automatic change tracking, which is stable and site independent.

1.8 Research objective

SAR images have already attracted greater attention in the remote sensing community with its all-time, all weather capacity. In the context of SAR image analysis, the problems of change detection are de-speckling, change image generations from multi-temporal images, optimum thresholding, and inclusion of spatial information etc. With the advancement of the sensor technology, availability of the PolSAR images allow to generate several descriptors from fully PolSAR images have created a good opportunity to conduct a sensitivity study to find the most effective descriptors and complementary couple. In order to detect the full-fledged change area, information fusion of the polarimetric descriptors is required. Additionally, the SAR and optical sensors acquired unique signature for each land use/cover feature, that is stable, and site independent, therefore, this information could be extremely useful to enhance the change detection capability. However, this requires a new data processing technique to fully utilize the available information.

Aiming of the development of very good change detection algorithm with various SAR images acquired in different polarimetric modes and the fusion of SAR and optical information for automatic change pattern detection fulfilling the above-mentioned requirements, three methodological objectives must be achieved:

Objective 1: Change detection in urban environment from multi-temporal SAR images.

Due to the complex nature and the presence of speckle noise, the SAR images have not yet been exploited fully over urban areas. The goal is to develop a robust SAR methodology that can give a reliable estimation of change area in moderate resolution multi-temporal SAR images by including a spatial information.

Objective 2: Sensitivity analysis of the polarimetric descriptors and information fusion for change detection

Several polarimetric descriptors can be generated from fully PolSAR images that allows to conduct a sensitivity study to find the most effective descriptors for

detecting several types of change and the best pairs of complementary components of these polarimetric descriptors. In addition to that, an information fusion approach to combine the unique features found in each polarimetric descriptor is necessary for full-fledged change detection.

Objective 3: Optical and SAR information fusion to enhance the detectability and automatic change pattern detection.

Several existing SAR and optical information fusion approaches focused on the pan-sharpening rather than utilizing of the complementary information for change detection. Thus, it is very important to use the available complementary information for the better change detection. Additionally, due to the lack of independent and unique information, MSIs cannot delineate the change pattern to a sufficiently depth. This problem will be overcome by developing a relationship between SAR and optical information.

1.9 Reader's guide

The remainder of this thesis is organized as follows. Chapter 2 gives a brief introduction to the basics of the SAR system. Chapter 3 discusses the major problem identified and proposed solution to improve the change detection using single polarimetric SAR images. A sensitivity analysis on the polarimetric descriptors generated from PolSAR images and the fusion approach for the complementary pairs of such component is presented in Chapter 4. An information fusion approach for SAR and optical sensor and a framework to detect the change pattern automatically is provided in Chapter 5. The synopsis of this thesis and an outlook on further work are discussed in Chapter 6.

2 BACKGROUND

2.1 Introduction

Currently, multi-spectral, hyperspectral and microwave sensors are being used for the imaging purpose. Fig. 2.1 shows the electromagnetic spectrum, which indicates the wavelength range using for a different purpose in current imaging system. The MSI includes the visible to thermal range and microwave remote sensing use the higher wavelength range i.e. centimeter range.

Visible and infrared space-borne sensors measure the amount of radiation reflected (or emitted) back from the earth and its overlying atmosphere. Like our eyes, these sensors operate largely within the optical spectrum, producing images that are recognizable and ready for interpretation. Hyper-spectral images have dozens to hundreds of narrow contiguous bands.

RAdio Detection and Ranging is an active sensor system. The imaging radar along with the antenna mounting on a vehicle platform emits an electro-magnetic signal in a side looking direction towards the earth's surface. The backscattering signal from the surface received by the same or different antenna. The radar reflectivity of the received backscattering is the recorded intensity. The phase is also measured in the coherent radar system e.g. SAR. The phase information and brightness are used to generate the image. However, in the real radar system, only amplitude is measured [32].

This chapter introduces various aspects of satellite remote sensing images using SAR. A brief description on the basis of SAR technology is included in this section. The major contents involved – radar-imaging system, processing of SAR data, calibration, target decomposition etc.

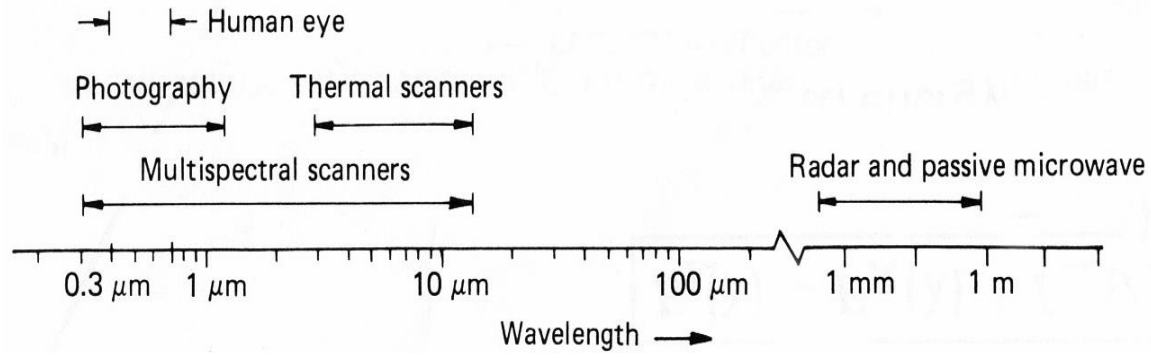

Figure 2.1 Electromagnetic spectrum using for different sensors.

2.2 Synthetic aperture radar (SAR)

The length of the radar antenna determines the resolution in the azimuth (along-track) direction of the image: the longer the antenna, the finer the resolution in this dimension. SAR refers to a technique used to synthesize a very long antenna by combining signals (echoes) received by the radar as it moves along its flight track. Aperture means the opening used to collect the reflected energy that is necessary to form an image that is the length of antenna in case of real radar system. A synthetic aperture is constructed by moving a real aperture or antenna through a series of positions along the flight track [32].

As the radar moves, a pulse is transmitted at each position; the return echoes pass through the receiver and are recorded in the memory. Because the radar is moving relative to the ground, the returned echoes are Doppler-shifted (negatively as the radar approaches a target; positively as it moves away). Comparing the Doppler-shifted frequencies to a reference frequency allows number of returned signals to be focused on a single point, effectively increasing the length of the antenna that is imaging that particular point. This focusing operation is known as SAR processing [32]. Frequency and wavelength, polarization, incidence angle etc. are the most important SAR specific parameters. They are discussed briefly in the following subsections.

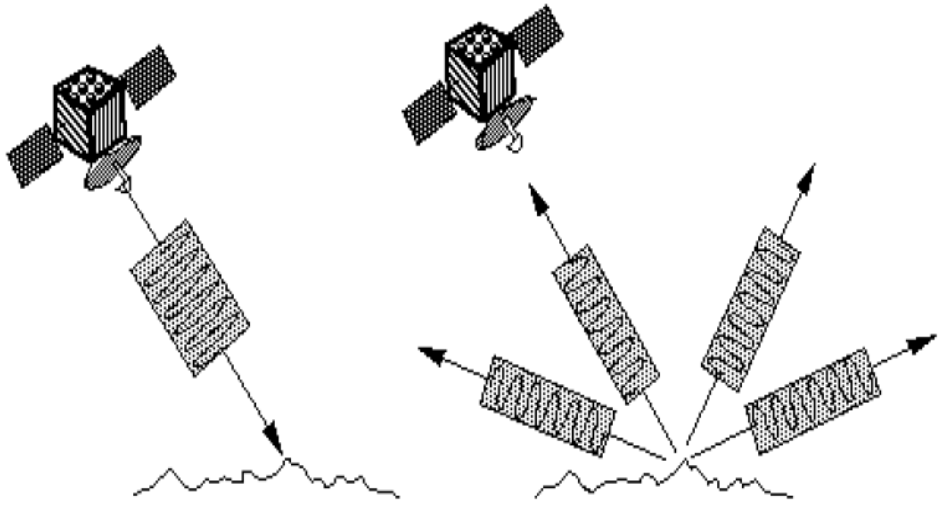

Figure 2.2 Radar transmits a pulse and measures reflected echo (backscatter). Source:[35]).

2.2.1 Wavelength and frequency

The distance between one crest to another crest is wavelength and the rate of oscillation of an electromagnetic wave is frequency. They are inversely proportional to each other (i.e. longer wavelength has lower frequency while shorter wavelength has higher frequency) [33]. The frequency range in radar are on the Gigahertz i.e 1 Gz to 1000Gz (a factor of one billion), the part of the electromagnetic spectrum with relatively larger wavelength i.e. in the centimeter. The electromagnetic wave with different frequency has a different influence on the medium [34]. In principle, radar signals are capable to penetrate the features. The larger the wavelength shorter the frequency and stronger the penetration in the vegetation and soil. Thus, the wavelength of the imaging radar is determined according to the applications, for example, X-band wavelength, the surface roughness of open areas can produces the image texture that distinct from the impervious surface. But at L-band wavelength, it may generate the similar texture in both. However, in the vegetation study, L-band data may prefer over X-band dataset. Table 2.1 illustrates the example of SAR sensors with different wavelength in general use.

2.2.2 SAR Polarimetry

A SAR system emitting strips of electromagnetic signal towards the earth's surface along the side of the flight direction. The sensor records the radar echo scattered back from the surface along the flying direction. The recorded information is the energy and the time delay of the echo. In SAR system, it is possible to selectively transmit and receive polarized energy such as horizontal transmission horizontal receives (HH), horizontal transmission vertical receives (HV), vertical transmission horizontal receives (VH), and vertical transmission vertical receives (VV). In case of

Table 2.1 Example of SAR sensors with different wavelength.

Band	Wavelength	Platform	Satellite/sensor
P-band	~65cm	air-/spaceborne	AIRSAR
L-band	~23 cm	air-/spaceborne	JERS-1 SAR, ALSO PALSAR/2
S-band	~10 cm	air-/spaceborne	Almaz-1
C-band	~5 cm	air-/spaceborne	ERS-1/2 SAR, RADARSAT-1/2, ENVISAT ASR
X-band	~3	air-/spaceborne	TerraSAR-X, Cosmos Skymed
K-band	~1.2 cm	air-/spaceborne	Military domain

Source: http://www.esa.int/ESA.

mono-static radar system, same antenna uses to transmit and receive the radar signal, however, in bi-static case, it is different.

They either transmit H or V polarization signal and receive the same polarization signal are called the co-polarization, however, if they transmit H polarization and received V polarization signal and vice versa are called cross-polarization. The cross-polarization is relatively weaker and associated with multiple volume scattering. There are mainly three types of polarization combinations, the Fig. 2.3 shows the HV polarization.

- Single polarizations – either HH, VV, HV or VH
- Dual polarization – either (HH and VV) or (HH and HV) or (HV and VV).
- Full or quad polarization - All four channels are present, i.e. HH, HV, VH and VV

The fully polarimetric mode can record the full vector nature of the electromagnetic radiation therefore it allows for detail and complete analysis of the backscattering echo. The polarimetric information of the backscattering echo is represented by the scattering matrix. In order to reduce the speckle noise the radar data are processed in the second order statistics of the scattering matrix i.e. covariance or coherency matrix which represents the complex information about targets.

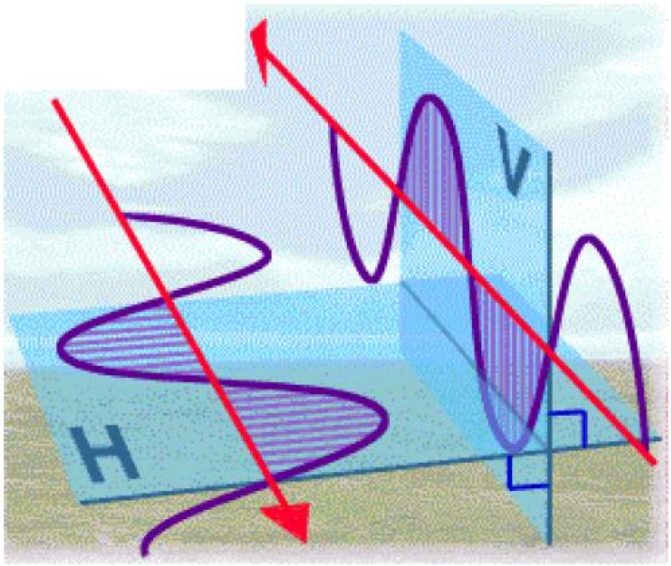

Figure 2.3 HV polarization signal.
Source: http://www.esa.int/ESA.

2.2.3 Incidence angle

The incidence angle (θ) is defined as the angle between the radar beam and a line normal to the earth's surface. The complementary angle of the incidence angle is called depression angle that is the angle between the radar beam and the horizontal line of the surface. Radar incidence angle can influence on the several aspects in the SAR images. Mainly, the backscattering may alter with the incidence angle. The surface scattering are normally strong at low incidence angles and decrease with increasing incidence angle [35]. Returns due to the volume scattering from a rough surface having low dielectric constant is likely to be uniform to all incidence angle. As radar backscattering depends on the incidence angle, an optimum configuration is possible based on the application and land surface pattern.

2.3 SAR data statistics

2.3.1 Single look complex, amplitude, intensity (power) data

SAR data are composed by a real and imaginary part (complex data), so called in-phase and quadrature channels, as shown in Fig. 2.4. The phase of a single-channel SAR system is uniformly distributed over the range of $-\pi$ to $+\pi$. In contrast, amplitude A has a Rayleigh distribution, and the Intensity I (or power P) = A^2 has a Gamma distribution. However, it approximates to the Gaussian distribution while increasing the number of looks.

2.4 SAR pre-processing

Prior to data analysis, initial processing on the raw data is necessary to carry out to correct for any distortion due to the characteristics of the imaging system and

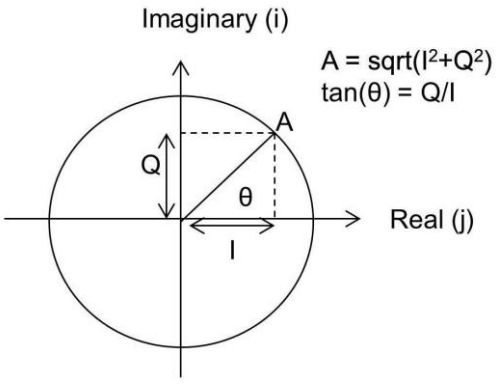

Figure 2.4 SAR data and statistic, composed by a real and imaginary part.

imaging conditions [36]. Depending on the user's requirement, some standard correction procedures may be necessary and thus carried out by the ground station operators before providing the data to the end-user. These procedures include radiometric correction for irregular sensor response over the whole image and geometric correction for geometric distortion due to earth's rotation and other imaging conditions (such as oblique viewing). The image may also be transformed to conform to a specific map projection system. Furthermore, if accurate geographical location of an area on the image needs to be known, ground control points (GCP's) are used to register the image to a precise map.

2.4.1 Multilinking

The single look complex (SLC) SAR image product is the highest possible resolution generated by using a full synthetic aperture and complete signal data history [37]. Multiple looks can be generated by taking the average over range and/or azimuth resolution cells. Multi looks expect to improve the radiometric resolution in the expense of spatial resolution. The goal is to obtain the multi-looked image approximately squared pixels considering the ground range resolution and pixel spacing in azimuth. The optimum number of looks can be obtained from the Eq. (2.1). The Fig. 2.5 (a) shows a single look image and Fig. 2.5 (b) is a multi-look image acquired by ALOS PALSAR.

$$ground\ range\ resolution = \frac{pixel\ spacing\ range}{\sin(incidence\ angle)} \qquad (2.1)$$

2.4.2 Co-registration

While working several images together, for example change detection, image rationing or similar operations are required to perform. SAR images must be co-registered before doing so. It is a process of superimposing, in the slant range geometry, two or more SAR images that are acquired over a same geographical location [38].

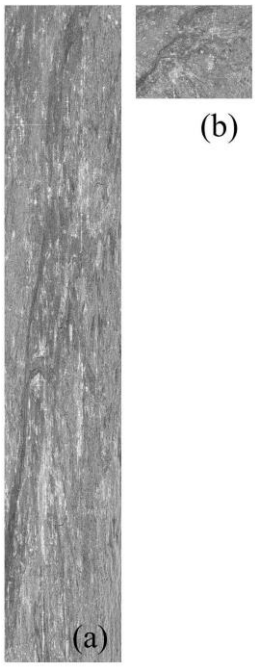

Figure 2.5 single look vs. multi-look image, (a) single look and (b) multi-look PALSAR images.

2.4.3 Geocoding

The process of converting each pixel from the slant range geometry to a cartographic reference associated with a specific coordinate system in the image. Two types of geocoding are possible.

Ellipsoidal Geocoding: The geocoding is done without referring the Digital Elevation Model (DEM) data

Terrain Geocoding: When carried out the geocoding with the use of DEM data.

Given sensor position vector $P = \{P_x,P_y,P_z\}$, velocity vector V_p, DEM position $G = \{G_x,G_y,G_z\}$, and velocity vector V_G. The following equations relate positions in the radar image to geodetic position in the Earth's surface:

$$(P_x\text{-}G_x)^2+(P_y\text{-}G_y)^2+(P_z\text{-}G_z)^2 = R_s^2 \quad (2.2)$$

$$\frac{2}{\lambda} \times \frac{P-G}{|P-G|}.(v_P - v_G) = f_{ref} \quad (2.3)$$

where the λ is the radar wavelength, while R_s and f_{ref} are the reference slant range and image Doppler respectively [39].

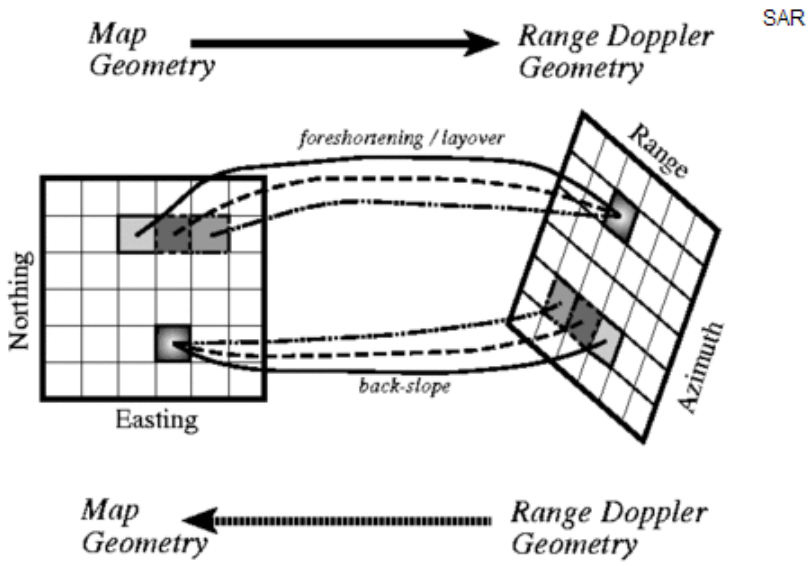

Figure 2.6 Georeferenced image; Source: [39].

2.5 Radiometric calibration

Radars measure the ratio of the power of the transmitted signal to that of received echo. This ratio is called the backscatter. This is system and acquisition mode dependent, thus in order to compare the received signal in various radar system, the radar backscatter need to convert to a standard format that is called the radiometric calibration. Following products can be obtained using the radio metric calibration of the SAR images.

Sigma Nought (σ○): The strength of reflected radar signal by a feature is also called the backscattering coefficient, it is expressed in dB. It is the dimensionless number that compares the strength observed from unit square meter. It has a significant variation with incident angle, wavelength, and polarization state and of course with the scattering property of the feature. It is computed by using Eq. (2.4).

$$\sigma^o = 10\log(DN^2) - CF \qquad (2.4)$$

Beta Nought (β○): is the radar brightness coefficient. It is the reflectivity per unit area in the slant range. It is computed by Eq. (2.5).

$$\beta^o = \frac{\sigma^o}{\sin(i)} \quad (2.5)$$

Gamma (γ): is the backscattering coefficient normalized by the cosine of the incidence angle. It is computed by Eq. (2.6).

$$\gamma = \frac{\sigma^o}{\cos(i)} \quad (2.6)$$

2.6 Scattering mechanism

SAR image is a representation of the received backscattering energy from the observed surface. The bright area indicates the stronger backscattering and the dark area represent the low backscattering. The Backscatter of the imaging feature in a specific wavelength vary with different conditions, such as the physical size, shape, alignment, electrical properties, water content of the targeted feature etc. The wet objects appearing brighter (except the water that act as a flat surface and reflect the radar energy away from the sensor), the wavelength, incidence angle, and polarizations of the SAR signal also effects the received energy. Fig. 2.7 illustrates the general backscattering characteristics of various features [32].

If the roughness of the ground object changes, the backscattering intensity is also changing, which leads to the SAR image changed. Based on the imaging features, three different types of scattering mechanism can be observed. Smooth surface like calm water surface, paved roads, runways, etc. causes the specular reflection. Most of the incident radar energy is reflected away according to the law of specular reflection and very little energy is scattered back to the sensor [36]. Rough

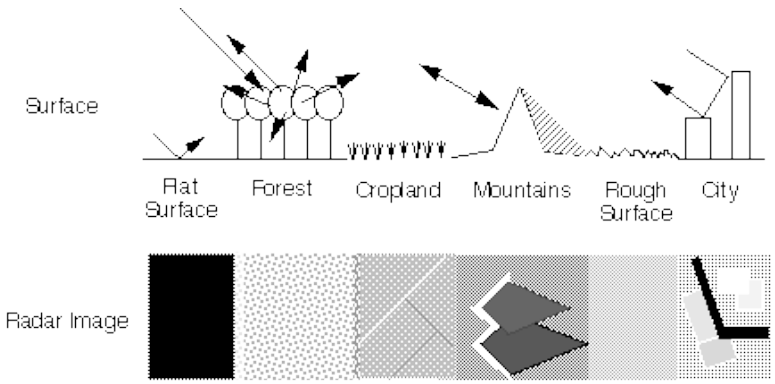

Figure 2.7 Imaging different types of surface with radar Source: [32].

surface such as forest, agricultural field etc. reflects the incidence radar energy in all directions. Part of the radar energy is scattered back to the sensor. However, the amount of energy received depends on the various characteristics of the observed objects such as orientation, size of the object. The dihedral structures, two smooth surfaces form a right angle facing the radar beam, generated a corner reflection thus, the most of the energy is reflected back to the sensor. In addition to the surface roughness, moisture content, wind direction, incidence angle etc. also effects the backscattering. Typical values of σ° for natural surfaces range from +5 dB (very bright) to -40 dB (very dark) [32].

If the land use/land cover pattern is changed from one type of surface to another type the quantity of backscattering energy will be changed. Thus, we assume that the changes – increase or decrease in backscattering energy will be standard while changing from one type of land cover to another type. The details of all the scattering mechanism are presented in the following subsections.

2.6.1 Surface scattering

A smooth surface acts like a mirror for the incident radar pulse. Most of the incident radar energy is reflected away according to the law of specular reflection, i.e. the angle of reflection is equal to the angle of incidence. Very little energy is scattered back to the sensor. The scattering mechanism is shown in Fig. 2.8 (a). The brightness of areas covered by bare soil may vary from very dark to bright depending on its roughness and moisture content and obviously with the frequency of the signal as well [36]. Typically, rough soil appears bright in the image. For similar soil roughness, the surface with higher moisture content will appear brighter.

2.6.2 Double bounce scattering

When two smooth surfaces form a right angle facing the radar beam, the beam bounces twice off the surfaces and most of the radar energy is reflected back to the sensor. The scattering mechanism is presented in Fig. 2.8 (b). Urban areas having such structures with proper alignment generates a stronger backscattering than non-aligned structures. In this case, radar pulse bounces off the horizontal ground towards the target, and then reflected from one vertical surface of the target back to the sensor

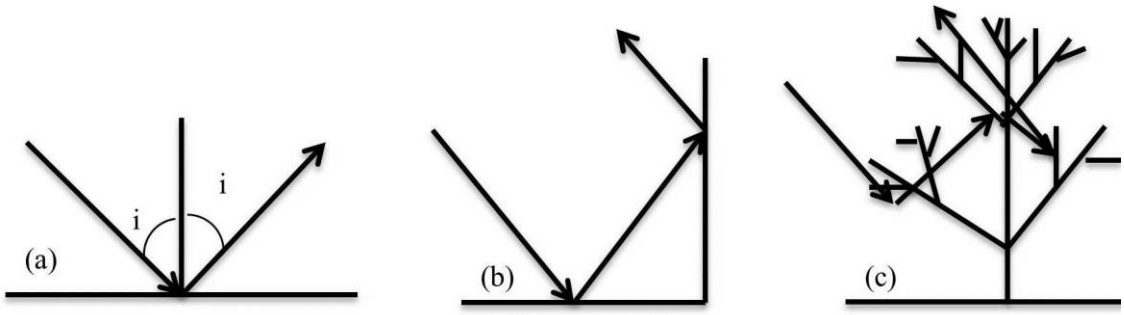

Figure 2.8 Scattering mechanism, (a) surface, (b) double bounce and (c) volume scattering.

due to the double bounce effect. Example of double bounce reflection are ships on the sea, high rise buildings and regular metallic objects such as cargo container [36] etc.

2.6.3 Volume scattering

A rough surface reflects the incident radar pulse in all directions. Part of the radar energy is scattered back to the sensor. The amount of energy backscattered depends on the properties of the target on the ground. Trees and other vegetation are usually moderately rough. Hence, they appear as moderately bright features in the image. The tropical rain forests have a characteristic backscatter coefficient of between -6 to -7dB, which is spatially homogeneous and remains stable in time [36].

2.7 Data representation

When the radar signal interacts with the target surface it changes its polarization state. That is, if the transmitted signal is horizontal polarization, the emitted signal would be both horizontal and vertical therefore, it gives the four combination of backscatter received in the fully polarimetric sensor, and is represented in the form of 2 ×2 scattering matrix as in Eq. (2.7).

$$S = \begin{pmatrix} S_{HH} & S_{HV} \\ S_{VH} & S_{VV} \end{pmatrix} = \begin{pmatrix} a & c \\ c & b \end{pmatrix} \tag{2.7}$$

where, all the elements of the scattering matrix denote the backscattering echo of the target of H or V polarizations and their both H and V returns polarization. The diagonal elements represents the co-polarization i.e., the transmitted signal and received signals have the same polarization however, non-diagonal elements represent

the cross polarization i.e. transmitted signal is in one polarization state and received the signal in different polarization state.

The scattering matrix describes the information of the pure target exhibiting a particular scattering mechanism. However, in general, the earth features are more complex and generating a variety of scattering response. In such a situation, the information obtained from the scattering matrix is insufficient to describe the physical properties of the surface. Therefore, second order statistics of the scattering matrix – covariance and coherency matrix are used for this purpose.

2.8 Target decomposition

One of the main advantages of polarimetric radar data analysis is the possibility of separating and identifying contributions from different types of scatters in the imaged terrain. To do this, the received scattering matrix can be analyzed using various techniques to extract information about the scattering processes. These methods are called target decomposition.

Target decomposition methods fall into two main categories, coherent and non-coherent. In the coherent case, a single scattered that produces a fully polarized scattered wave is assumed, and the scattering matrix is expressed as a combination of canonical scattering mechanisms and analyzed, for example Pauli decomposition [40]. incoherent target decomposition methods involve analysis of the power forms of the scattering matrix, such as coherency matrices [41]. Example of such method include ,Freeman and Durden three composition decomposition [42], Cloude and Pottier alpha-entropy decomposition [43], Yamaguchi four component decomposition [44] etc.

2.8.1 Pauli decomposition

The Pauli decomposition expresses the measured scattering matrix [S] in the Pauli basis. In case of mono-static system, Pauli decomposition decomposes [S] into three scattering mechanisms:

1. Single scattering by a smooth surface (single or odd bounce scattering).
2. Diplane scattering from corners wih relative orientation of 0°.

3. Diplane scattering from corners with a relative orientation of 45°.

The scattering matrix S can be expressed as the sum of these three matrices as follows [41]:

$$[S] = \begin{bmatrix} S_{HH} & S_{HV} \\ S_{VH} & S_{VV} \end{bmatrix} = \alpha[S]_a + \beta[S]_b + \gamma[S]_c \quad (2.8)$$

where, $\alpha = \frac{S_{HH}+S_{VV}}{\sqrt{2}}$, $\beta = \frac{S_{HH}-S_{VV}}{\sqrt{2}}$ and $\gamma = \sqrt{2}s_{HV}$

Thus, span of [S] can be obtained as:

$$SPAN = |S_{HH}|^2+|S_{VV}|^2+|S_{HV}|^2 = \alpha^2+\beta^2+\gamma^2 \quad (2.9)$$

2.8.2 Freeman and Durden three component decomposition

The Freeman and Durden decomposition method decompose the $<[T_3]$ matrix as a combination of second order descriptors corresponding to canonical objects[41]. The decomposition can be expressed as.

$$<[T_3]> = < P_s T_{surface} + P_d T_{double} + P_v T_{volume} >$$

where $[T_3]$ represents the canonical response and P_i is the coefficient of these component and their sum is equal to *SPAN*.

$$SPAN = Ps + P_d + P_v = T_{11} + T_{22} + T_{33}$$

Surface scattering is modeled by the first order Bragg surface scatter[42], [45] as:

$$T_{surface} = \frac{1}{1+\beta^2}\begin{bmatrix} 1 & \beta & 0 \\ \beta^* & |\beta|^2 & 0 \\ 0 & 0 & 0 \end{bmatrix}, \beta<1 \quad (2.10)$$

Double bounce scattering is modeled by a dihedral reflector as:

$$T_{double} = \frac{1}{1+\alpha^2}\begin{bmatrix} |a|^2 & \alpha & 0 \\ \alpha^* & 1 & 0 \\ 0 & 0 & 0 \end{bmatrix}, \alpha<1 \quad (2.11)$$

Volume scattering is given as.

$$T_{volume} = \frac{1}{4}\begin{bmatrix} 2 & 0 & 0 \\ 0 & 1 & 0 \\ 0 & 0 & 1 \end{bmatrix}, \quad (2.12)$$

For mono-static radar imaging, the three component decomposition is done under the assumption of $S_{HV} = S_{VH.}$ The procedure is applied as shown as the flowchart in Fig. 2.9.

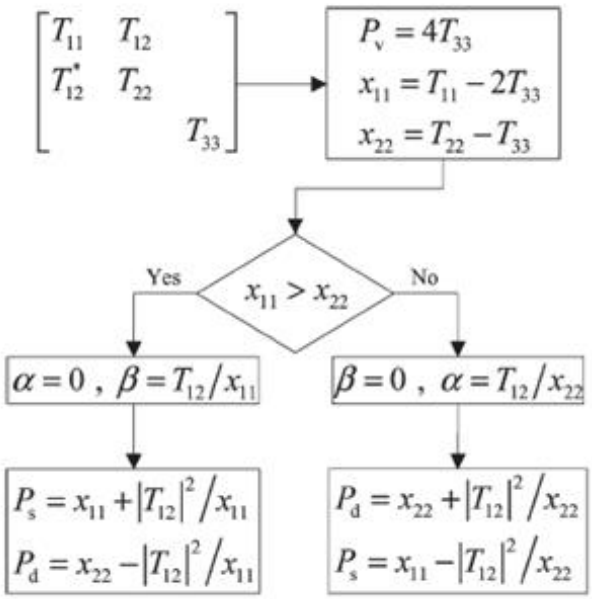

Figure 2.9 Flow chart, Freeman and Durden three component decomposition; Source: [41].

2.8.3 Eigenvector-eigenvalue based decomposition

It is the eigenvalue-eigenvector based analysis of a 3×3 coherency matrix. It provides information about scattering processes and their relative magnitudes. The coherency matrix T_3 can be decomposed as follows:

$$<[T_3]>=[U_3][\Sigma_3][U_3]^{-1} \quad (2.13)$$

where Σ_3 is a real diagonal matrix formed with eigenvalue of $<[T_3]>$.

$$[\Sigma_3] = \begin{bmatrix} \lambda_1 & 0 & 0 \\ 0 & \lambda_2 & 0 \\ 0 & 0 & \lambda_3 \end{bmatrix} \quad (2.14)$$

where $\infty > \lambda_1 > \lambda_2 > \lambda_3 > 0$.

The unitary matrix $[U_3]$ contains the eigenvectors u_i for i = 1,2,3 of $<[T_3]>$

$[U_3]=[\underline{u}_1,\underline{u}_2,\underline{u}_3]$

Thus, the eigen decomposition can be rewritten as.

$$<[T3]> = < [T_3] \geq \sum_{j=1}^{3} \lambda_i u_i u_i^{*T} \quad (2.15)$$

where ^{*T} is the complex conjugate.

In order to simplify the analysis of the physical information provided by this eigen value and eigen vector , three secondary parameters are defined as follows.

$$\text{Entropy (H)} = -\sum_{i=1}^{3} p_i log \quad (p_i) \; ; p_i = \frac{\lambda_i}{\sum_{k=1}^{3} \lambda_k} \quad (2.16)$$

where p_i is the probability of the eigenvalue λi, represents the relative importance of this eigenvalue with respect to the total scattered power.

The polarimetric scattering entropy defines the roughness of the scattering,

H =0 indicates a single scattering mechanism

And H =1 indicates a random mixture of scattering mechanism.

$$\text{And mean alpha angle } (\alpha) = \sum_{i=1}^{3} p_i \alpha_i \quad (2.17)$$

The scattering angle (α), the mean scattering mechanism, is a continuous angle ranging from 0 to 90 degree.

α -> 0: The scattering corresponds to single-bounce scattering

α->π/4: The scattering mechanism correspond to volume scattering.

A->π/2: The scattering mechanism is corresponding to double bounce scattering.

Polarimetric scattering anisotropy (*A*)

$$\text{Anisotropy } A = \frac{\lambda_2 - \lambda_3}{\lambda_2 + \lambda_1} \quad (2.18)$$

where $\lambda_1>\lambda_2>\lambda_3>0$.

The anisotropy *A* is a complementary parameter to entropy. It measures the relative importance of $\lambda_2>\lambda_3$. For low H values, $\lambda_2>\lambda_3$ are highly affected by noise, as *H* increases, the involved scattering process is difficult to distinguish. In such a case, anisotropy is useful to identify the distinguishable scattering processes.

3 COUPLING OF THRESHOLDING AND REGION GROWING ALGORITHM FOR CHANGE DETECTION IN SAR IMAGES

In order to fulfil the requirement of a robust change detection approach of the SAR images, we mainly focused on three basic problems in this chapter, including (i) a development of a change image from multi-temporal SAR images, (ii) thresholding value detection and (iii) inclusion of contextual information to reduce the false alarm in the boundary line.

3.1 Introduction

Southeast Asia is a home of nearly 600 million populations and lies three out of thirty mega cities in the world. The region has experienced rapid urbanization with above 3% of annual growth rate for the last couple of decades and is expected in the future as well. Development associated with urbanization not only decrease the proportion of agricultural land, forest, open space and other land cover types but also affects the local as well as global environments. Therefore, change detection in multi-temporal images have attracted increasing concern, especially in environmental monitoring, land-use/cover dynamics, disaster assessment, infrastructure planning and development etc. Space borne sensor images have been extensively used to provide up-to-date land cover (LC) maps [4] economically. The use of optical images has become widely acceptable for land use/cover change detection [4], but cloud cover is a common problem of visible and infrared remotely sensed images in humid tropical region. As an alternative, Synthetic Aperture Radar (SAR) images would be the best choice in the Southeast Asia.

SAR images have already attracted greater attention in the remote sensing community with its all-time, all weather capacity [46]. In the context of SAR image analysis, the problems of change detection are de-speckling, change image generations from multi-temporal images, optimum thresholding, and inclusion of spatial information etc. Several methodologies were found in the literature for change detection using SAR images. Most of them start from generating the change image using multi-temporal intensity or amplitude images [6], [15], [16]. They then used the supervised or unsupervised thresholding algorithm to segment the change and no-change areas but very few works have been done by including spatial information in the SAR change detection when moderate to low resolution images are used.

A ratio operator was used to compare two SAR images by Rignot et al., in [18] and suggested because this is more effective in minimizing the speckle noise than the difference image. A few other similar papers [16], [18], [19], also recommended the ratio method for SAR images because of its efficiency in reducing the speckle noise. Paper [6] implemented controlled adaptive iterative filtering and comparing the multi-temporal images using the log-ratio operator; finally an EM thresholding algorithm was implemented. Paper [16] examines the effective methods for urban

change detection using multi-temporal space borne SAR images. They used the modified ratio operator with an EM thresholding algorithm for automatic classification of the change image into two classes, viz., change and no-change. They concluded that the change detection accuracy obtained using the modified ratio operator and Kittler-Illingworth algorithm depends on how the assumed conditional class density function fits the histogram of change and no-change classes [16]. In another work, the difference of backscattering coefficients of the pre and post events and correlation coefficients between the pre and post events were implemented. A manual trial and error method was used to obtain the appropriate threshold value to detect the change in both indicators[21].

Most of the above thresholding algorithms are applicable for bi-level thresholding [6], [46]–[48]. The histogram of the image is assumed to have one valley between two peaks. The peaks represent the background and objects, respectively[49]. They identified the threshold value using certain statistical criteria such as variance, mean etc. As land cover/use nature is dynamic with time, some areas have increased backscattering intensity, whereas others have a decreased intensity. Therefore, the histogram of the change image has at least two valleys and three peaks and often the middle peak (around 1 in the case of the ratio operator) represents the no-change area. The remaining two peaks represent the change area for the increase and decrease in backscattering intensity. Thus, in land cover change, a tri-level thresholding is required i.e. two threshold values, one segments the increase in the intensity whereas the other segments the decrease in intensity, from the no-change pixels.

Some very good unsupervised methods to obtain two-way thresholding are also available; however, they work under the assumption of same distribution in the change and no-change areas of the image [16], [20]. Paper [20] proposed an algorithm under the Generalized Gaussian distribution in the change and no-change areas. Similarly, paper [16] evaluates the goodness of fit for several distributions. A threshold value was obtained using the EM thresholding and it manages to discriminate the increase and decrease intensity areas. However, the same distribution in both the change and no-change areas may not be valid in all cases. Thus, the most important lack here is the absence of any technique that can give two thresholds to segment all the possible cases of change in the SAR images, when there is not same distribution n change and no-change areas.

Regarding the supervised thresholding methods, the manual trial and error procedure (MTEP) is the only popular method, [4], [22]. A log-ratio operator was implemented to generate a change image followed by adaptive filtering, and manual selection of the decision threshold for change detection was presented in [22]. In another paper [21] MTEP was implemented to obtain the appropriate threshold for detection of the change area by using the difference of backscattering coefficients between the pre and post event images. Similarly, METP has been used as the base method to compare the outcome of the proposed two-way unsupervised thresholding method in [20].

Pixel wise change detection methodologies that are based on the threshold value(s), only uses the spectral information of the pixel [2-5 and many others]. It mostly ignores the spatial context and it is almost impossible to segment it with specific threshold value into the change and no-change areas perfectly. Therefore, it is very important to extend the methodology to include spatial information as well. However, thus far, spatial information is used in common practice, only in high resolution (HR) or very high resolution (VHR) images, although it is gaining popularity in image segmentation and change detection [31], [50], [51]. Several objects based change detection techniques which considered spatial information were discussed in [50]. Most of the segmentation approaches were grouped into either boundary or edge-based (discontinuity of pixels) or area-based (similarity of pixels) techniques. Another work [31] introduced a change detection model based on the neighborhood correlation image (NCI). However, in the middle to low resolution of SAR images, these methods are not in practice. Although it is very difficult to implement the object based contextual information in such resolution, it may be possible to introduce the spatial consideration, which can improve the change detection performance.

Thus, the major objective of this study is to investigate multitemporal single channel, single polarization SAR images for change detection using supervised and unsupervised change detection methods, without considering any predefined distribution in the change area. And, the spatial information will also be used to improve the change detection performance in the SAR images through the coupling of modified thresholding and region growing algorithms.

3.2 Methodology used

The framework of the change detection methodology in multi-temporal SAR images is presented in Fig. 3.1. The details regarding the methodology are presented in the following sections.

3.2.1 Preprocessing

All images were geocoded and co-registered to the Universal Transverse Mercator (UTM) system using the Global Digital Elevation Model (GDEM) with 30 m pixel spacing. Only the amplitude of the HH component of the multi-temporal fully Polarimetric Synthetic Aperture Radar (PolSAR) images acquired by ALOS PALSAR was used for the experiment.

The multiplicative nature of speckle noise presence in the SAR image may affect the performance of the methodology. Therefore, Enhanced Lee filter of window size 5×5 was implemented to reduce the speckle noise [52]. The window size was selected with a caution, if the size is bigger the spatial resolution will lose and if the window size is smaller, the filter will not be effective.

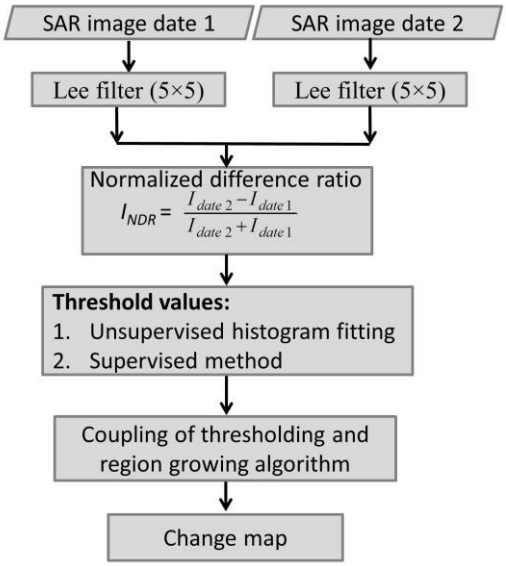

Figure 3.1 Work flow diagram.

3.2.2 Change image development

A normalized form of a ratio operator, Normalized Difference Ratio (NDR) operator, will be used to generate the change image. Unlike the ratio operator, the NDR operator generates pixel value from -1 to +1. All no-change pixels are clustered around 0, while all the change pixels are either close to -1 or +1. Therefore, it will give a clear peak for each type. More importantly, the NDR operator is effective to generate relative changes in the multi-temporal images. The change image generated by NDR operator can be seen in Fig. 3.2. The NDR operator is defined as:

$$Change_{i,j} = \frac{X2_{i,j} - X1_{i,j}}{X2_{i,j} + X1_{i,j}} \tag{3.1}$$

where $X1 = \{X1, i, j; i = 1\cdots m; j = 1\cdots n\}$ and $X2 = \{X2, i, j; i = 1\cdots m; j = 1\cdots n\}$ are co-registered images acquired on two dates, and i and j are the X and Y coordinates of pixels in the images.

To confirm the effectiveness of the NDR operator over widely used ratio operator, a following separability index is used [53].

$$Seperability\_index = \frac{|\mu_c - \mu_{uc}|}{\sigma_c + \sigma_{uc}} \tag{3.2}$$

where μ_c and σ_c are mean and standard deviation of change class and μ_{uc} and σ_{uc} are

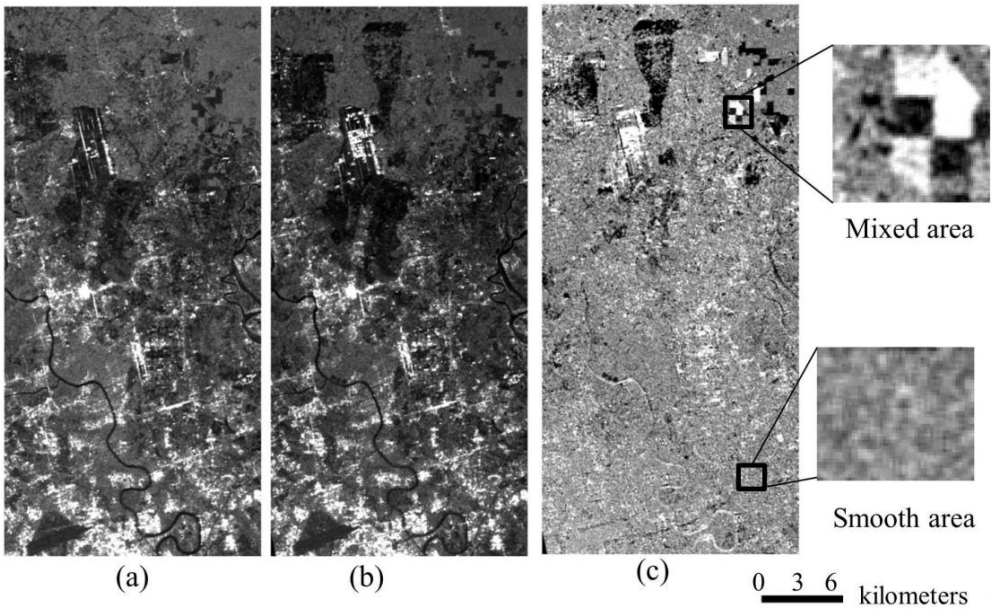

Figure 3.2 Change image generation through NDR operator. HH component of PolSAR images taken in 2007 and 2010, Change image (right big) generated using the NDR operator, along with the smooth area and mixed area.

mean and standard deviation of no-change class respectively. The higher value of separability index implies the better separability of change area from the no-change area.

3.2.3.1 Statistics

The data distribution in the resulted image was confirmed with the-QQ-plot on the dataset generated from the NDR operator with a pair of the simulated dataset having Gamma distribution with the same shape and scale parameter, where the shape parameter represents the number of looks and scale parameter is the inverse of the backscatter energy. In order to verify the effects of number of looks in multi-look images, several tests have been conducted in the various pairs of dataset with different shape parameter i.e. number of looks. Fig. 3.3 illustrates the results of the QQ-plot. It is observed in the figure that the fitting is better for higher number of look and the number of look above 5 has satisfactory fitting with a Gaussian distribution. Therefore, we assume that the Gaussian distribution in no-change area is valid in NDR image where number of look is above 5.

3.2.3.2 Comparison - NDR vs ratio operator

In order to confirm the performance of the NDR operator with widely used

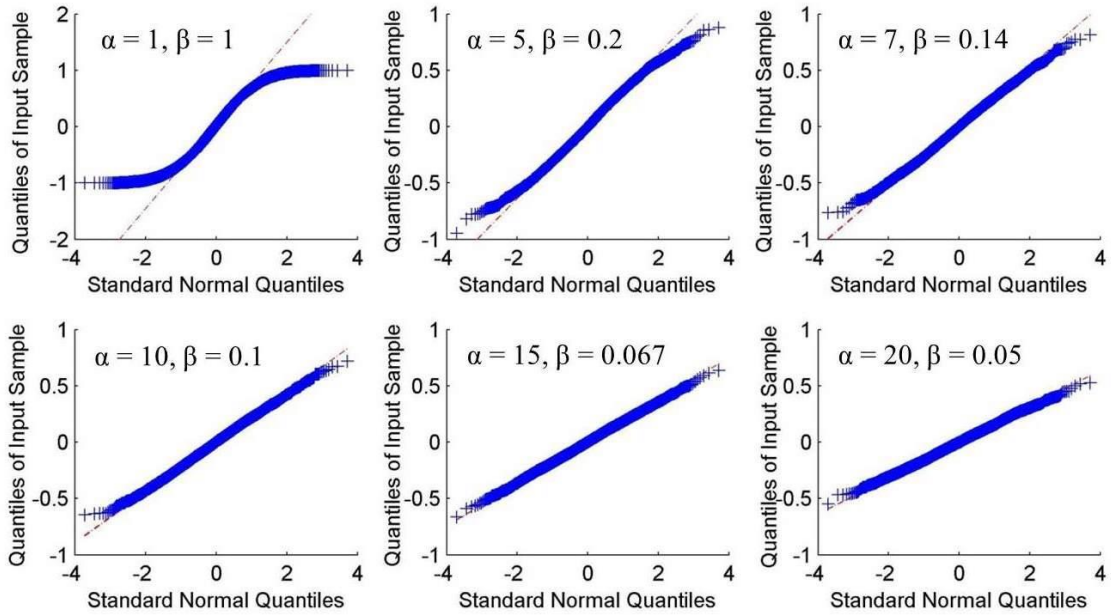

Figure 3.3 QQ plot of the NDR operator for the simulated dataset having Gamma distribution where α is the number of look and β is the scale parameter corresponding to the number of look.

ratio operator for the SAR image, we have developed a ROC curve (plotting of probability of false alarm vs probability of detection) Fig. 3.4. The results is considered to be better if the curve is closer to the upper left corner (0,1), and the threshold value which gives closest point from (0,1) in the curve is the best threshold value[21] (in other word - (having higher probability of detection and lower probability of false alarm). With the visual analysis, the curve generated from NDR image is closer to (0,1) but in one point the ratio image overcome. The most important point here is that, the threshold value that is closer to the (0, 1) lies in the NDR image. Therefore, from this comparison, what we can say is that, the NDR image can give the result at least as good as that gives by the ratio image.

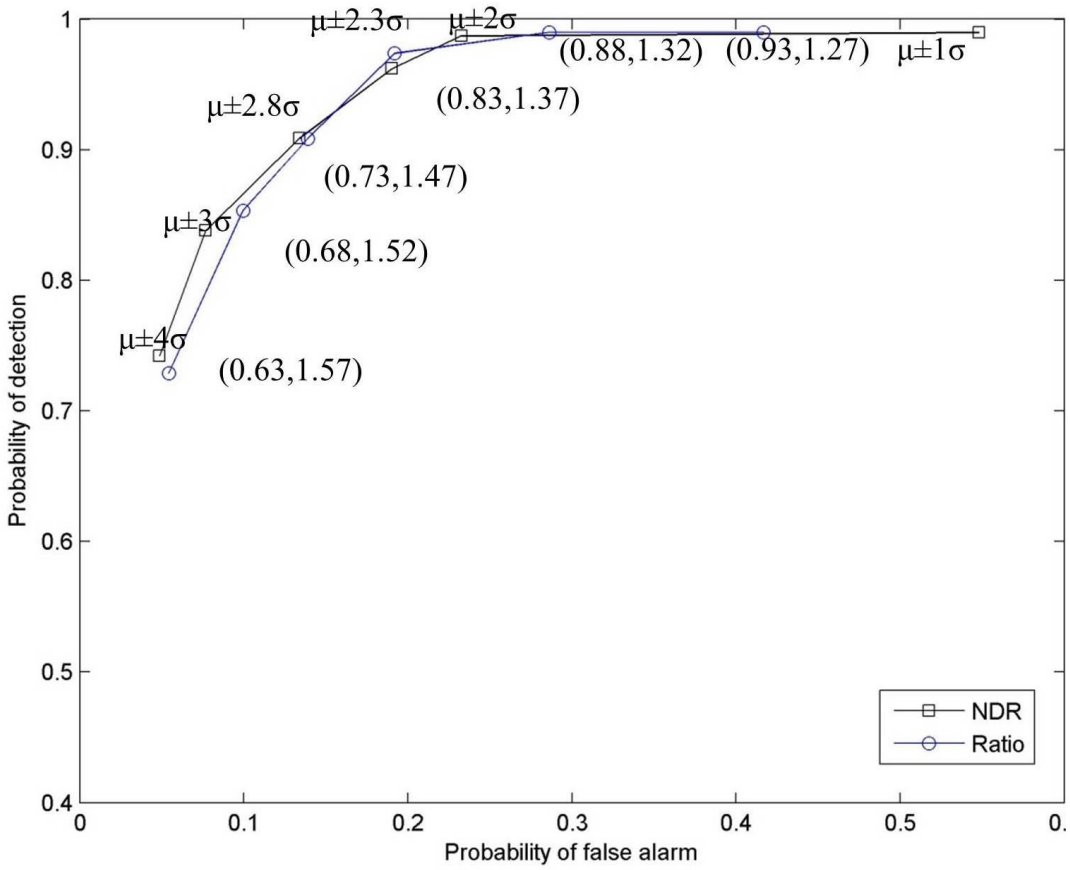

Figure 3.4 ROC curve for NDR and ratio images for the study area presented in Fig. 3.2, where μ and σ are mean and standard deviation of no-change area in NDR image respectively.

3.2.3. Change mapping

We aim to classify the area into $\{C_i, C_{nc}, C_d\}$ by threshold values of t_1 and t_2, where C_i, C_{nc} and C_d are associated with increase intensity, no-change and decrease intensity pixels respectively. Most of the thresholding algorithms are based on parametric approaches that assume a predefined statistical model in all change and no-change classes[6], [16], [20], [46], [47]. But, due to the dynamic behavior of the changing area and its complex nature, assuming a predefined statistical model for change class may not be valid in all cases.

Thus, assuming a Gaussian distribution in the no-change class, and both change –increase and decrease intensity areas do not follow any distribution, two thresholding methodologies - supervised and unsupervised are proposed in this study and explain as follows.

3.2.3.1. Thresholding

Unsupervised thresholding

Let the pixels in the change image be represented by the L gray levels [0, 1, 2,⋯ ,L]. Let x_j denote the number of pixels with the gray level j. A histogram $H(x)$ is formed of the image results in an ordered set of discrete values x_1, x_2, x_3,⋯,x_L. Our aim is to distinguish the H(x) into three classes as follows:

$$H(x) = \sum_{j=0}^{t_1} H(x_j) + \sum_{j=t_1+1}^{t_2} H(x_j) + \sum_{j=t_2+1}^{L} H(x_j) \qquad (3.3)$$

where t_1 and t_2 are the two thresholds that cover the no-change area. The first region from 0 to t_1 represents the change area - decrease in intensity, and the third term from t_1 to L is also the change area - increase in intensity. The no-change area follows the Gaussian distribution; thus we can approximate as below.

$$\sum_{j=t_1}^{t_2} H(x_j) \approx \frac{1}{\sigma\sqrt{2\pi}} \int_{t_1}^{t_2} e^{-\frac{(x-\mu)^2}{2\sigma}} \mathrm{dx} \qquad (3.4)$$

where, μ and σ are the mean and standard deviation of H(x) in an interval between t_1 and t_2.

Hence, the t_1 and t_2 can be found iteratively in such a way that the pixels within the range better approximate the normal distribution than any other interval in the histogram.

As shown in Fig. 3.3, the distributions of no-change class and change classes usually overlap. Thus, the optimum threshold is often located at the point where two distributions cross each other. If t_1 and t_2 are two cross point in left and right side of no-change class, the probability density fitting of no-change class will be the best in the range from t_1 to t_2. But, if t_1 moves left, the left tail will be heavier and if it moves right, the left tail will be shorter than the ideal one and vice versa while moving t_2. As a result, the probability density fitting will not be as perfect as before, thus this method is likely to select the cross point as the left and right bounds of the no-change area that eventually works as the threshold value.

Supervised thresholding

The basic premise in using remote sensing data for change detection is that changes in land cover must result in changes in reflectance values and changes in reflectance due to land cover change must be large with respect to reflectance changes caused by other factors [1]. However, in the case of the Synthetic Aperture Radar (SAR) images, it is the result of changes in backscatter and changes in the backscatter value due to the land cover change must be larger than the changes in backscatter caused by other factors.

As the no-change area has a Gaussian distribution, the range $\mu\pm3\sigma$ covers almost all pixels (99.7% of the total sample), and the rest are assumed to be noise. Therefore, it is clear that expanding the threshold value (e.g. $\mu\pm4\sigma$) will not increase inclusion of the no-change pixel considerably. With reference to the basic premise, none of the change pixels fall in the range of no-change area i.e. $\mu\pm3\sigma$. If we narrow down the threshold value, change pixels do not fall in that range, eventually increase the missing alarm of no-change area and false alarm of change area. For example, if narrow down the threshold value to $\mu\pm2\sigma$, 5% of the no-change pixels classify as the change area. Therefore, $\mu\pm3\sigma$ would be the ideal threshold value to segment the no-change area from change.

It is easy to recognize the no-change area in the image with the visual interpretation, which is relatively smooth. This is a good prospect to separate the no-change area in the image. The smooth area is defined as follows.

If the pixel(s) does not have any change, ideally the pre-event and post-event images should have the same backscattering intensity. However, due to phonological

changes or some noises, the backscattering intensity varies slightly; still they have a similar level of intensity. Therefore, the NDR generates a pixel value close to 0 for the no-change area and that looks smoother than other areas. The smooth area can be seen in Fig. 3.2.

Several sample no-change clusters in the change image generated through NDR operator can be selected interactively. As, the pixels in the no-change area are normally distributed, $\mu \pm 3 \times \sigma$ can cover 99.7% of the total population and that can work as a threshold value to separate no-change area from change. Thus, if sample no-change area gives the mean (μ) and standard deviation (σ) for no-change area, the threshold values can be computed as follows.

$$Threshold = \begin{cases} left\ Threshold\ (t_1) = \mu - 3 \times \sigma \\ right\ Threshold\ (t_2) = \mu + 3 \times \sigma \end{cases} \quad (3.5)$$

3.2.3.2. Coupling of thresholding and region growing algorithm

If the change pixels have significant differences in the backscattering intensity, those pixels are located in the extreme area, near -1 or +1, of the histogram. However, in the boundary line of the change region, the change in the backscattering intensity may not alter significantly; therefore, those pixels are located in and around the threshold values. Such pixels are always at risk to misclassify using only the thresholding criteria. This fact is evident in Fig. 3.5. Therefore, the classification scheme has been modified to use the spatial relationship of confirmed change and no-change pixels with those at risk. The methodology is modified by including the spatial information to detect the change area as follows.

If we have mean (μ) and standard deviation (σ) within the threshold values t_1 and t_2. The pixels less than t_1-σ are classified as a change - decrease intensity (C_1). Similarly, the pixels in the range t_1+σ to t_2-σ are classified as the no change area (C_2) and greater than t_2+σ are classified as a change – increase intensity (C_3). These classes have very few chances to misclassify. The remaining pixels in between t_1-σ to t_1+σ and t_2-σ to t_2+σ are left unclassified. The region growing algorithm [54] is then adopted to classify those unclassified pixels as.

At this stage, we have three classes (C_1, C_2, and C_3) and unclassified pixels. The classified pixels (C_1, C_2, and C_3) with modified thresholding values are treated as

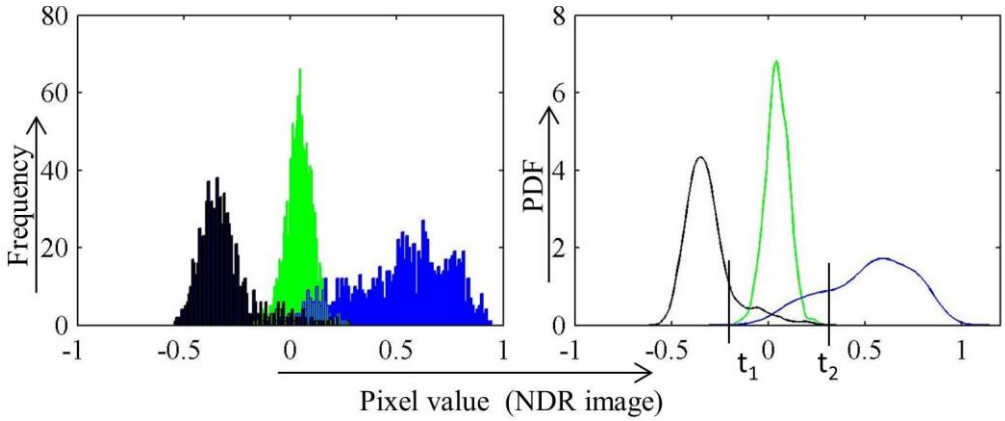

Figure 3.5 Histogram and non-parametric density fitting of decreased, increased and no-change intensity area. Left peak- decreased intensity, middle peak- no change and right peak- increased intensity area.

seed pixels. The set of unclassified pixels that have classified neighbors are defined as:

$$U = \left\{ x \notin \cup_{i=1}^{3} C_i \mid x \in \cup_{i=1}^{3} C_i' \right\} \tag{3.6}$$

where, i = 1,2,3 for potential three classes, C_i is set of pixels classified as i-th class, and C_i' is set obtained by two-time dilation of C_i.

$\forall x \in U$, compute the distance (Δx_i) with each connected class as follows:

$$\Delta x_i = \left| g(x) - g_i(c) \right| \tag{3.7}$$

where, i = 1,2,3, $g(x)$ is pixel value and $g_i(c)$ is average pixel values for each class, and calculated from connected pixels.

A pixel will be assigned to the class which has the minimum distance from the pixel. The process will be repeated as long as there is an unclassified pixel with at least two neighboring classes. The rest of the pixels were classified as no change [55].

3.2.4. Accuracy assessment

A confusion matrix has been used to estimate the change detection accuracy that allocates the change and no change class [56]. The accuracy with which change is detected and its expected value is derived from the confusion matrix, which provides a cross tabulation of the remote sensing derived labels with a corresponding ground reference dataset [57]. The entries in the confusion matrix along with the associated reference values may be used to derive the numerous summary measures of the accuracy of the classes and the amount of change that has occurred. Particularly, in

this study, the considered accuracy measures are correctly detected increasing and decreasing intensity (%), false alarm (%) that gives the number of missing pixels and falsely classified pixels in each class and Kappa coefficient gives the overall accuracy. To assess the accuracy, Advanced Visible and Near Infrared Radiometer type-2 (AVNIR-2) images acquired on nearly the same date as the SAR images as well as high-resolution QuickBird images from Google Earth were used. The reference change area was acquired by manual analysis.

3.3. Data used and study area

A pair of simulated SAR images and two pairs of real images – associated with geographical locations in Southeast Asia - Ho Chi Minh City and Bangkok were subjected to evaluate the robustness of the proposed methodologies. SAR images are sensitive to the seasonal vegetation, moisture content and other acquisition configuration. Therefore, fully polarimetric images acquired by the ALOS PALSAR images in the same acquisition configuration were used to detect changed areas. To reduce effects of phenological changes in vegetation and water content on the land surface, the images were acquired at nearly the same time of year. Additionally, both years selected in all cases had a normal precipitation pattern. Thus, all the changes detected in multi-temporal images are assumed to be related to human activity. The details of all data sets and study area are presented in the following sections.

3.3.1. Simulated dataset

To confirm the algorithm, a simulated SAR image is considered. As, the study focus in urban change detection, a pair of simulated images represents the change in dihedral structures, mainly construction and destruction of the structures for L-band. The size of the simulated image is (400 × 200) pixels. A simulator was developed with 7-look image that has Gamma distribution with various intensity levels for different objects. Simulated intensity values are set to be 2×10^6 on background, 8×10^6 on high intensity areas that is built-up area, and 5×10^6 on destructed area. Phase angle was uniformly generated in 0 to 2π. The bright and moderately bright area was changed in two simulated images to make sure of having a change area and the background intensity remains same in both images.

3.3.2. Ho Chi Minh City dataset

The first real dataset in this experiment is a section of (636 × 1357 pixels) two Advanced Land Observing Satellite (ALOS) Phased Array type L-band Synthetic Aperture Radar (PALSAR) images in Ho Chi Minh City acquired in April, 2007 and April, 2011. Ho Chi Minh City is one of the fastest growing Asian Cities. The total population was 7.52 million in 2011 whereas in mid-2007, the city's population was 6.65 million with nearly 3.1% of increasing rate [2]. Major changes in this section of the city are huge urban expansion in an agricultural land and deforested area. All data sets used in the study have the same acquisition parameters with the same viewing configuration. Therefore, we can assume that differences in the images' are directly related to the changes that occurred to the ground scatters.

3.3.3. Bangkok dataset

The second dataset represents a section of (548 × 876 pixels) two SAR images acquired by the ALOS PALSAR over Bangkok, Thailand, in May, 2009 and May, 2010. Bangkok is a mega city having 14.6 million populations with annual growth of 0.9% [2]. The image contains the majority of the highly populated urban area, thus there are not big change clusters. Similar to the Ho Chi Minh City, all data sets used in the study have the same acquisition parameters with the same viewing configuration. Therefore, we can assume that differences in the images' are directly related to the changes that occurred to the ground scatters.

3.4. Experimental results and discussions

Three different experiments were performed to evaluate the results obtained from the proposed supervised and unsupervised algorithms. First, the effectiveness of the algorithm was validated in a simulated SAR image then implemented into two real images associated with geographical locations. In the geographical locations, one is the fastest growing South East Asian City – Ho Chi Minh City and another is a Southeast Asian mega city – Bangkok. To reduce the speckle noise, a Lee filter [52] of window size 5×5 was implemented. Then, the change image was generated and the methodologies proposed were implemented. Goodness of fit test was performed to confirm the distribution of the change image in all cases. Three statistical models, namely normal, logistic and student's-t distribution were selected to perform the

goodness of fit test. A widely used visual interpretation technique named QQ-plot was selected to confirm the goodness of fit [58]. The coupling of thresholding and region growing algorithm was done to consider the spatial information while classifying. The results were evaluated with the referenced change map developed interactively with several high and very high optical images. The accuracy measures considered are correctly detected change (%) in increase and decrease intensity area separately, false alarm (%), and Kappa coefficient. Finally, the results obtained were compared with the results obtained from the widely used EM based thresholding algorithm [16], [20], [46] and a manual trial and error procedure (MTEP) [4], [20].

3.4.1. Experiment with simulated image

3.4.1.1. Statistical analysis

To confirm the statistical distribution, samples were taken for change, no-change and mixed (change and no-change) areas from the change image generated by the NDR operator in simulated image. Fig. 3.6 (a) – (c) shows the QQ-plot of the mixed, both change and the no-change areas against the standard normal, logistic and student's-t distribution sample dataset. The no-change area has good alignment with

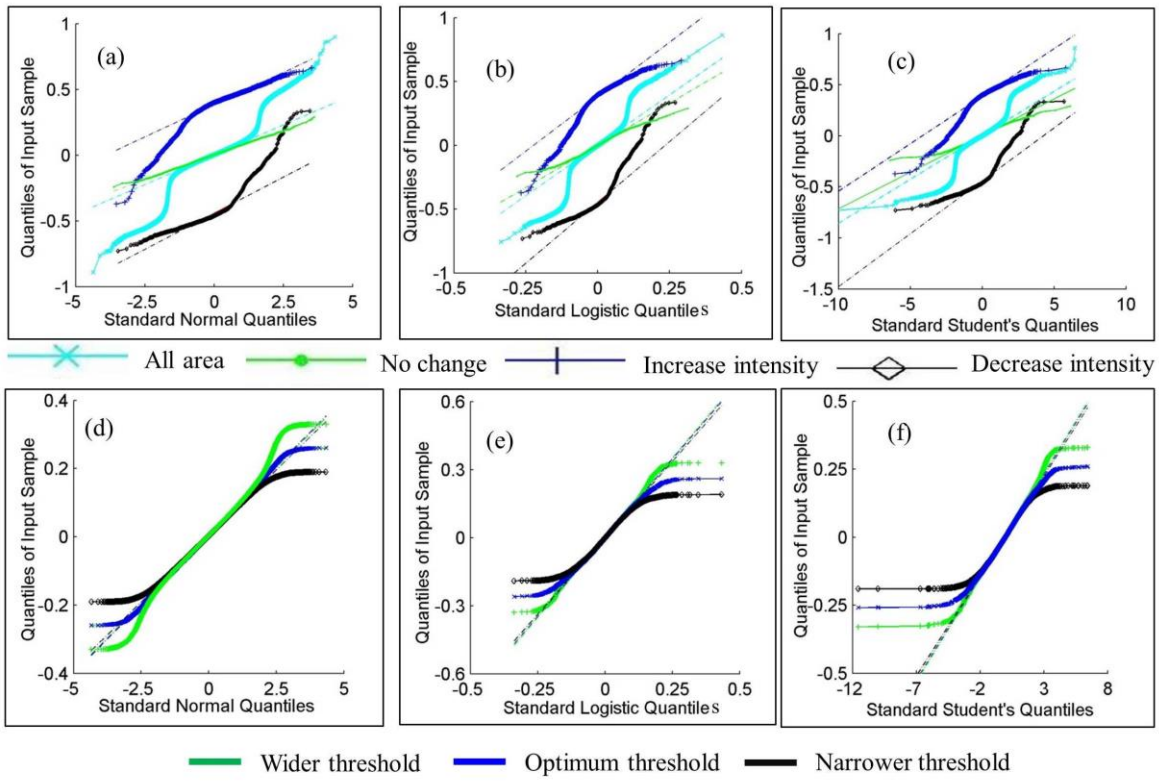

Figure 3.6 QQ plot for several input samples with various statistical distributions in simulated image.

all distribution however all other areas – both changes and all areas do not reveal any matching. If we further evaluate the matching of no-change area, normal distribution is close to impeccable in comparison to other two distributions.

To further confirm he distribution Fig. 3.6 (d) – (f) represents the QQ-plot of optimum threshold value, narrower and wider than optimum against standard normal, logistic and student's t distribution respectively. The optimum threshold values were obtained with the MTEP, which gives the best results, show the best matching against normal distribution.

3.4.1.2. Change mapping

The changed results obtained from simulated dataset are presented in Fig. 3.7. The threshold values obtained by supervised and MTEP were same and thus both of them depict the same results. The unsupervised approach has some missing alarm however this is recovered while implementing the coupling of thresholding and the

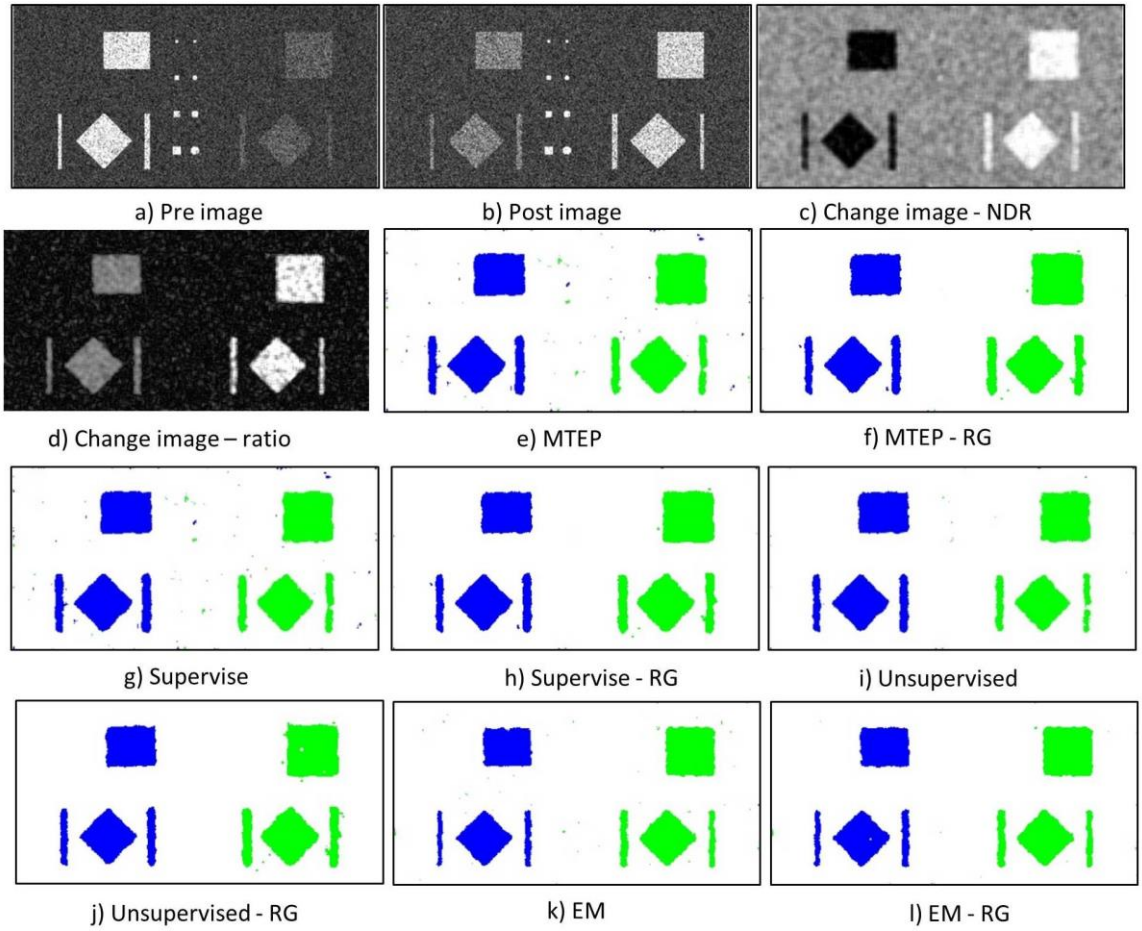

Figure 3.7 Results obtained in simulated image, (a), (b) simulated SAR images, (c) NDR – image, (d) ratio – image, (e) – (l) Change map obtained from several methodologies in simulated image (RG- region growing).

region growing algorithm. The effect is clearly visible in the increased intensity rectangle which is smoother in the edge in comparison to that obtained only with threshold values. Some missing alarm is visible in the boundary region of all shapes in the results obtained from the EM method that is also improved greatly while implementing the coupling of thresholding and region growing algorithm.

Table 3.1 represents the accuracy obtained from the simulated image with different methodologies. Increase intensity and decrease intensity show the percentage of correctly classified pixels in an increase and decrease intensity area respectively. False alarm denotes the percentage of falsely classified pixels and Kappa coefficient shows the overall accuracy. As the threshold value obtained from MTEP and the supervised algorithm are same, the results from these two methods are same. The overall performance is very high in these methods, however some overestimation causes a slight decrease in overall performance and increase false alarm. On the other hand, the proposed unsupervised method is slightly better at detecting the change pixels than EM, however, they have very similar overall accuracy. That is because of the overestimation caused by unsupervised method. Despite having a very good change detection capacity in all method, the coupling of thresholding with region rowing algorithm seem to be equally effective in reducing the false alarm and improving the detection capacity.

3.4.2 Site 1 – Ho Chi Minh City

3.4.2.1 Statistical Analysis

The first experiment associated to geographical location was performed in Ho Chi Minh City. The separability index was computed to demonstrate the effectiveness

Table 3.1 Accuracy assessment in simulated data.

Indicators	**MTEP**	**MTEP - RG**	**Sup.**	**Sup. - RG**	**Unsup.**	**Unsup.- RG**	**EM**	**EM-RG**
Increase intensity (%)	91.72	95.45	91.72	95.45	90.23	93.86	88.03	93.16
Decrease intensity (%)	94.69	95.52	94.69	95.52	93.15	94.79	85.17	91.72
False alarm (%)	12.88	9.12	12.88	9.12	14.80	11.64	14.91	12.23
Kappa coefficient	0.92	0.94	0.92	0.94	0.91	0.93	0.91	0.93

Unsup.- unsupervised, Sup. – supervised, EM – Expectation Maximization, RG – region growing.

of the NDR operator in comparison to the ratio operator. Fig. 3.8 represents the separability index for major change features, namely bare land or agricultural land to dihedral structures, deforestation, and destruction of building etc. with no-change class while using NDR operator and ratio operator. The aim is to discriminate the change area from no-change area; therefore all the separability indexes were measured with respect to no-change area. In all change types, the NDR image has a higher separability index than that for ratio image; therefore NDR operator would be better for the change detection.

Similar to the simulated image the statistical distribution is confirmed to the samples taken for change, no-change and mixed (change and no-change) areas from the change image generated by the NDR operator in Ho Chi Minh City. Fig. 3.9 shows the QQ-plot of the mixed, change and no-change areas against the standard normal, logistic and student's-t distribution sample dataset and with different threshold values. The optimum threshold value was obtained with the MTEP, which gives the best results and presented in the same section.

Fig.3.9 (a) is the QQ-plot of the quantiles of the all area of change image, no-change area, and both change areas against the standard normal quantile. The curve for the all change area image shows a heavy tail; and, the curve for the no-change area has good alignment with the reference line. However, for the change area, both the increase and decrease intensity do not reveal any match. Similar results can be seen in Fig. 3.9 (b) which is against the standard logistic quantile. Here, too, the curve for

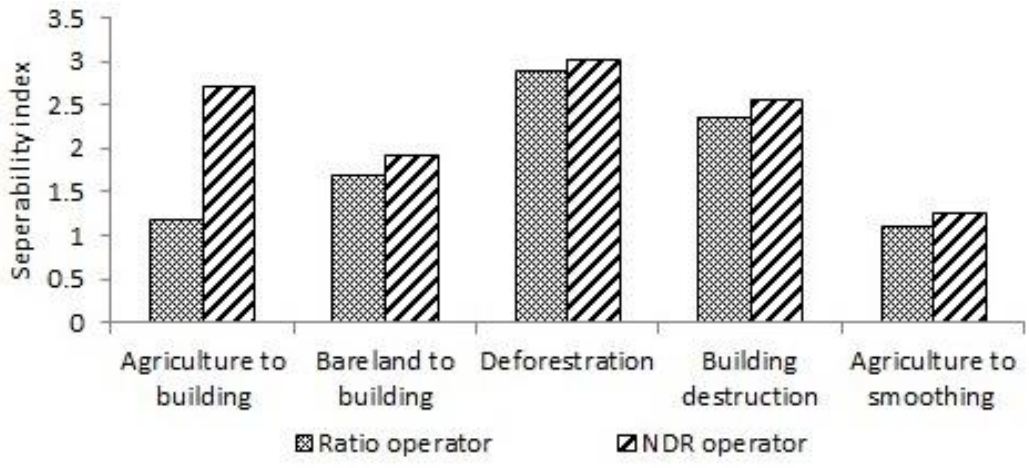

Figure 3.8 Separability index for major change classes by ratio and normalized difference ratio operator in Ho Chi Minh City.

whole image reveals the long tail and the no-change area shows the reasonable alignment with the reference logistic distribution, and no match is seen with both change areas. Fig. 3.9 (c) is for student's-t distribution with 8 degrees of freedom, which gives the best result compared with any other number of freedoms. In this case also, only the no-change area has considerable alignment with the standard reference line although the matching is not as good as the normal distribution and logistics distribution. If we compare the matching in the three distributions tested in the no-change area, the standard normal quantile shows the best matching.

Based on the plotting in Fig. 3.9 (a) - (c), we conclude that the no-change area can better model with normal distribution. Still, to further improve the confidence, in Fig. 3.9 (d) - (f) we tested the distribution with different threshold values in the image against all considered distributions. In Fig. 3.9 (e) two datasets, one with the optimum threshold value and another with the narrow range have a very short tail compared with the standard logistic distribution, and the dataset showed a wider range than the optimum having a better alignment with the standard reference line and very similar

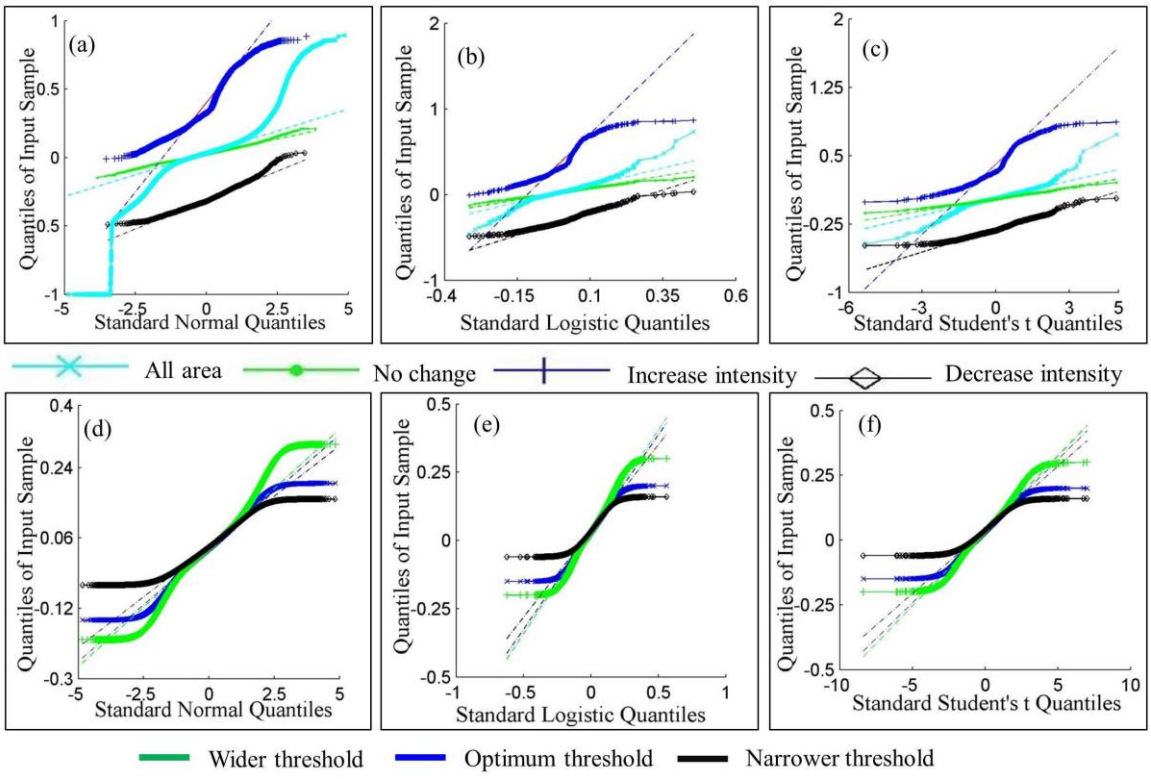

Figure 3.9 . QQ plot for several input samples with various statistical distributions in Ho Chi Minh City.

results can be seen in Fig. 3.9 (f) as well. On the other hand, Fig. 3.9 (d), it is clear that the wider the threshold range longer the tails, while the shorter the threshold range shorter the tails than the standard normal distribution. However, if the threshold is optimum, the data can approximate with the normal distribution. It is this threshold value that gives the best change detection results.

3.4.2.2. Change mapping

The results obtained by implementing the EM, MTEP, proposed supervised, and unsupervised algorithms are presented in Fig. 3.10, with increasing and decreasing intensity shown in green and blue, respectively. The majority of the increasing intensity is changed from the open area or agricultural area to the built-up area and the decreasing intensity area is changed from the forest to the open space (deforestation) or the agricultural area to the open space (bare land). The main misclassification occurred in the boundary area, and the highest misclassification occurred between the no-change to the decrease intensity or vice versa. Similar kinds of misclassification are also observed in the middle part of the change area where small patches of no-change area is surrounded by the change area. These misclassifications are reduced significantly while implementing the coupling of thresholding with the region growing algorithm. Thus in the change detection problem, a threshold value alone is unlikely to give a perfect result because of the spatial relation of the pixels in the boundary region. This is confirmed by the effectiveness of the methods proposed with the inclusion of spatial information in the generation of an accurate change detection map.

Only thresholding algorithms and the coupling of modified thresholding with the region growing algorithms were implemented independently. The change

Table 3.2 Accuracy assessment in Ho Chi Minh City.

Indicators	**MTEP**	**MTEP -RG**	**Sup.**	**Sup. - RG**	**Unsup.**	**Unsup.- RG**	**EM**	**EM-RG**
Increase intensity (%)	82.52	84.76	86.78	86.51	80.83	80.87	82.01	82.31
Decrease intensity (%)	82.39	92.69	66.70	86.81	53.13	62.75	39.08	49.09
False alarm (%)	11.00	10.25	12.32	11.13	11.87	10.30	13.12	11.43
Kappa coefficient	0.76	0.78	0.74	0.76	0.72	0.75	0.70	0.73

Unsup.- unsupervised, Sup. – supervised, EM – Expectation Maximization, RG – region growing.

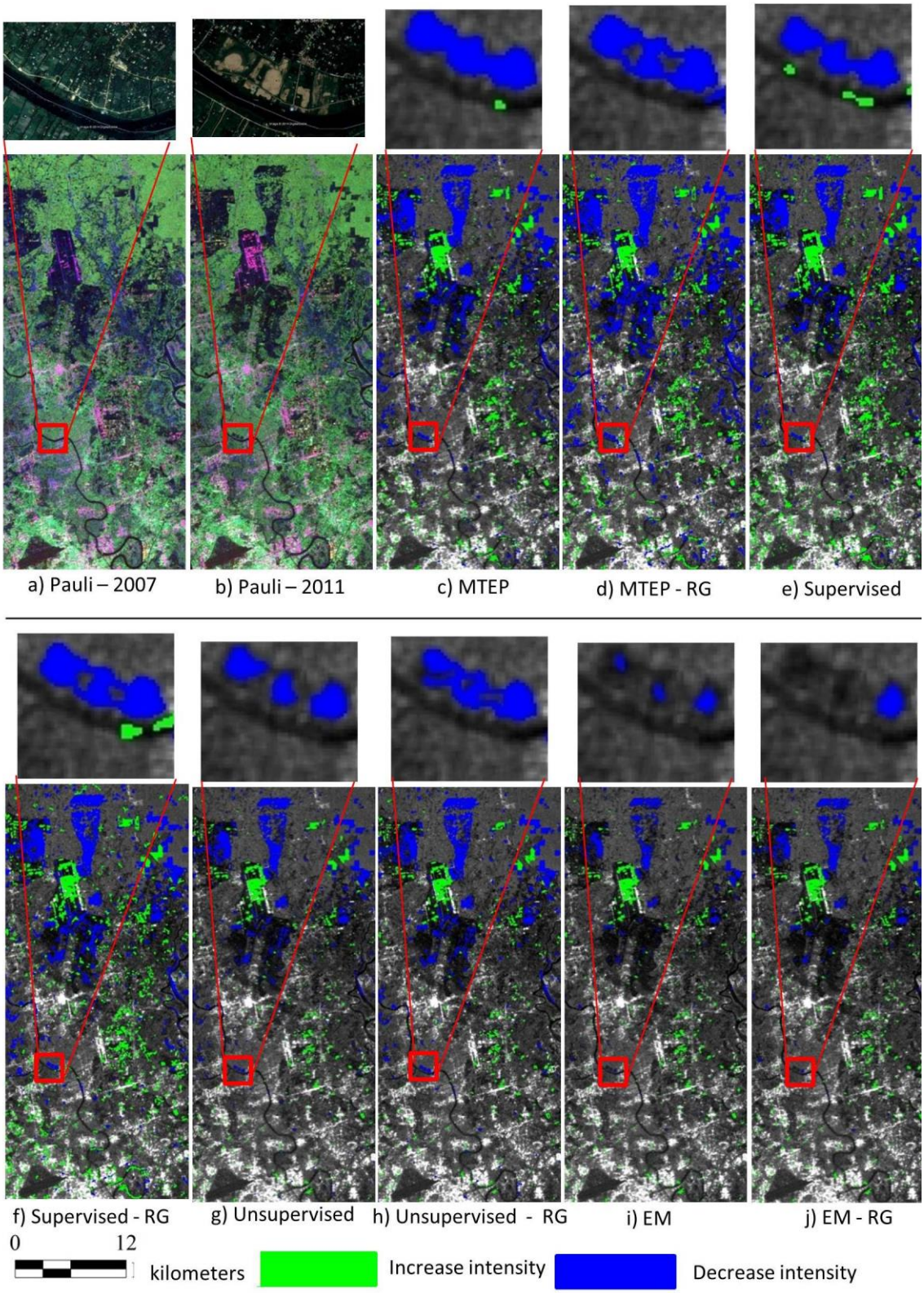

Figure 3.10 Change map in Ho Chi Minh City. (a), (b) Pauli composition of PolSAR image, (c) – (j) Change map obtained from several methodologies, and a corresponding zoom in area.

detection results with the coupling of modified thresholding and the region growing algorithm show significant improvement over the results obtained only with

thresholding values in all considered algorithms. Additionally, the results obtained from both methodologies proposed outperform the results from the traditional EM thresholding.

Table 3.2 shows the accuracy assessment of the change results obtained in the Ho Chi Minh City. Similar to the previous section, the increase intensity and decrease intensity show the percentage of correctly classified pixels in an increase and decrease intensity area respectively. Likewise, false alarm reflects the percentage of falsely classified pixels and Kappa coefficient shows the overall accuracy. In all indices, MTEP gave the best possible result. The supervised methodology also generated similar result with the 0.75 of Kappa coefficient and 11.13% of false alarm. The coupling of thresholding with region growing algorithm is appeared to be highly effective in all cases.

The change pixels surrounded by no-change pixels, and vice versa in several places, were observed in the results (see Fig. 3.9 (d), (f), (h), (j)) while considering the spatial information. This is because, several patches within the forests were already open in the pre-image; the intensity changes in these pixels are relatively higher than others in the no-change area. This may be due to the filtering effects in the pixels surrounded by the highly varying pixel intensity or noise introduced from the surrounding area to the enclosed small area. If changes in the center really occur, the backscattering intensity should vary in the center pixels to at least as high as in the surrounding pixels that justify them to be classified as change area. The detection of a small patch of no-change area that is surrounded by the change area is impressive.

3.4.3. Site 2 – Bangkok

3.4.3.1. Statistical analysis

Another experiment with geographical location was performed in Bangkok. In this experiment, we considered a relatively short time interval so it has a little change area than in site-1. Fig. 3.11 represents the separability index for major change features namely bare land or agricultural area to dihedral structures, deforestation, building destruction, and an inundation area with no-change class while using the NDR operator and the ratio operator. Similar to Ho Chi Minh City, the NDR image has a higher separability index than that in the ratio image in all change classes.

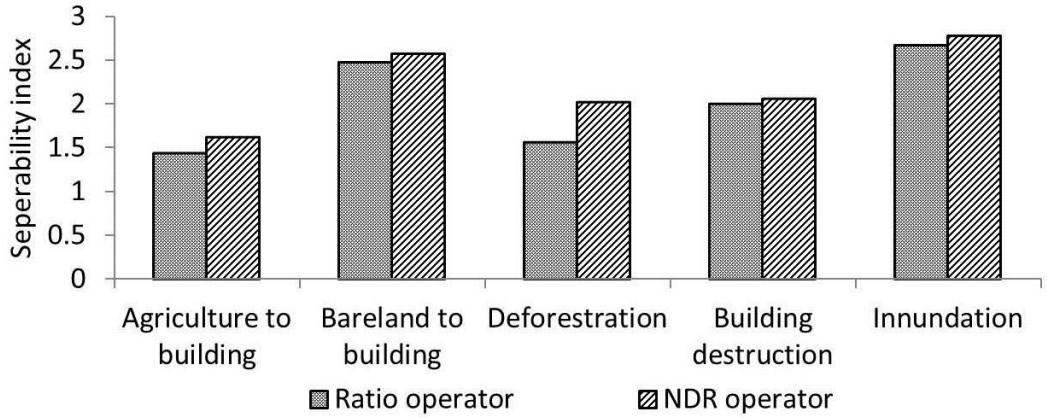

Figure 3.11 Separability index in several change area with respect to no change area in Bangkok.

Similar to the Ho Chi Minh City the statistical distribution was confirmed with the samples taken for change, no-change and mixed (change and no-change) areas from the change image generated by the NDR in Bangkok. Fig. 3.12 shows the QQ-plot of the mixed, change and no-change areas against the standard normal, logistic and student's-t distribution sample dataset and with different threshold values. The optimum threshold value was obtained with the MTEP, which gives the best results and presented in the same section.

Fig.3.12 (a) – (c) represent the QQ-plot of the quantiles of the all area of change image, no-change area, and both change areas against the standard normal quantile, standard logistic quantile and student's t-distribution quantile with 8 degrees of freedom. The nature of the curves in all distributions and in all input samples is very similar to that in simulated image and Ho Chi Minh City. The curve for all area shows a heavy tail; however, the curve for the no-change area has good alignment with the reference line. Furthermore, for the change area, both the increase and

Table 3.3 Accuracy assessment in Bangkok.

Indicators	**MTEP**	**MTEP -RG**	**Sup.**	**Sup. - RG**	**Unsup.**	**Unsup.- RG**	**EM**	**EM-RG**
Increase intensity (%)	78.19	78.85	78.19	78.85	64.98	73.35	52.86	61.23
Decrease intensity (%)	87.25	98.95	87.25	98.95	67.65	94.73	67.23	85.88
False alarm(%)	4.16	4.28	4.16	4.28	6.47	4.69	6.87	5.19
Kappa coefficient	0.84	0.85	0.84	0.85	0.74	0.84	0.72	0.81

Unsup- unsupervised, Sup. – supervised, EM – Expectation Maximization, RG – region growing.

decrease intensity do not reveal any match in all distributions. If we compare the matching in the three distributions tested in the no-change area, the standard normal quantile shows the best matching.

The change image in Bangkok area is plotted against all selected statistical distributions with optimum, narrower and wider threshold values to further improve the confidence. The plotting is represented in Fig. 3.12 (d) - (f). The nature of the plots in all threshold values in all distribution is similar to that in Fig. 3.9 (d) – (f). Thus, this test also confirms the Gaussian distribution in no-change area and eventually, the optimum threshold range as well.

3.4.3.2. Change mapping

Fig. 3.13 represents the change results obtained by implementing the EM, MTEP, proposed supervised and unsupervised algorithms in Bangkok. Similar to simulation dataset, the MTEP and supervised algorithms generate the same results on this site. The major changes occur are from open space or agriculture to built-up, and inundation area. Similar to the previous experiment the coupling of the modified

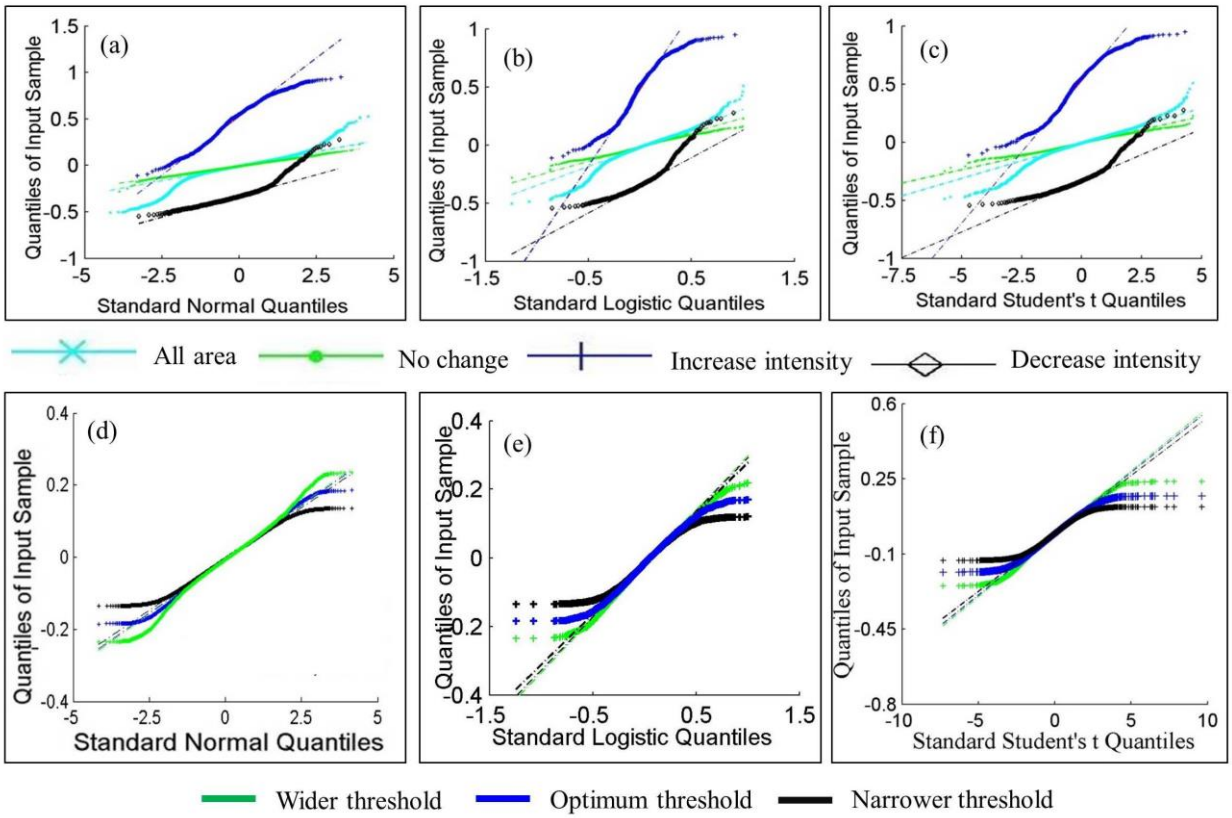

Figure 3.12 QQ plot for several input samples with various statistical distributions in Bangkok.

thresholding with a region growing algorithm that incorporate the spatial information enhances the performance greatly. However, it is more effective in the case where thresholding value generates higher false classification. Concerning the change detection accuracy, the performance given by the both proposed methodologies is superior than that in EM and supervised method has similar to MTEP which is regarded as the best method.

The change accuracies obtained in Bangkok are presented in Table 3.3. Similar to the simulated results, the MTEP and supervised methodology have the same results followed by the proposed unsupervised methodology. The improvement in the Kappa coefficient, overall detection capability and false alarm is clear in both proposed methodologies in comparison to EM method. The improvement in correctly classifying pixels while implementing the coupling of thresholding with region growing algorithm is significant. The proposed coupling of thresholding with region growing algorithm appear to be more efficient in the area where higher false classification occurred.

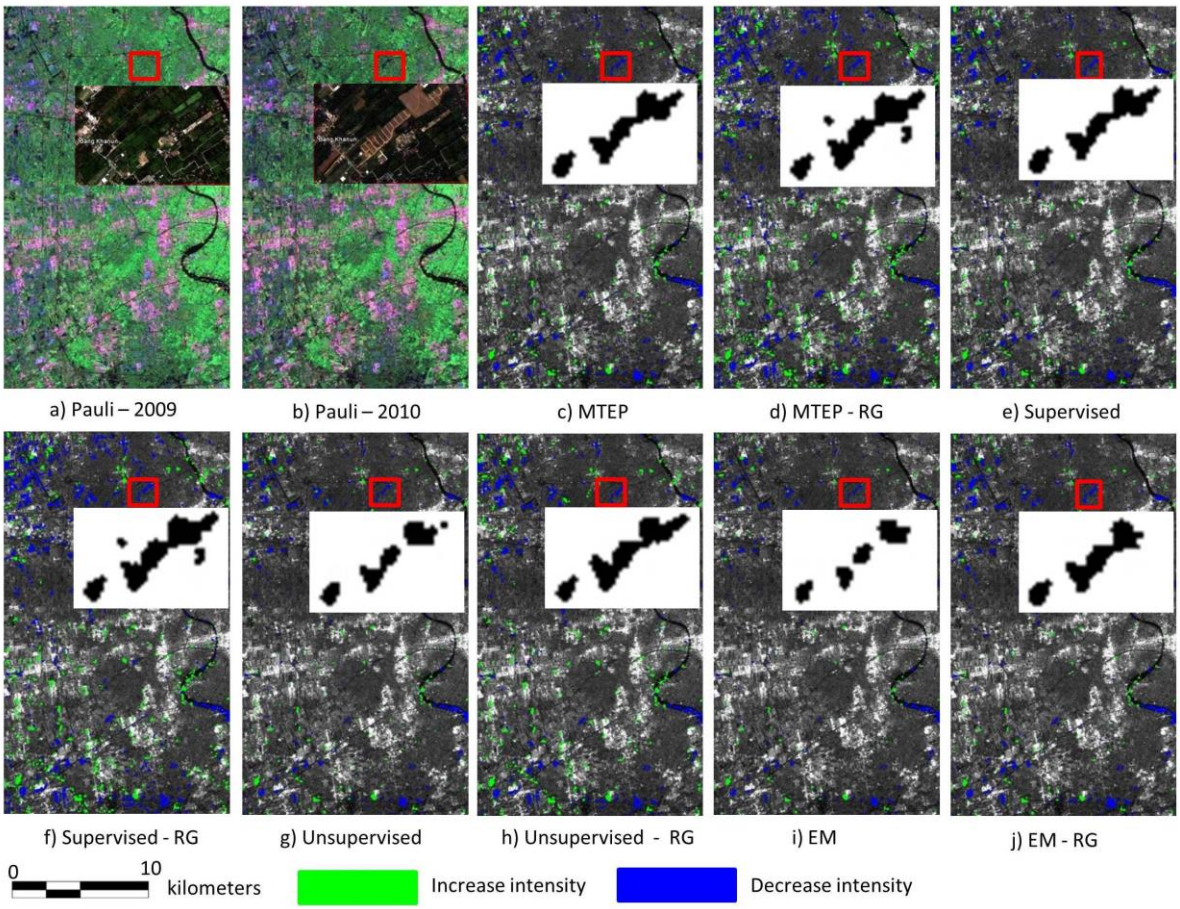

Figure 3.13 Change map in Bangkok. (a), (b) Pauli composition of PolSAR image, (c) – (j) Change map obtained from several methodologies, and corresponding zoom in map for a selected site.

The same kinds of misclassification can be seen in the Bangkok as in the Ho Chi Min City. Similar to the previous experiment, the accuracy of the unsupervised and supervised classification is low when the threshold values alone are used. The reason for the higher error resulting from using the threshold value alone is that the change area may not have a clear variation in the backscattering intensity in the pre and post-event images to separate changes. However, while implementing the coupling of thresholding with the region-growing algorithm, such kinds of misclassification get reduced. In addition, it appears extremely effective in the boundary region.

3.4.4. Overall discussion

The performance of both of the methodologies proposed is higher than that obtained by using the EM under the assumption of lognormal distribution [16] and a very similar to MTEP in all experiments including simulated image. The assumption of same distribution in both change area and no-change area [6], [16], [20] may not be valid in all the cases. It depends on the change area, size, and amount of variations in the intensity and nature of the change etc. Thus, the EM method cannot give stable threshold values in different cases. In contrast to that, while using the NDR operator, the assumption of normal distribution in no-change area is rather stable. And, the methodologies proposed do not need any predefine distribution in the change area.

The coupling of the thresholding and region-growing algorithm appears to be very effective in all experiments performed here in this paper. The accuracy obtained in simulated image is higher than that obtained in real images associated with the geographical locations, however the pattern of the performance improvement while implementing the proposed methodologies is similar. The kappa coefficient is increased by 0.05 in unsupervised, and 0.06 while using the supervised methodology in Ho Chi Minh City. Similarly, in Bangkok, the improvement is better than that in Ho Chi Minh City, it is improved by 0.13 in comparison to the traditional EM method.

The thresholding algorithms give a threshold value on either side of the no-change area. But, these threshold values unlikely give perfect results. Therefore, inclusion of the spatial information is instrumental in improving the performance for each methodology. As in Fig. 3.5, if we move the t_1 left, the probability to misclassify

the no-change to change will decrease but, the probability to misclassify the change into no-change will be increased, and vice versa while moving it to the right side. A similar result can be seen if we move t_2 to the left or right. Therefore, the threshold value alone cannot give the best result and coupling of thresholding with region growing algorithm is more effective if there is higher missing and false alarm in thresholding only. The methodology proposed would be promising solution that includes the spatial information along with the thresholding. The methodologies proposed are effective in those regions where the pixels are in higher risks to misclassify, especially along the edge of the change area.

3.5. Conclusions

In this research, one supervised and one unsupervised change detection methodology under the mixed distribution (normal distribution in the no-change area and no assumption for the change area) with the coupling of the thresholding and the region-growing algorithm are proposed. Effectiveness of the methodologies proposed in detecting the change area was confirmed in simulated SAR images as well as real SAR images associated with the geographical locations – Ho Chi Minh City and Bangkok.

The main strengths of the proposed approaches are: 1) the change image generation through the NDR operator from multi-temporal SAR image. NDR image is characterized as a higher separability index than widely use ratio image for several change classes, they eventually improve the accuracy of the estimation of the optimum threshold, and depicts the Gaussian distribution in the no-change area, 2) both proposed thresholding methodologies are computationally easy and stable (they are independent to the distribution in the change area and the Gaussian distribution in the no-change area is rather stable), and 3) the coupling of thresholding and region growing algorithms enable to include the spatial information in the moderate to low resolution images and equally effective to both supervised as well as unsupervised thresholding algorithms.

Concerning the limitation of the methodology proposed, both methods are not able to detect the change, if that is not statistically significant. This fact is applicable to MTEP and EM thresholding as well. In the future, we intend to generalize the approach for all data types, like optical and multi frequencies SAR images.

4 SENSITIVITY ANALYSIS FOR L-BAND POLARIMETRIC DESCRIPTORS AND FUSION FOR URBAN LAND COVER CHANGE DETECTION

A fully PolSAR image allows the generation of a number of polarimetric descriptors. These descriptors are sensitive to changes in different land use and cover patterns. Thus, this chapter focuses: to identify the most effective descriptors for each change type and ascertain the best complementary pairs from the selected polarimetric descriptors; and, to develop an information fusion approach to use the unique features found in each polarimetric descriptor to obtain a better change map for urban and suburban environments. The change image generation approach proposed in the chapter 3 was adopted for the change image generation from each considered descriptors. Additionally, the change detection results were obtained by using the supervised thresholding method, which is also proposed in the chapter 3, for each descriptor. Finally, a polarimetric information fusion method based on the coupling of modified thresholding with a region-growing algorithm was implemented for the identified complementary descriptor pairs.

Chapter 4

4.1 Introduction

Information on land use and cover and the changing patterns of these data is always a hot topic because of its importance in several applications, including land policy development, site selection, and demographic and environmental issues at the national, regional, and global scale. Collecting the change information by ground-based survey is more accurate than any other method, but this is impractical to do regularly and at short intervals in a rapidly growing urban area. Thus, remote sensing is the best available technique to monitor these changes. The utility of synthetic aperture radar (SAR) images in change detection has already been proven for urban change detection and disaster monitoring [6], [18], [46], [59]. However, the full potential of Polarimetric SAR (PolSAR) images still needs to be explored.

The use of radar intensity information has been suggested for change detection rather than power correlation coefficients and phase differences between co-polarized channels [13]. Several studies have been published based on radar intensities [6], [13], [16], [18], [46], [59], but most of these studies were based on single polarimetric images rather than fully polarimetric images [6], [16], [18]. A fully polarimetric image allows the development of several descriptors by different image processing algorithms. The representation and fundamental methods are based on incoherent analysis, which works with an ensemble average of several pixels to give second order statics of polarimetric information [44]. This allows the generation of several very useful pieces of information and descriptors [42], [43] [60]. These descriptors could supplement the results derived from single polarization images by adding several unique features, reflecting the complex nature of man-made structures, that could be sensitive to different types of changes in urban environments.

The availability of several processing techniques and the possibility of generating several descriptors from fully PolSAR images have created a good opportunity to conduct a sensitivity study to find the most effective descriptors for detecting several types of change. In this study, we also identify the best pairs of complementary components of these polarimetric descriptors. Furthermore, we develop an information fusion approach to combine information from the unique features found in each polarimetric descriptor in order to generate a better change map for urban and suburban environments.

The data used and study area are described in Section II. Section III contains an explanation of the methodology followed in this study. In the first part, we discuss the processing technique used to generate the polarimetric descriptors, and in the second part, we discuss the proposed polarimetric fusion technique. The results are presented and discussed in Section IV. The discussion of the results includes the sensitivity analysis and results obtained from the fusion of selected complementary pairs of polarimetric descriptors. Finally, our conclusions are given in Section V.

4.2 Data used and study area

Ho Chi Min City, one of the fastest growing Asian cities, was selected for the study. Its location is shown in Fig. 4.1. To detect changed areas, two fully polarimetric images acquired by the Advanced Land Observing Satellite (ALOS) Phased Array type L-band Synthetic Aperture Radar (PALSAR) in April 2007 and

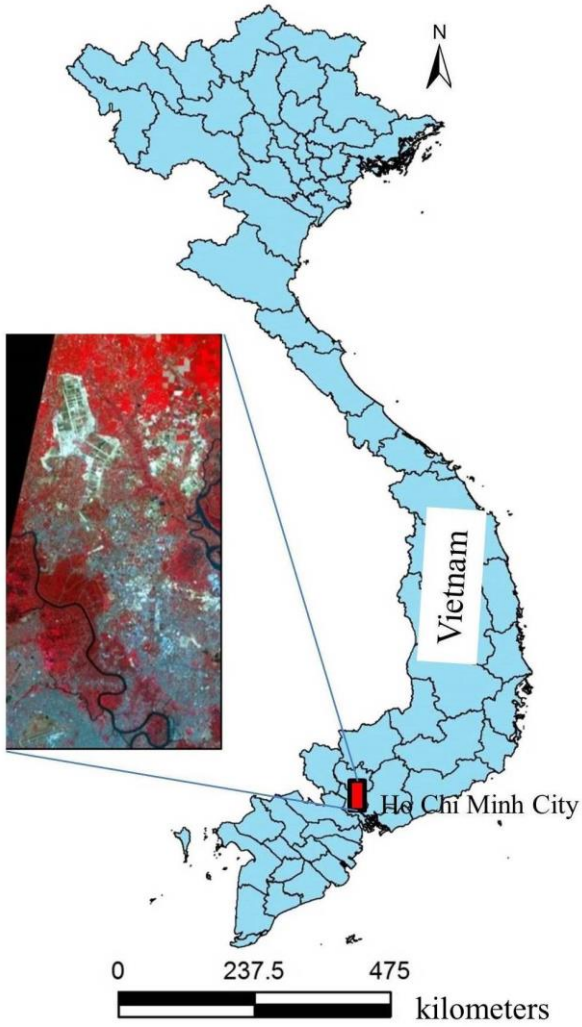

Figure 4.1 Study area.

April 2011 was used. To reduce the effects of phenological changes in vegetation and water content on the land surface, the images were acquired at nearly the same time of year. Additionally, both years selected had a normal precipitation pattern. Thus, all the changes detected in multi-temporal images are assumed to be related to human activity. All images were geocoded and co-registered to the Universal Transverse Mercator (UTM) system using the GDEM with 30 m spatial resolution. To confirm all possible types of change, a section of 605 × 1352 pixels that includes a core urban area and a rapidly expanding suburban area, was selected. To assess the accuracy of our approach, AVNIR-2 images acquired on nearly the same dates as the PALSAR images were used. In addition, high-resolution QuickBird images from Google Earth were used as a supplementary source to develop a reference change map.

4.3 Methodology

The process flow diagram of the sensitivity analysis and the fusion of polarimetric descriptors in multi-temporal PolSAR images is presented in Fig. 4.2. Details of the methodology are given in the following sections.

4.3.1 Generation of polarimetric descriptors

Several polarimetric decomposition methodologies are available to extract the physical scattering mechanism. In this study, we use descriptors obtained from different stages of the polarimetric processing: four polarimetric components (HH, HV, VH, and VV), the diagonal elements of the coherency matrix (T_{11}, T_{22}, and T_{33}), the eigenvector-based descriptors alpha (α), and Entropy (H) [45], and three physical scattering components, surface scattering (P_S), double bounce (P_D), and volume scattering (P_V) [42], [43].

The PolSAR data consist of complex scattering values, which can be represented by the 2 × 2 scattering matrix shown in Eq. (4.1).

$$S = \begin{pmatrix} S_{HH} & S_{HV} \\ S_{VH} & S_{VV} \end{pmatrix} = \begin{pmatrix} a & b \\ b & c \end{pmatrix} \qquad (4.1)$$

For mono-static radar imaging of a reciprocal medium, we have $S_{HV} = S_{VH}$ [44].

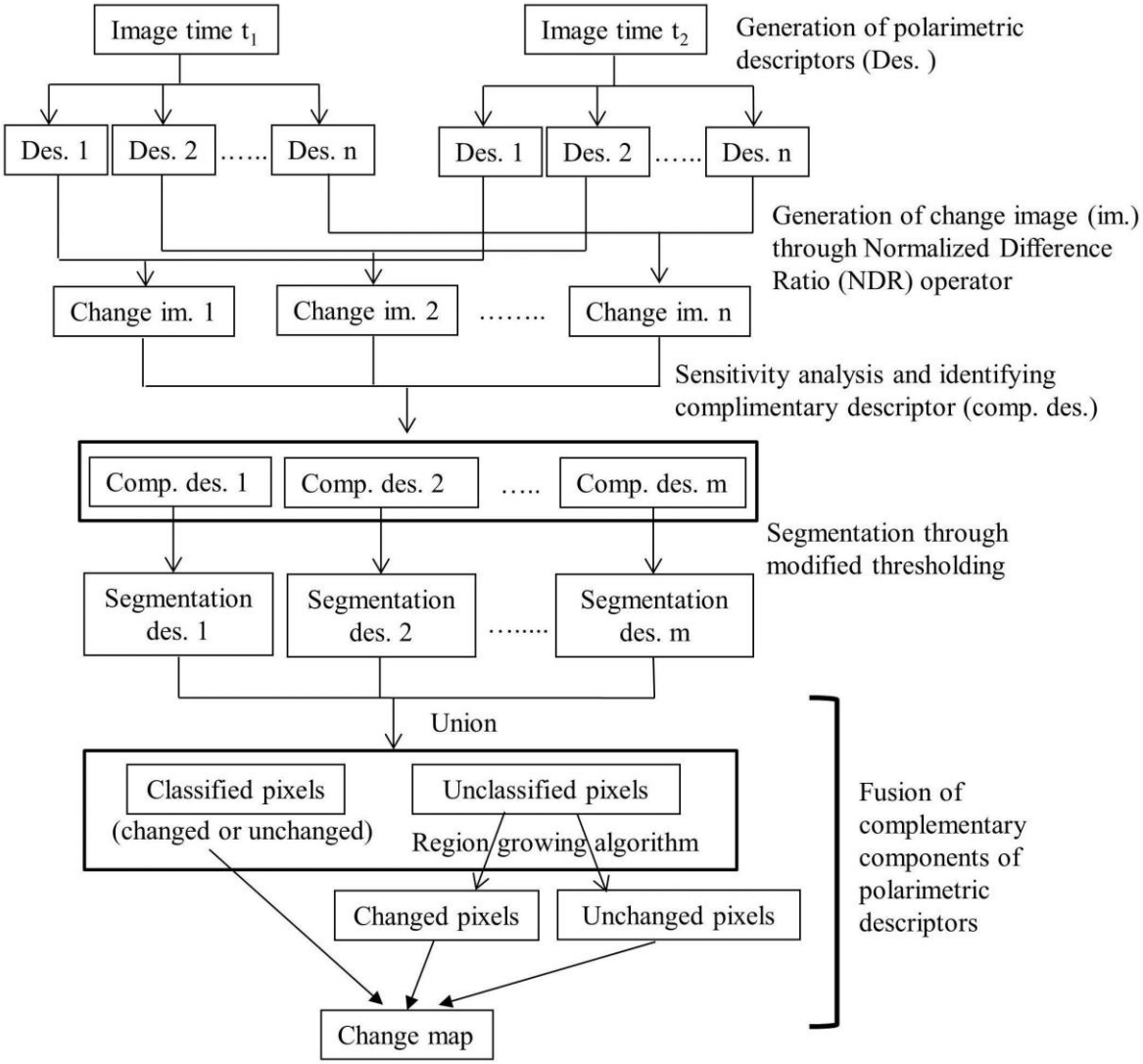

Figure 4.2 Process flow diagram.

In a multilook PolSAR image, each pixel is represented by a 3 × 3 coherency matrix.

$$T = \begin{pmatrix} T_{11} & T_{12} & T_{13} \\ T_{21} & T_{22} & T_{23} \\ T_{31} & T_{32} & T_{33} \end{pmatrix} = \begin{pmatrix} |a+b|^2 & (a+b)(a-b)^* & 2(a+b)c^* \\ (a-b)(a+b)^* & |a-b|^2 & 2(a-b)c^* \\ 2c(a+b)^* & 2c(a-b)^* & 4|c|^2 \end{pmatrix} \quad (4.2)$$

where * represents the complex conjugate operation.

The value of H obtained from a Cloud and Pottier alpha-entropy (α-H) decomposition of the coherency matrix [8] defines the roughness of the scattering: H = 0 indicates a single scattering mechanism, while H = 1 indicates a random mixture of scattering mechanisms. The scattering angle (α), representing the mean scattering mechanism, is a continuous angle ranging from 0° to 90°. In a model-based approach,

the scattering matrix is decomposed into the physical scattering components P_S, P_D, and P_V [42].

4.3.2. Change image development

The NDR operator is used to generate the change image. The NDR operator is defined as eq. 4.3.

$$change_{i,j} = \frac{im2_{i,j} - im1_{i,j}}{im2_{i,j} + im1_{i,j}} \tag{4.3}$$

where, *im*1 and *im*2 are co-registered polarimetric descriptor generated from PolSAR images acquired on two dates, and *i* and *j* are the X and Y coordinates of pixels in the images. This operator was introduced by Coppin and Bauer in [61] and later used on optical images in [62] and on SAR images in [14]. The NDR operator is better for change detection than other traditional operators [14] because the NDR image has less errors than an image produced by difference or ratio operator. We now compare the errors generated from NDR and ratio operator. Let's rewrite Eq. (4.3) as:

$$y = \frac{x_2 - x_1}{x_2 + x_1} \tag{4.4}$$

where, y is the image generated from NDR operation, x_1 and x_2 are the SAR backscattering magnitude at two dates. According to the law of error propagation, the variance of NDR operator, σ_y^2, can be derived as follows:

$$\sigma_y^2 = \left\{\frac{d}{dx_1}\left(\frac{x_2 - x_1}{x_2 + x_1}\right)\right\}^2 \sigma_{x_1}^2 + \left\{\frac{d}{dx_2}\left(\frac{x_2 - x_1}{x_2 + x_1}\right)\right\}^2 \sigma_{x_2}^2$$

$$= \frac{4x_2^2}{(x_2 + x_1)^2}\sigma_{x_1}^2 + \frac{4x_1^2}{(x_2 + x_1)^2}\sigma_{x_2}^2.$$

Let's assume that the variance of $x_1, \sigma_{x_1}^2$, and x_2, $\sigma_{x_2}^2$, are equal and substitute them by σ_x^2.

$$\frac{\sigma_y^2}{\sigma_x^2} = \frac{4(x_2^2 + x_1^2)}{(x_2 + x_1)^4} \tag{4.5}$$

Similarly, the ratio operation is defined as:

$$z = \frac{x_2}{x_1} \tag{4.6}$$

where, Z is the image generated from ratio operation, x_1 and x_2 are the backscattering magnitude at two dates. According to the law of error propagation, the variance of ratio operator can be calculated as follows:

$$\sigma_z^2 = \left\{\frac{d}{dx_1}\left(\frac{x_2}{x_1}\right)\right\}^2 \sigma_{x_1}^2 + \left\{\frac{d}{dx_2}\left(\frac{x_2}{x_1}\right)\right\}^2 \sigma_{x_2}^2 = \frac{x_2^2}{x_1^4}\sigma_{x_1}^2 + \frac{1}{x_1^2}\sigma_{x_2}^2 = \frac{x_2^2\sigma_{x_1}^2 + x_1^2\sigma_{x_2}^2}{x_1^4}.$$

Similar to the NDR operation, $\sigma_{x_1}^2$ and $\sigma_{x_2}^2$ are assumed to be equal and substituting them by σ_x^2.

$$\frac{\sigma_z^2}{\sigma_x^2} = \frac{(x_2^2+x_1^2)}{x_1^4} \tag{4.7}$$

Dividing Eq (4.5) by Eq (4.7)

$$\frac{\sigma_y^2}{\sigma_z^2} = \frac{4(x_2^2+x_1^2)}{(x_2+x_1)^4} \times \frac{x_1^4}{(x_2^2+x_1^2)} = \frac{x_1^4}{(x_2+x_1)^4}. \tag{4.8}$$

The right hand side of Eq. (4.8) is less than 1 for all value of $x_2 > 0.414x_1$. This suggests that the variance of ratio operator is smaller than the variance of NDR operator only if the backscattering intensity is decreased heavily i.e $x_2 < 0.414x_1$. This fact is presented in the Fig.4. 3 generated by plotting the contour line using Eq. (4.8). It is shown that a very small area has the ratio higher than 1, that means ratio operator is better than NDR in very limited combination of x_1 and x_2. As the probability of

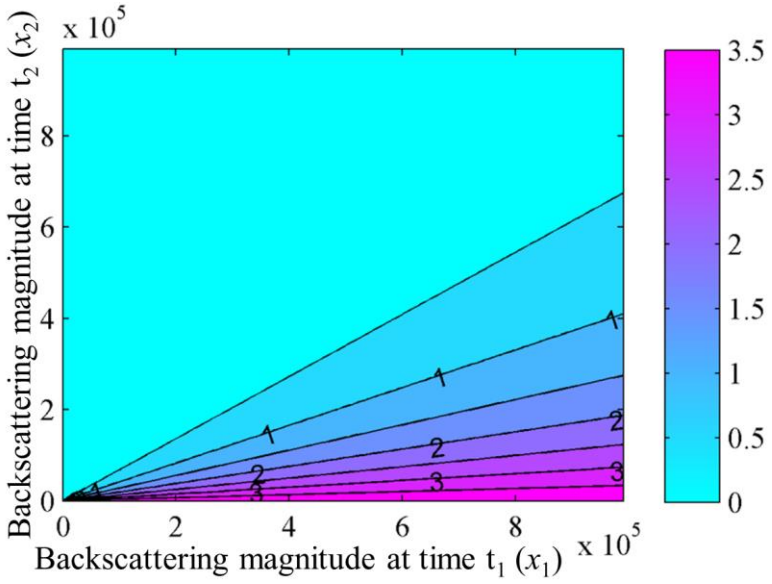

Figure 4.3 Contour map of ratio of error propagation in NDR and ratio image.

error in detecting changes increases with the variance [18], the NDR method produces a less error than the ratio method. Therefore, NDR operator has been adopted in this study.

4.3.3. Sensitivity analysis

Two approaches were considered for sensitivity analysis: the first is the analysis of separability index for several selected changed areas for each polarimetric descriptor; the second is change mapping using a single polarimetric descriptor.

4.3.3.1 Separability index

The separability index of a descriptor indicates the degree of separability of that descriptor. It is computed from Eq. (4.9) [53].

$$Separability\ index = \frac{|\mu_c - \mu_{uc}|}{\sigma_c + \sigma_{uc}} \quad (4.9)$$

here, μ_c and σ_c are the mean and standard deviation of the change class, and μ_{uc} and σ_{uc} are the mean and standard deviation of the no-change class. The descriptor with the highest separability index is the best to use for change detection. Four major change classes—bare land to built-up, agriculture to built-up (under construction), deforestation, and agricultural to bare land (smoothing of agricultural land) — were analyzed.

4.3.3.2 Change mapping through supervised thresholding using a single polarimetric descriptor

By assuming a Gaussian distribution of no-change areas in the change image generated by the NDR operator, a threshold value was identified in a supervised manner. The NDR image allows a clear preliminary assessment of changes by simple visual inspection. Fig. 4.4 shows the NDR image for the HH polarimetric component. Bright areas indicate increased backscattering intensity, whereas dark areas indicate decreased backscattering intensity. The majority of the area is moderately bright or dark and is composed of those pixels having values around 0. This area is characterized as the no-change (smooth) area. Thus, it is easy to recognize clusters of no-change cluster by visual inspection (Fig. 4.4).

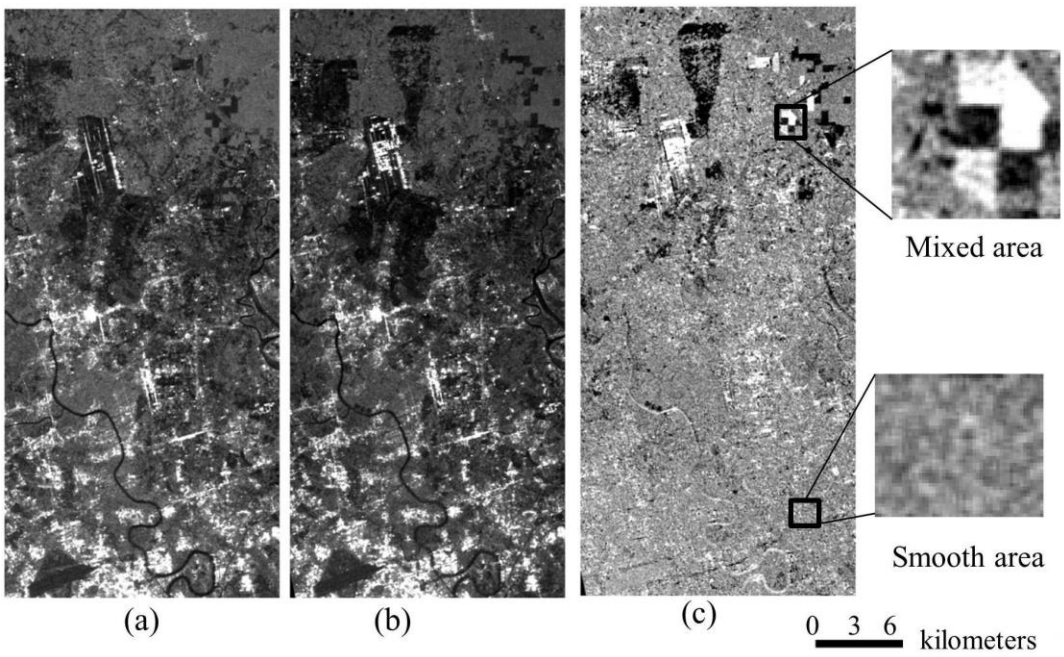

Figure 4.4 Change image generation using the NDR operator. HH component of PolSAR images (a) taken in 2007, (b) taken in 2011 and (c) the change image.

Several sample no-change clusters in the change image were selected manually. Because the pixels in the no-change area are normally distributed, $\mu \pm 3\sigma$ covers 99.7% of the total population of the sample no-change area, and those values can be used as threshold values to separate no-change areas from changed areas. Thus, if the sample no-change area has mean (μ) and standard deviation (σ), the threshold values can be computed as.

$$Threshold = \begin{cases} Left\ Threshold\ (t_1) = \mu - 3\sigma \\ Right\ Threshold\ (t_2) = \mu + 3\sigma \end{cases} \quad (4.10)$$

The remaining 0.3% of pixels in the sample no-change area are considered to be outliers. The advantage of this method is that no assumption is required about change areas. This method appears to give nearly the same results as the manual trial-and-error procedure, but it strongly depends on the selected sample.

With the inherent problem of the supervised methodology, the accuracy of this method is also greatly depends on the selected sample. However, due to the implementational advantage of the image generated by NDR operator, that allows a clear preliminary assessment of the change area by simple visual inspection, a sufficiently large number of sample no-change pixels are possible to select. Thus, the threshold range is unlikely to shift significantly.

A change in the land use or cover pattern alters the backscattering mechanism, and thus changes the backscattering intensity. For example, changing from bare land to a built-up area changes the backscattering mechanism from surface to double bounced reflection, which causes an increase in backscattering intensity. Similarly, deforestation changes the backscattering mechanism from volume to surface reflection, thus decreasing the backscattering intensity. Because such backscattering mechanisms are known for each feature, we assume the terms "increase in backscattering intensity" and "decrease in backscattering intensity" always have the same meaning for different features. However, this assumption may not be valid for α and H. Changes in pixels located beyond the left threshold obtained from Eq. (4.10) are attributed to a decrease in backscattering intensity and those located beyond the right threshold are attributed to an increase in backscattering intensity.

4.3.4. Proposed polarimetric fusion by considering spatial information for change detection

We propose the fusion of several descriptors, to be effected by coupling thresholding with a region-growing algorithm that considers spatial information. If we have threshold values t_1 and t_2 ($t_1 < t_2$) obtained from Eq. (4.10), we can compute the mean (μ) and standard deviation (σ) of values falling within this threshold range. It is empirically found that a majority of false alarms come from $t_1 \pm \sigma$ or $t_2 \pm \sigma$; that is, from the overlap of the histograms of the change and no-change classes, as shown in Fig. 4.5. Thus, the threshold values were modified to mitigate this effect. The pixels in the range $t_1+\sigma$ to $t_2-\sigma$ are classified as belonging to the no-change group. Similarly, pixels with value less than $t_1-\sigma$ are classified as having a decrease in intensity and those with value greater than $t_2+\sigma$ are classified as having an increase in intensity. The remaining pixels, from $t_1-\sigma$ to $t_1+\sigma$ and from $t_2-\sigma$ to $t_2+\sigma$ remained unclassified [14].

The fusion process is explained here for the two descriptors case. This operation was carried out in two steps. First, the union operation was performed for all pixels classified by both descriptors; this operation is illustrated in Fig. 4.6. At this stage, we have two types of pixels: classified and unclassified. The classified pixels are a member of one of three classes C_1, C_2, or C_3, which represent no change, increased intensity, and decreased intensity, respectively. The classified pixels are

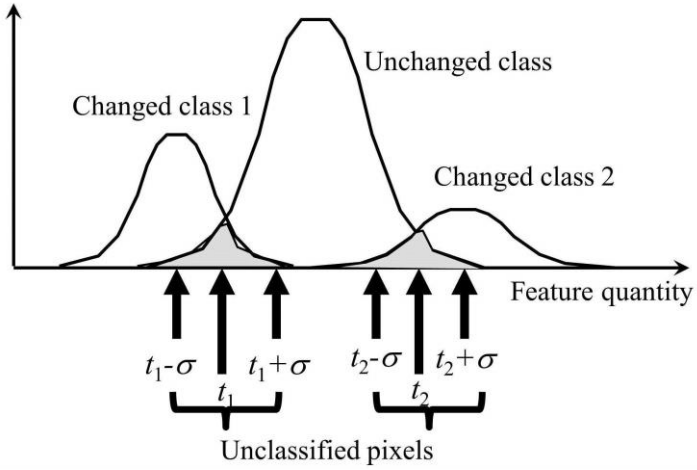

Figure 4.5 Modification of the thresholding algorithm.

treated as seed pixels, after which unclassified pixels are classified by a region-growing approach that operates locally.

Formally, let *U* represents the set of unclassified pixels. For all *x* in *U*, compute the distance (Δx_i) from each connected class as follows:

$$\Delta x_i = |g(x) - g_i(c)| \tag{4.11}$$

where, i = 1,2, or 3, $g(x)$ is the value of pixel x, and $g_i(c)$ is the average pixel value for each class. The connected class members are obtained from two time dilations of x.

We next obtain Δx_i for each descriptor to be fused. For *descriptor* 1, *decp*1*Inc*, *decp*1*Dec*, and *decp*1*Noc* are the distances of the pixel $x(i, j)$ to the increased intensity class, the decreased intensity class and the no-change class, respectively. Similarly, for *descriptor* 2, *decp*2*Inc*, *decp*2*Dec*, *decp*2*Noc*, are the distances to the increased intensity class, the decreased intensity class and the no-change class, respectively. Now, the overall distances of all classes from $x(i, j)$, considering both descriptors, is computed as follows:

$$\left.\begin{aligned} distInc &= decp1Inc + decp2Inc \\ distDec &= decp1Dec + decp2Dec \\ distNoc &= decp1Noc + decp2Noc \end{aligned}\right\} \tag{4.12}$$

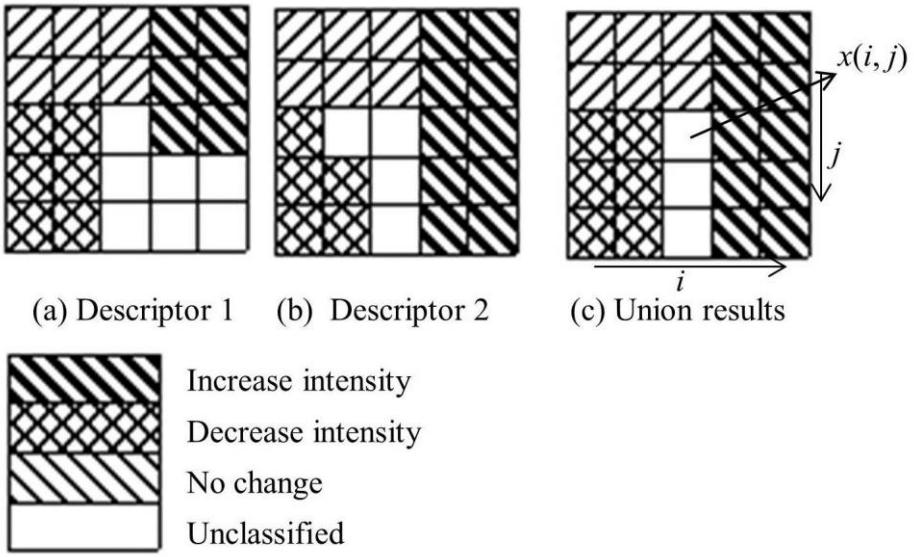

Figure 4.6 . Union operation of classified changed areas obtained from modified thresholding in a complementary pair of polarimetric descriptors. (a) Descriptor 1, (b) descriptor 2, and (c) results obtained by the union of areas classified in (a) and (b). Three pixels, $x(i, j)$, $x(i, j+1)$ and $x(i, j+2)$, are unclassified by both descriptors.

here, *distInc* is the overall distance of pixel $x(i, j)$ to the increased intensity class, *distDec* is the overall distance of $x(i, j)$ from the decreased intensity class, and *distNoc* is the overall distance of $x(i, j)$ from the no-change class.

Each unclassified pixel is assigned to the class that has the minimum distance from the pixel. This classification is similar to the *k*-minimum distance classifier. The process will be repeated as long as there is an unclassified pixel with at least two neighboring classes. The remaining pixels will be classified as no-change. This method can be extended to more than two descriptors in an analogous manner.

4.4. Results and discussion

The assumption of the null hypothesis, Gaussian distribution in no-change area, was verified with normal probability curve. And the effectiveness of the supervised thresholding was verified by comparing the performance with a parametric approach (minimum error thresholding) [16] and a non-parametric approach (Otsu thresholding)[63].

Given that the study area has the positive (increased backscattering intensity) and negative changes (decreased backscattering intensity). The resulting image generated through NDR operator will have multi-model histogram; therefore, theoretically derived PDF will not be able to model such dataset. Many previous work

with such kinds of datasets assumed a joint distribution and performed a statistical test for each area (changed and no-changed) in order to identify the approximate distribution. For example: in paper [6] a generalized Gaussian distribution was assumed and verified with the statistical test while implementing the logratio operator. The paper [46] concluded that three non-Gaussian distributions, Nakagami-ratio, Log-normal, and Weibull-ratio, for ratio image of the amplitude values of SAR images have similar performance. In another work [59] Gaussian distribution was assumed in both change and no-change area while using the difference operator and continuing without any test. Similarly, in [16] Nakagami and lognormal distributions are recommended in the image generated from modified ratio operator. Likewise, in order to test the null hypothesis that no-change areas are normally distributed, an NDR image generated from the HH component was subjected to analysis in this study.

The study area was divided into three subzones. The experiment was performed for four datasets, one for the whole study area and one for each of the three subzones. A normal probability curve fitting method was used to verify the Gaussian distribution in the sample no-change area selected from each zone. The results are presented in Figs. 4.7(a)–(d). Further, to show the range of $\mu \pm 3\sigma$ within the no-change area with respect to all areas, a Gaussian PDF is also shown for each zone (Figs.4. 7(e)–(h)). By using the same sample no-change pixels, threshold values were obtained for each zone; the change results are shown in Figs. 4.7(i)–(j). The results in all zones are very consistent and reasonable. From this analysis, it is clear that the no-change area can be stably approximated with a Gaussian distribution. Thus, the null hypothesis was not rejected for the HH component. We assume that other polarimetric descriptors also have the same statistical distribution. A detailed analysis of this approach is presented in [14].

Similarly, Fig. 4.8 (a) shows the change map obtained from the manual trial and error procedure (MTEP) thresholding, Fig. 4.8 (b) from supervised thresholding, Fig. 4.8 (c) from minimum error thresholding and 4.8 (d) from Otsu thresholding. The Kappa indices are 0.76, 0.74, 0.70 and 0.71 for MTEP, supervised method, minimum error algorithm and Otsu thresholding algorithm, respectively. The results obtained from minimum error thresholding has the lowest accuracy. The big missing alarm in both increased and decreased backscattering areas was identified, though the majority

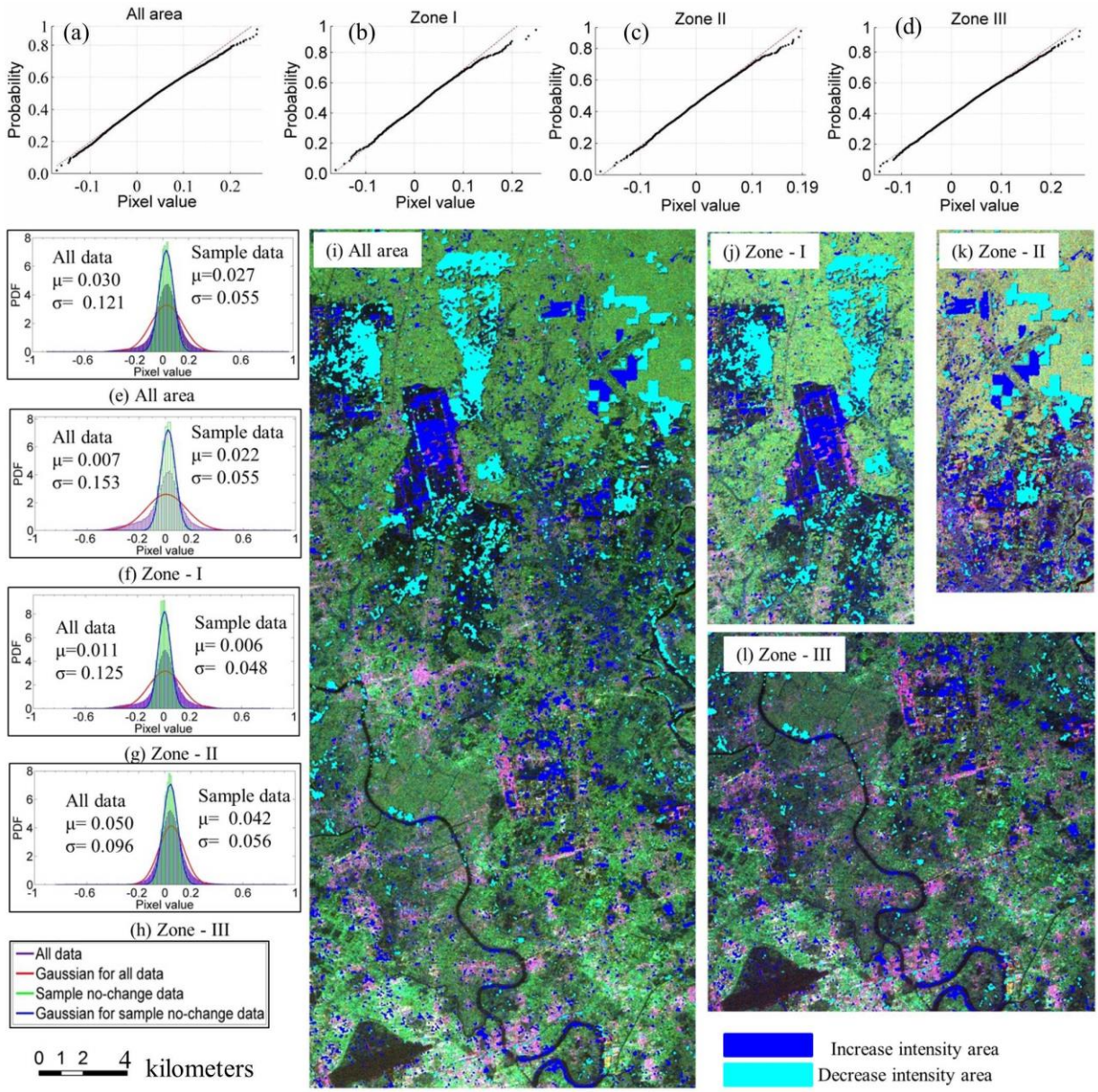

Figure 4.7 Test results for Normal distribution. (a) – (d) Normal probability curve for sample no-change area in each selected zone, (e) - (h) Gaussian PDF fitting for sample no-change area and whole area in each zone and (i)–(l) corresponding change results in each zone based on the threshold value obtained from the sample no-change pixels, overlaid with Pauli vector false color composite.

of error comes from decreasing backscattering area. While implementing the Otsu thresholding, it omits a large decrease backscattering area and gained a commission in an increased backscattering area. The major reasons behind the poor performance in minimum error are two folds: one is due to the inappropriate assumption of the same statistical distribution in both change and no-change classes, and the other is the uses of single thresholding values for detecting two types of changes (increased and decreased backscattering).

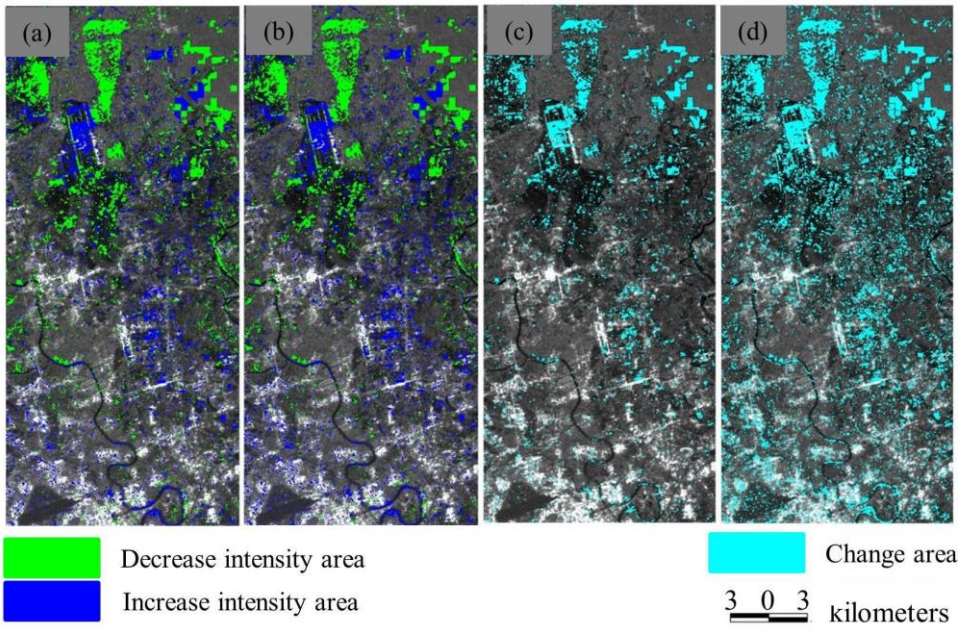

Figure 4.8 Change mapping using several methods - (a) MTEP, (b) supervised, (c) minimum error thresholding and (d) Otsu thresholding.

The Otsu thresholding approach also suffers from the same problem. When converting data into a single-tail statistic, the nature of the curve will differ from both tails and a single threshold value cannot perfectly judge both types of change. That is, what is good for one type of change (increased or decreased backscattering) will not be good for the other. In this case, a higher missing alarm rate in detecting decreased backscattering areas and false alarm in the increased backscattering area were identified even though the thresholding values obtained from Otsu algorithm is reasonable. In order to solve such problems: one tail problem, and the same distribution for change and no-change areas, a supervised thresholding methodology appear to be effective among three approaches. Therefore, we adopt the supervised thresholding method for sensitivity analysis and as a pre-processing for polarimetric fusion process.

4.4.1. Sensitivity analysis

4.4.1.1. Separability analysis

A separability index was computed from Eq.(4.9) for each major change classes (agriculture to under construction area, bare land to built-up area, deforestation, and agriculture to bare land area) across all considered polarimetric descriptors. The NDR images of each descriptor obtained from multi-temporal PolSAR images were subjected to analysis. Fig. 4.9 shows the separability index for

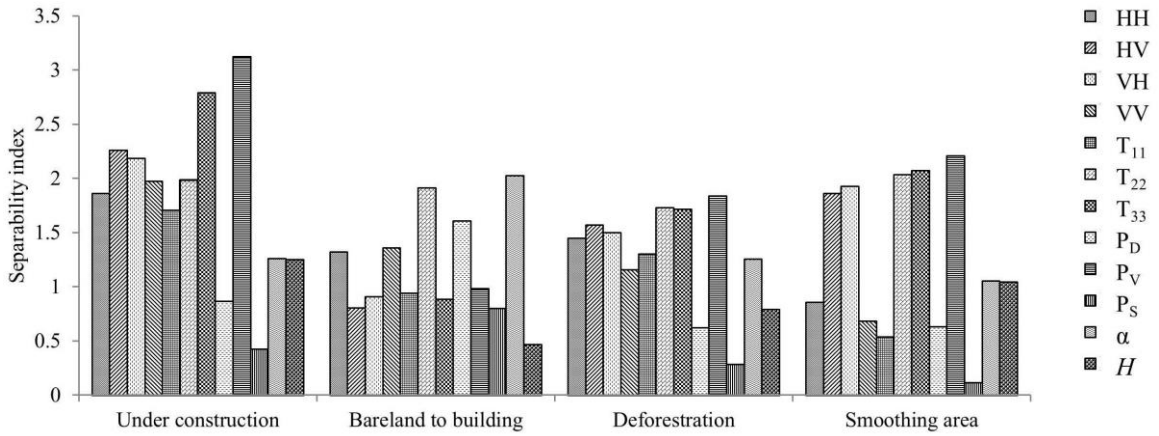

Figure 4.9 Separability index of different polarimetric descriptors in major change classes.

each descriptor in the selected change classes. Higher separability indexes indicate a better ability to detect changes.

In Fig. 4.9, it can be clearly seen that P_V, HV, and T_{33} have very similar indexes and are the highest in three change classes: agriculture to bare land (surface smoothing), construction, and deforestation. However, they are not good indicators for the change from bare land to built-up area. Some other descriptors appear better for detecting such changes. The descriptors α, T_{22}, and P_D appear to be better than any others for detecting bare land to building changes. If we consider the polarimetric components HH and VV, neither shows the highest separability index in any change class. However, they are moderately effective for each change.

Thus, from this analysis, what we can say is that a single descriptor cannot be equally effective for each type of change and some descriptors appear to be better for detecting specific types of change. Therefore, it is likely to improve the overall accuracy of change detection if we make use of complementary pairs: that is, use those polarimetric descriptors that have better separability indexes in a tight coupling. P_V, T_{33}, and HV are more sensitive to three of the major types of change (agricultural to bare land, deforestation, and construction). Similarly, T_{22}, P_D, and α are the most sensitive to changes in the dihedral structure. Hence, a complementary pair can be formed by taking one descriptor from each group.

4.4.1.2. Change detection from polarimetric descriptors and discussion

Fig. 4.10 shows change detection maps developed from pairs of polarimetric descriptors for April 2007 to April 2011 data. The accuracy assessment is summarized

in Table 4.1. Change detection results obtained from *H* and α are shown in Figs. 4.10 (c) and (d), respectively. The accuracy obtained from *H* is slightly better than that from α; however, the major sources of error are the same in both. Some specific change types, such as change from bare land to vegetation, are not detected by either descriptor, which leads to many missing alarms.

Figs. 4.10(e)–(h) indicate the changes in single channel backscattering measurements for HH, HV, VH, and VV polarizations, respectively. The results obtained from the co-polarization descriptors (HH and VV) are very similar. Likewise, the results from VH component are very similar to those of the HV component. The cross-polarization descriptors (HV and VH) give slightly different

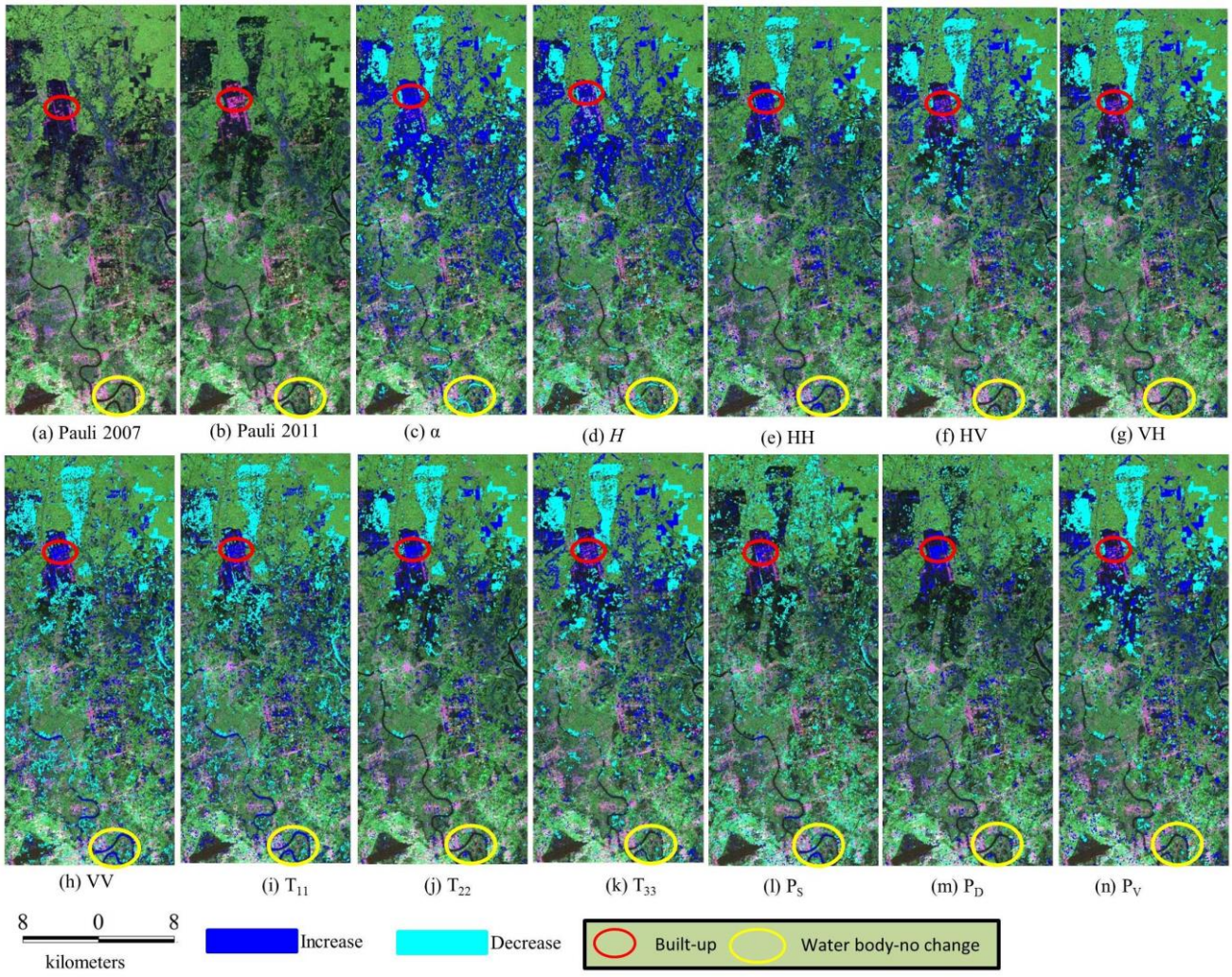

Figure 4.10 . Change map obtained from polarimetric descriptors. (a) – (b) False color composite of Pauli vectors generated from PolSAR images in 2007 and 2011, and (c) – (n) change detection maps derived from the various polarimetric descriptors by supervised thresholding method, overlaid with Pauli vector false color composite.

results from those obtained from the co-polarization channels. Some water bodies appear as change areas in HH and VV, as shown by a yellow circle in Fig. 4.10. However, they are not changed in the reference map. Wind direction, turbidity, and movement in the water body can alter the backscattering in SAR images. Although these assumptions were not verified, we treated these areas as no-change areas.

Among the model-based decomposition components (Figs. 4.10 (l)–(n)), the change detection map obtained from P_V exhibits the best detectability. The accuracy obtained from P_D is not comparable with that from P_V but it differs from P_V in the change types detected and thus they appear to complement each other. For P_S, false and missing alarms are more frequent, but it can detect some changes that are not detected by P_V or P_D. Some water bodies seen as changes are not really changed. The source of this false alarm is the same as for HH and VV. T_{11}, T_{22}, and T_{33} (Figs. 4.10 (i)–(k)) are nearly the model-based decomposition. T_{33} is very similar to P_V, but T_{22} mixes results from P_S and P_D. Even though it is close to P_D, T_{22} possesses the detection capability in P_S as well. This is because T_{22} is used for computing P_S, along with other polarimetric descriptors from the coherency matrix. Additionally, T_{11} also has the capability to detect changes that cause changes in P_S and P_D, but it is not as

Table 4.1 Comparison of urban and suburban change mapping accuracies from different polarimetric descriptors.

Descriptors	False alarm rate (%)	Increased intensity (%)	Decreased intensity (%)	Kappa coefficient
HH	11.96	84.6	66.41	0.73
HV	10.27	78.67	63.03	0.74
VH	10.52	78.97	62.9	0.74
VV	14.55	83.53	59.1	0.7
T_{11}	13.83	79.56	67.56	0.69
T_{22}	9.6	89.19	60.06	0.73
T_{33}	10.28	72.72	61.98	0.75
P_D	12.92	59.29	15.21	0.56
P_V	9.41	75.72	66.51	0.76
P_S	23.81	63.85	15.4	0.48
α	19.89	82.43	21.46	0.62
H	17.2	86.99	38.98	0.68

False alarm rate (%) – Percentage of falsely classified pixels.
Increased intensity (%) – Percentage of correctly detected increased backscattering intensity areas.
Decreased intensity (%) – Percentage of correctly detected decreased backscattering intensity areas.

robust. This is because T_{11} is one of the major contributors in the computation of P_S and P_D. The major source of error in T_{11} is the same as in P_S.

The accuracy assessment confirms that the frequency of missing alarms in P_D is significant. Decreased intensity areas, such as those with a change from agricultural land to bare land (smoothing area) and deforestation, are not sensitive to P_D, and thus have higher missing alarm rates. Similarly, several increased backscattering areas are under construction and thus clear dihedral structures have not been formed, resulting in significant changes in P_V rather than P_D. However, the false alarm rate is very low in P_D, and P_D is complementary to P_V and T_{33}. However, T_{22} is equally sensitive to the change from bare land to dihedral structures as P_D, but it is better than P_D for other kinds of changes, such as agricultural land to bare land or deforestation.

In contrast, T_{11} and P_S have some common information and they are complementary to $T_{22} \cup T_{33}$ and $P_D \cup P_V$, respectively, but a significant false alarm rate may cause a decrease in the overall performance if they are used in fusion with other descriptors. Therefore, the fusion of T_{22} and T_{33}, HH and HV, and P_D and P_V would be worthwhile to detect the diverse changes occurring in an urban and suburban environment and reduce the rate of false and missing alarms. Furthermore, HH and VV are interchangeable and, of course, HV, T_{33}, and P_V can replace each other. The accuracy of urban change detection by H and α is fairly good. However, the increase and decrease in H and α do not have exactly same meaning as increased and decreased backscattering from other polarimetric descriptors. Thus, they cannot be used to complement any other polarimetric descriptors.

In addition to single polarimetric descriptors, a polarimetric similarity test between two images was implemented. The likelihood ratio test statistic P can be given as.

$$P = In\left(\frac{|C_{avg}|}{|C_1|}\right) + In\left(\frac{|C_{avg}|}{|C_2|}\right) \tag{4.13}$$

where C_1 and C_2 are the covariance matrices corresponding to the images acquired at time 1 and time 2, respectively, and C_{avg} is $(C_1+C_2) / 2$.

Fig. 4.11(c) shows the change map developed from the likelihood ratio test statistic *P*. The overall kappa coefficient is 0.79, the overall detectability is 83% with a false alarm rate of 12%. The results are better than those of a single polarimetric descriptor, but they also fail to solve the false alarm problem for an unchanged water body. In addition to that, this technique is not very sensitive to changes from agricultural land to bare land, which causes a very small change in the overall scattering mechanism that is dominated by HV (P_V). The major disadvantages in this method arise from the single-tail curve generated by the likelihood ratio test statistic, as shown in Fig. 4.11(a). A single threshold value will distinguish change and no-change areas. Thus, it entails two types of deficiency. The first problem is that it can only distinguish between change and no-change areas, but not between increased and decreased backscattering. The second problem is the misclassification error. This arises because the change area is not symmetrical, as shown in Fig. 4.11(b). When converting such data into a single-tail statistic, the nature of the overall curve will differ from both tails, and a single threshold value cannot perfectly judge both types of change. That is, what is good for one type of change (increased or decreased backscattering) will not be good for the other. In this case, a higher missing alarm rate in detecting decreased backscattering areas was identified.

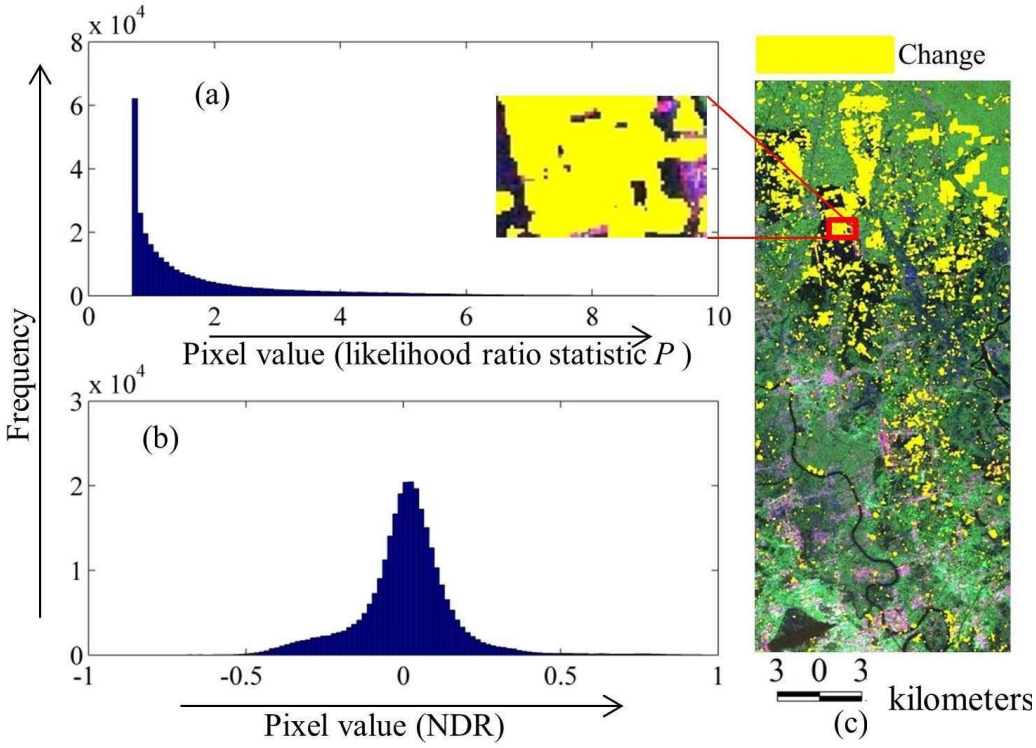

Figure 4.11 Results from likelihood ratio statistic. (a) Histogram of the likelihood ratio statistic (P), (b) histogram of the NDR image generated from the HH component, and (c) the change map derived from the likelihood ratio statistic.

4.4.1.3. Change mapping using complementary pairs of polarimetric descriptors

The polarimetric scattering mechanism analysis and change detection results obtained from different descriptors imply that several polarimetric descriptors provide complementary information about changes. Therefore, the performance of change detection can be improved by the fusion of several polarimetric descriptors. three independent sets of complementary couple namely {HH, HV (VH is considered equivalent to HV)}, {T_{22}, T_{33}}, and {P_D, P_V} were identified. Each member of each set is complementary to the other member of the same set and they are complete, i.e. can detect all changes that are sensitive to SAR backscatter. From the analysis, it is observed that HH and VV have similar responses to the various changes, therefore they may be used interchangeably. However, as HH and VV show very similar responses to most changes, they may be used interchangeably. T_{11} and P_S generate a high false alarm rate and, consequently, they may degrade the overall performance if used with other descriptors. Consequently, In addition, spatial information is also useful to improve change detection performance and so is considered here.

Thus, the results from using each of the three complementary pairs of polarimetric descriptors were evaluated independently. Fig. 4.12 shows the resulting change detection maps, and Table 4.2 gives the corresponding mapping accuracy. As all the descriptors come from the same data sources, the detected results do not seem to differ much visually. The overall accuracy assessment, based on the Kappa coefficient, shows that the results obtained from the fusion of T_{22} and T_{33} are better than all other fusion results. Even though the overall detectability is higher when considering T_{11} and P_S along with an appropriate complementary pair, their contributions to the false alarm rate greatly degrades the overall performance. The unchanged water body that is detected as a changed area by the fusion of HH and HV is the main source of the increase in the false alarm rate. Similarly, the changed features that cause changes in surface scattering are missing when using P_D and P_V only. In contrast to that, the fusion of T_{22} and T_{33} overcomes both the false alarm and missing alarm problems. The false detection of the water body was not seen in any of the T_{22} and T_{33} results. Additionally, as discussed in the previous section, it is T_{22}, that possesses the potential to detect the same changes as P_S and is responsible for the improvement of accuracy in the fusion of T_{22} and T_{33}.

Table 4.2. Change mapping accuracies with the fusion of several complementary sets of polarimetric descriptors.

Indicators	**HH & HV**	**T_{22} & T_{33}**	**P_D & P_V**
False alarm rate (%)	8.52	6.50	7.26
Increased intensity (%)	93.20	93.92	92.57
Decreased intensity (%)	79.19	80.14	78.05
Kappa coefficient	**0.81**	**0.85**	**0.83**

False alarm rate (%) – Percentage of falsely classified pixels.
Increased intensity (%) – Percentage of correctly detected increased backscattering intensity areas.
Decreased intensity (%) – Percentage of correctly detected decreased backscattering intensity areas.

The fusion of polarimetric descriptors improves the results in two ways, as we carried it out in two steps. The union operator is responsible for overcome the missing

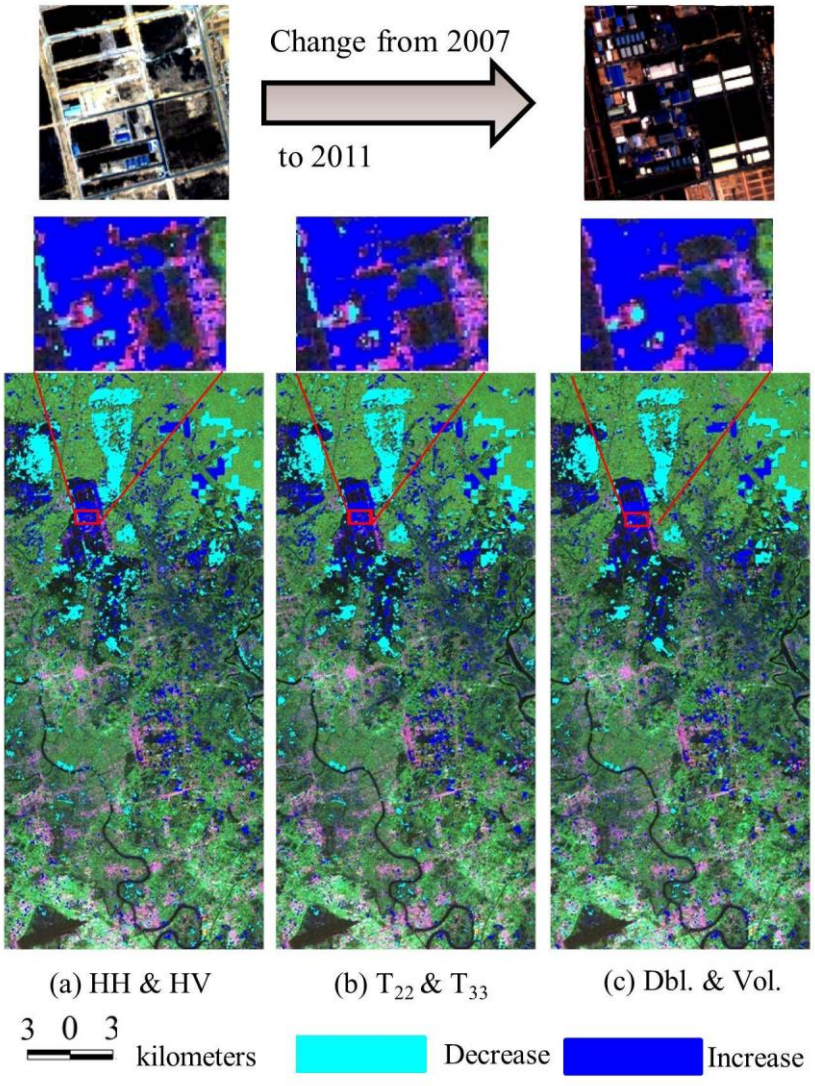

Figure 4.12 Change map obtained from the proposed fusion method (a) HH and VV, (b) T_{22} and T_{33}, (c) P_D and T_V, overlaid in a false color composite of Pauli vectors.

alarm problem by making use of the complementary characteristics of several descriptors. In addition, the classification of ambiguous pixels identified by modified thresholding and the union operation was done successfully through the region-growing algorithm, which was modified to use local information from all polarimetric descriptors considered in the fusion process. Thus, the accuracy of mapping large areas of urban change was notably improved, with a significant reduction in the missing and false alarm rates, by the fusion of complementary descriptors.

4.5 Conclusions and recommendations

Changes in the radar scattering mechanism for urban and suburban areas were investigated by using several polarimetric descriptors. Changes in radar backscattering from built-up areas are characterized by significant changes in P_D due to the presence of dihedral structures. T_{22} is also highly sensitive to these changes. All other descriptors revealed the same changes; however, they are not as effective. Deforestation is characterized by a significant decrease in P_V. In contrast, P_V was found to increase in built-up areas in which the structures were not clearly dihedral, such as buildings under construction, small houses with sloped roofs, and structures not aligned to the image orientation. In terms of separability, P_V and its family (HV and T_{33}) are sensitive to three major changes: deforestation, construction, and change from bushes or agricultural land to bare land. The descriptors *H* and α could identify changed areas; however, they were not able to distinguish clearly between areas of increased and decreased intensity. Moreover, they do not have any complementary descriptors.

A supervised change detection approach was applied to various polarimetric descriptors. The accuracy assessment results indicated that single polarization observation can give a kappa coefficient up to 0.74, and a single polarimetric descriptor up to 0.76. These results match the characteristics obtained from separability index. Thus, the fusion of polarimetric descriptors is important to optimize performance.

The major aim of this research is to obtain a change map that allows the separation of both types of change areas (increased and decreased intensity) from unchanged background. To achieve this, a new polarimetric information fusion approach based on the coupling of thresholding and a region-growing algorithm was

implemented for several complementary pairs of descriptors. The contextual fusion of T_{22} and T_{33} gave the best change detection results for urban and suburban environments, with a kappa coefficient of 0.85 and a significant improvement in the false and missing alarm rates.

The supervised thresholding algorithm adopted in this study was tested for only ordinary changes and not for changes resulting from a disaster, in which most of the area could be affected by the disaster and it may be difficult to find an appropriate no-change sample. Therefore, we strongly recommend caution when considering the use of this supervised thresholding algorithm to monitor disaster effects. Additionally, it should be noted that apparent changes may occur in water bodies due to turbidity or different air directions. Users should carefully examine any changes to a water body.

5 OPTICAL AND SAR DATA INTEGRATION FOR AUTOMATIC MULTI-CLASS CHANGE DETECTION

Automatic change pattern mapping in urban and sub-urban area is important but challenging due to the diversity of urban land use pattern. With multi-sensor imagery, it is possible to generate multidimensional unique information of earth surface features that allow developing a relationship between a response of each feature to SAR and optical sensors to track the change automatically. Thus, a SAR and optical data integration framework for change detection and a relationship for automatic change pattern detection were developed. It was carried out in three steps: (i) computation of indicators from SAR and optical images, namely: normalized difference ratio (NDR) from multi-temporal SAR images and the normalized difference vegetation index difference (ΔNDVI) from multi-temporal optical images, (ii) computing the change magnitude image from NDR and ΔNDVI and delineating the change area and (iii) the development of an empirical relationship, for automatic change pattern detection.

The development of compatible indicators from multi-sensor images is very important, and ΔNDVI and NDR have a very good matching and thus we can use these indicators as a complementary to each other. The NDR operator was developed and proposed in chapter 3 and implemented in chapter 4. Additionally, the change mapping approach is also adopted from chapter 3 and chapter 4.

5.1 Introduction

As hundreds of thousands of people are migrating from rural to urban area every year, land cover/use classes in urban and suburban areas are changing rapidly and this trend is likely to increase in future. In addition to that, several human interventions such as agricultural practice, deforestation, reforestation, dam construction etc. also make big changes in the Earth`s surface. Thus, continuous monitoring is very important in several aspects including infrastructure planning and development to Environmental monitoring, etc. Change information detected from the multi-temporal remote sensing images is seemed to be extremely useful [13], [64], [14], [15], [25]. Mainly, optical and radar images have been being used for change detection independently as well as in a combination with each other or with ancillary datasets derived from other sensors like LiDAR or field based surveying. Currently, mainly three types of change detection procedure were in practice namely, binary change detection [5], [1], [6] multi-class change detection [7], [8] and change detection in long time series of images [10] [9].

For the binary change detection, several supervised and unsupervised methods for multi-temporal optical, SAR or fusion of both images have been developed and published in several journal articles. The most common way for change detection using optical images are: image differencing (ID) and followed by thresholding [1], [5], [6]. The NDVI is the major index while the change in vegetation is a major concern [9], [10]. However, while considering all kinds of changes the change vector analysis (CVA) with Tasseled cap transformation is one of the most common approaches [1], [5], [8] for multi-spectral images. The basic idea for change vector analysis is to subtract the vector generated from a multispectral image in one date to that with another date [7]. The changed and unchanged classes were then segmented through the threshold value of the vector magnitude image [5], [8]. The threshold values were identified either empirically or unsupervised theoretical thresholding strategy [6]. The CVA is recommended for change detection from a comparative study done by [11] among the most common for methods including: image differencing, image rationing, image regression, and CVA. In addition to that the CVA is able to detect the change direction automatically [65].

Because of the several inherent shortcomings in optical imagery, for example weather and light condition, etc., SAR images are being used as an alternative sources. They are less exploited in comparison to the optical images [6], this may be due to the complexity caused by speckle noise or may be the unavailability to common users. In spite of the less exploit, SAR images have already proven their usability for urban change detection because of their unique features and operational advantages over optical imageries. Several very good methods can be found for the automatic change detection through the SAR images [6], [13], [14].

A research done by Dierking and Skriver suggested that the intensity images were better for change detection than phase difference and correlation coefficient between the multi-temporal co-polarized images [13]. They used the ratio operator to obtain the change image and decision mechanisms based on a desired value of probability of false alarm. Paper [6] presents an automatic change detection approach based on Generalized Gaussian model. They used the log-ratio operator to obtain the change image and the threshold value was obtained using the Kittler-Illingworth minimum-error thresholding by assuming the Generalized Gaussian model. In paper [14] used the normalized difference ratio (NDR) operator for the change image generation. They suggested NDR operator rather than ratio for the change detection. Additionally, coupling of the region-growing algorithm with the thresholding in order to use the spatial information that improves the detectability in the boundary line was also suggested. However, due to the speckle noise and some inherent features of different wavelength signal, even SAR images are not able to provide the best change detection results and hence is subjected for a continuous research topic in order to improve the performance.

With the availability of multi-sensor images and their unique signature for each ground feature, potentially new research scope was created to enhance the change detection and labeling automatically. Accordingly, to use the complimentary information from multi-sensor images, several data fusion techniques have already been in practice. Data fusion of multi-sensor optical imagery has been exploited widely. Majority of such fusion techniques is motivated to pan sharpening [23]–[26]. The most common pan-sharpening methods include: an intensity-hue-saturation (IHS) transformation [27] , principal component Analysis (PCA) [24], High Pass Filter [26]. and wavelet transformation (WT) [23].

Even though, SAR and optical image fusion is not widely exploited in comparison to the multi-sensor optical images, some good approaches are already in practice. The motivation behind these fusion approaches is also to enhance the spatial resolution by preserving spectral information [25], [28]. In addition to that, SAR and optical fusion is driven from better land cover classification or some specific structure detection. [66] T have used the SAR and optical data for building outline detection using feature based fusion approach in one of their studies. Their study showed that SAR images are capable to show the building presence and optical images are good for the shape delineation – complementary information about building presence and proper shape extraction. They carried out it in two steps: first, extraction of partial potential building footprints on the SAR image and then shape detection in the optical one.

Hong et al. in [28] proposed a fusion method based on wavelet-IHS transformation for SAR and optical MS images that was mainly motivated to preserve the spectral information of MS images and spatial detail of high resolution SAR image. [29], in another work for grassland and alfalfa segmentation, the same fusion technique was implemented. The fusion results gave spatial details of relatively high spatial resolution SAR imagery and spectral detail was obtained from low-resolution Moderate-resolution Imaging Spectroradiometer (MODIS) imagery. Major concern was again to improve the spatial detail.

In another research, McNaim et al integrated optical and SAR imagery for developing annual crop inventories [30]. They used two SAR (Envisat ASAR) and one optical (Landsat 5) imagery for crop classification and achieved above 80% of accuracy. The work was motivated to reduce the risk associated with operational implementation even though three optical imagery gives acceptable results. Multi-temporal SAR images alone are unable to achieve such high accuracy. Due et al. [25] integrates the pan sharpening and decision level fusion to develop a new change detection framework based on two-stage sequential fusion. And, others mainly work on the pixel level or decision level fusion.

As presented in previous paragraphs, several data fusion techniques are available which allow better analysis and interpretation by making use of complimentary information, however authors have not yet found even a single work

motivated from automatic change type detection and very few fusion works were inspired by the change detection [25], [28], [67].

In addition to binary change detection, some works were inspired by automatic multi-class change detection [7], [8].They are mainly based on change vector analysis on MS images but the discriminated classes are very limited due to the lack of enough information. Even though CVA is not well appreciated for multi-class change detection, it successfully makes use of MS information for change detection. Therefore, CVA could be a very good approach for information fusion that can be obtained from optical and SAR imagery so that the overall detectability can be improved in comparison to MS or SAR images only for the change detection. It is known that the unique signature of SAR and optical images for each land use/cover feature is stable and site independent, in the similar weather and light condition for optical imagery and same frequency in case of SAR images, it is possible to develop a relationship between them and can deploy for an automatic change tracking.

In this study, an empirical relationship is developed by using the unique response from major features in the Earth's surface in SAR and optical imagery and deployed for automatic multi-class change detection. Before that, a change area is segmented through CVA based SAR and optical information fusion. The fusion is motivated to use the complimentary information without losing the inherent information that comes from either SAR or optical images for better change detection. Specifically, it is expected to improve the sharpness of the detected feature, or be able to detect the changed features that are otherwise not possible from a single data source.

5.2 Study area and data used

5.2.1. Study area

For an experimental purpose, a section of 636×675 pixels (19×20 km) in an outskirts part of Ho Chi Min City was selected. Almost 19% of the selected area was changed during the considered study period (2007 to 2011). The major events occurred in the area was constructions, deforestation and smoothing of agricultural land that causes the changes on agricultural land to bare land (preparing for construction), forest to bare land, bare land or agricultural land to built-up area or

under-construction area. These are believed to be the major changes while expanding the urban area all over the world; therefore, study in this site is likely to be useful for other parts of the World. Fig. 1 shows the study area.

5.2.2 Data used

HH component of two fully Polarimetric Synthetic Aperture Radar (PolSAR) images acquired by the Advanced Land Observing Satellite (ALOS) Phased Array type L-band Synthetic Aperture Radar (PALSAR) in April 2007 and April 2011 were used. Similarly, the Landsat-7 band 3 (Visible Red) and band 4 (Near InfraRed) acquired by the Enhanced Thematic Mapper Plus (ETM+) images nearly the same

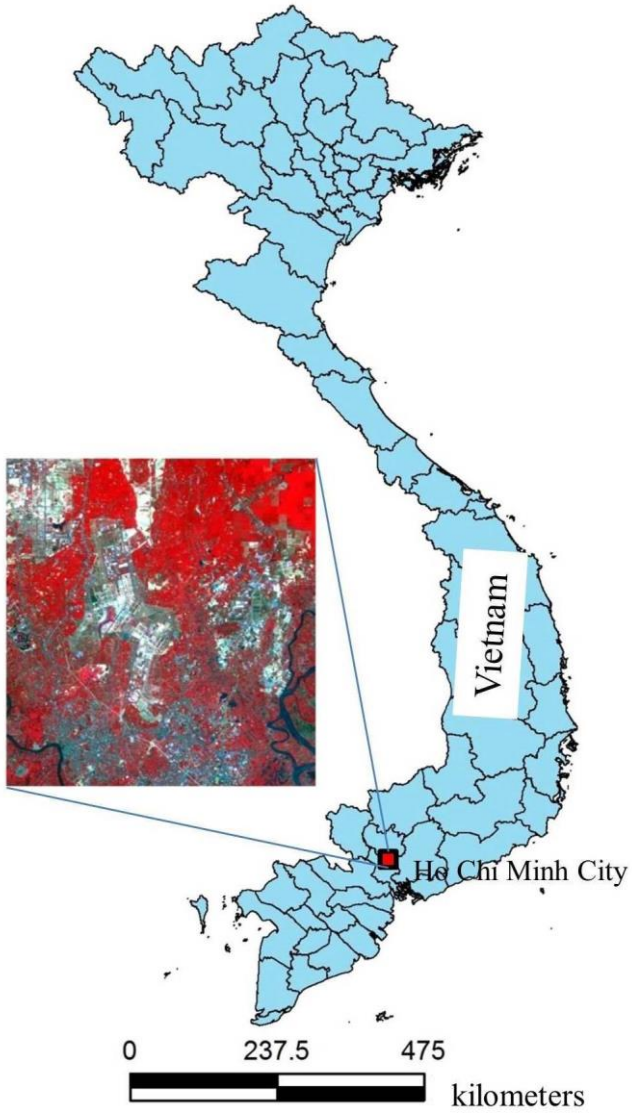

Figure 5.1 Study area.

Table 5.1 Data used.

Acquisition date	Sensor	Processing level
April 1, 2007	PALSAR	1.1
April 12, 2011		
March 31, May 2, 2007	Landsat	L1T
March 8 and April 11, 2011		
March 5, 2007	AVNIR 2	1B
March 16, 2011		

date as PALSAR images were considered. Table 5.1 shows the detail of all images used in this study.

Since all the images used in this study were acquired at nearly the same time of year (April), all the changes due to agricultural practices were ignored. Additionally, the different intensity of precipitation may cause the various levels of vegetation growth even in the same season of the year, thus the years (2007 and 2011) with normal precipitation records were selected for the study. Thus, all the phenological changes were also ignored and focused solely on the change due to the human intervention. The results were evaluated based on Advanced Visible and Near Infrared Radiometer type-2 (AVNIR-2) optical data acquired nearly the same time with PALSAR images and very high-resolution images in Google Earth.

5.3 Statistical analysis

Several indicators are possible to develop from optical images such as enhance vegetation index (EVI), soil adjusted vegetation index (SAVI), normalized vegetation index (NDVI), revised NDVI [68]. NDVI is one of the most common and well accepted indicator for the surface dynamics study using optical imagery and that has complementary information with SAR backscatter for surface phenomenon. One of

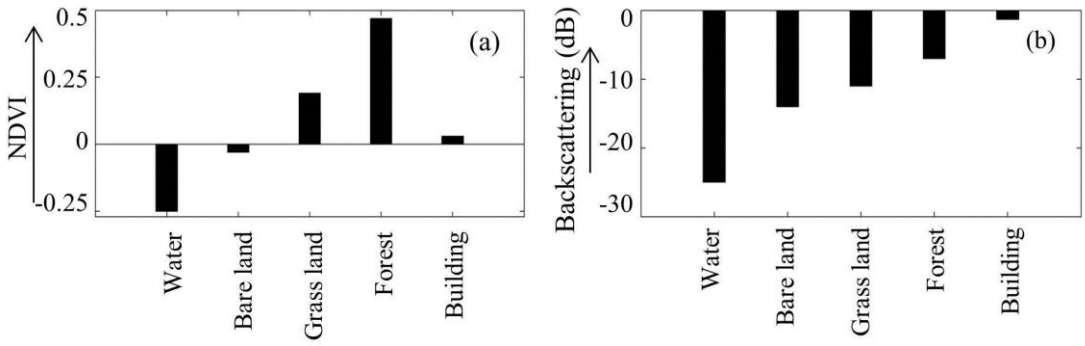

Figure 5.2 NDVI and SAR backscattering coefficient for major land use classes, (a) NDVI, (b) backscattering coefficient.

such information is changes in surface greenness without altering in the backscatter significantly e.g. pastureland, therefore NDVI is considered in this study.

Fig. 5.2 (a) represents the NDVI for major five features in the Earth's surface, and Fig. 5.2 (b) represents the backscattering coefficients of HH polarimetric component for the same features. The backscattering coefficients and NDVI value of each feature were obtained by taking the average value of the sample obtained manually from the known area. In each feature type, the sample pixels were more than 1000, and assumed that this signature was site independent.

While generalizing these five features, we considered grassland, forest and agricultural land (with crop plantation) as a vegetation area and identified the

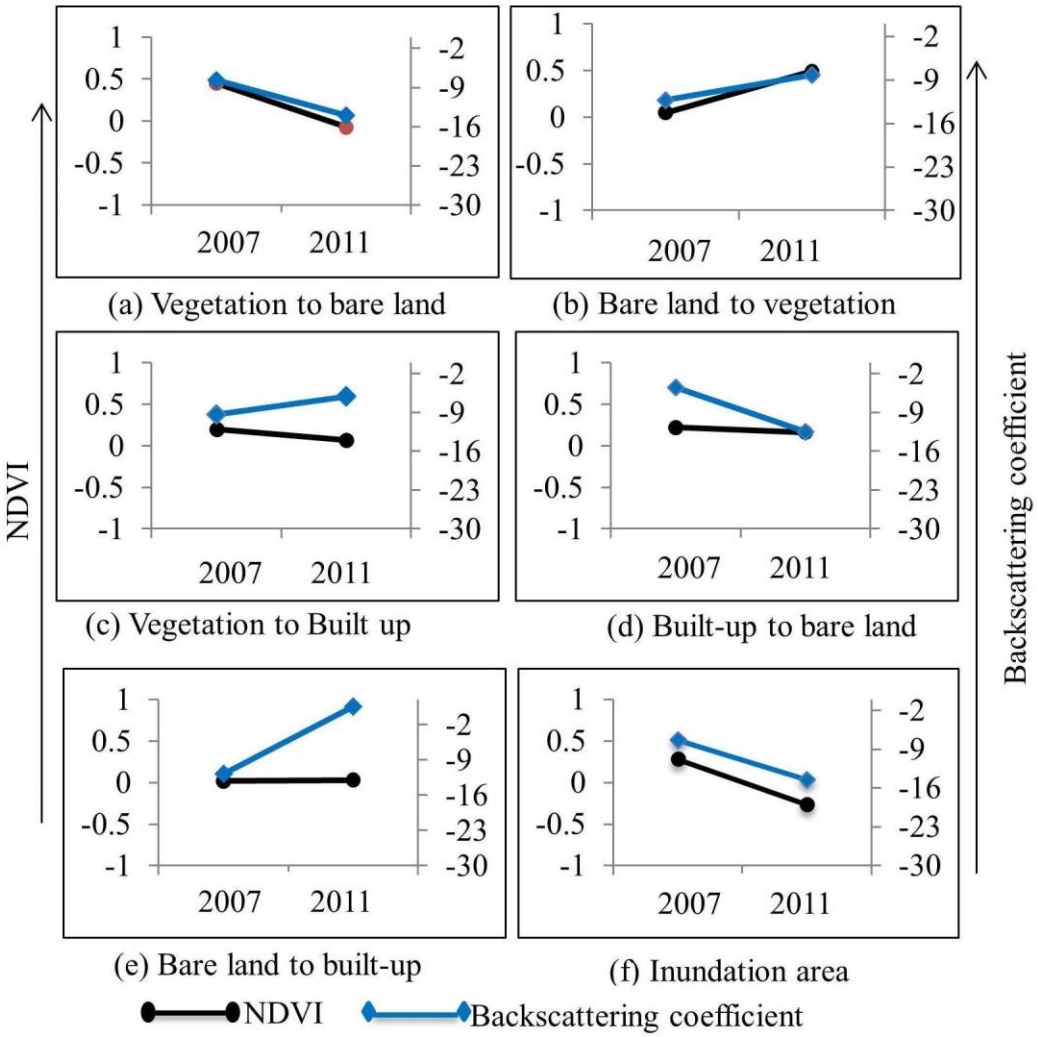

Figure 5.3 The backscattering coefficient and NDVI in pre and post image with several land cover change classes.

following possible change types. Inundation (vegetation, built-up or bare land to water bodies) and vice versa (water body to vegetation, built-up or bare land), bare land to vegetation and vice versa, bare-land to built-up and vice versa, vegetation to built-up and vice versa. A statistical analysis has been done for NDVI and SAR backscattering responses in earlier and later imagery for the above mentioned possible change types and presented in Fig. 5.3.

Fig. 5.3 shows that some change types are equally sensitive to the SAR and optical sensors e.g. vegetation to bare-land and vice versa, some have reverse effect such as: vegetation to built-up and vice versa and some are sensitive to one sensor whereas not in another, such as building construction in a bare land or building to bare land change. Similarly, some greenery appears in grassland or pastureland is not sensitive in some SAR sensor with relatively longer wavelength. Therefore, the complementary information available in multi-sensor images pave the way for further analysis.

5.4 Method

The process flow diagram for the optical and SAR image fusion for change detection and automatic labeling is presented in Fig. 5.4. Details of the methodology are presented in the following sections.

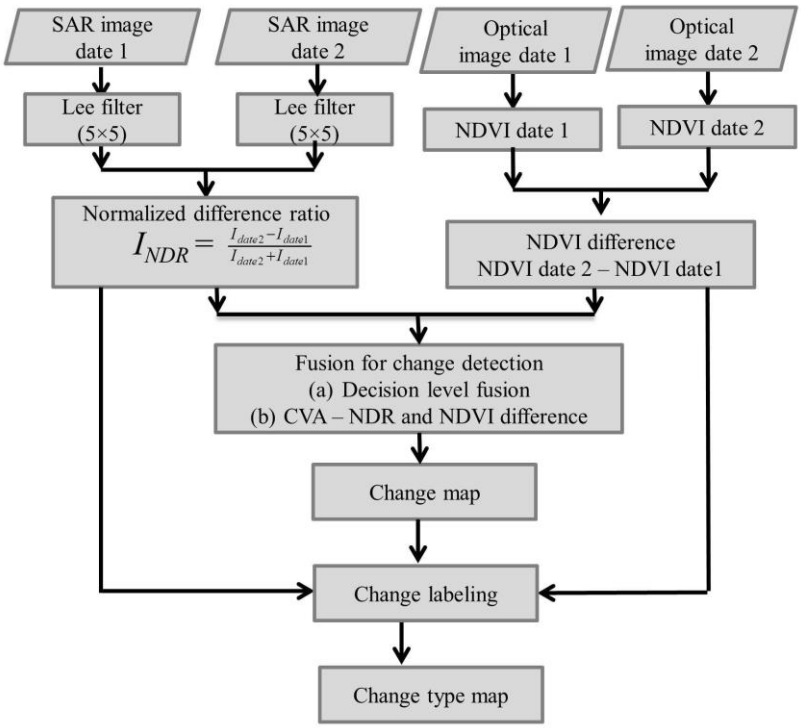

Figure 5.4 Process flow diagrams.

5.4.1 Preprocessing

5.4.1.1 Calibration and gap filling for Landsat data and gap filling

We used the Landsat L1T image. Atmospheric correction was done using ENVI 5.0 in which the raw digital number (DN) values were converted into surface reflectance. The calibrated images were then subjected for filling gaps [69]. The image acquired in March 31, 2007 and April 11, 2011 were the main considered image and dated on May 2, 2007 was used for filling gaps in March 31, 2007 and image acquired on March 8, 2011 was used to fill the gap in the image acquired in April 11, 2011.

5.4.1.2. PALSAR images - geometric correction and co-registration

All images were geometrically corrected using 30 m Global Digital Elevation Model (GDEM) using ASF MapReady 3.2. The images were geo-coded with UTM system and co-registered with Landsat imageries with 19 ground control points selected manually in ENVI 5.0, where the overall error was less than a single pixel. The nearest neighbors resampling was used at this stage.

5.4.2. Deriving the change image

5.4.2.1. Normalized difference ratio from SAR images

A normalized form of ratio, Normalized Difference Ratio (NDR), operator is used to generate the change image from multi-temporal SAR images. The NDR operator generates pixel value from -1 to +1. All no-change pixels are clustered around 0, while all the change pixels are deviated far from 0. Change image generated by the NDR operator can be seen in Fig. 5.9 (d). The NDR operator is defined as [14].

$$NDR(t_1, t_2) = \frac{A_{t_2} - A_{t_1}}{A_{t_2} + A_{t_1}} \quad (5.1)$$

where, $A_{t1}$and A_{t2} are amplitudes of co-registered images acquired on two dates t_1 and t_2.

5.4.2.2. NDVI difference (ΔNDVI) image

The NDVI gives the vegetation greenness thus it is very useful to study the surface dynamics. NDVI at time t for Landsat TM/ETM+ is defined as Eq. (5.2).

$$NDVI(I) = \frac{\rho_{4,t} - \rho_{3,t}}{\rho_{4,t} + \rho_{3,t}} \quad (5.2)$$

Where ρ_2 and ρ_4 are reflectance of TM/ETM+ band 3 and 4 respectively. The difference of *NDVI*, *ΔNDI* is derived by Eq. (5.3):

$$\Delta NDVI = NDVI(t_2) - NDVI(t_1) \quad (5.3)$$

5.4.3. Fusion of NDR and (Δ *NDVI*) for change detection

As discussed in section 3 some changes are sensitive to both sensors however, others are sensitive in only one. Therefore, they have some complimentary information, which are important for full dimensional change detection. We devise two different data fusion techniques in order to make use of complimentary information that can capture all changes.

5.4.3.1. Decision level fusion

Decision level fusion is common for multi-sensor image fusion, specifically in SAR and optical imagery and motivated from classification. In this study, we have developed a change map through thresholding of both change images independently, namely NDR image, that was derived from two multi-temporal SAR amplitude images from eq. (5.1), and Δ NDVI image, derived from two multi-temporal NDVI image generated from the equation (5.2). Union of the detected changed area was carried out to get the final change map. The fig. 5.5. (a) represents the procedure for the change detection process using decision level fusion.

5.4.3.2. Change vector analysis (CVA)

Change vector analysis is a well-established change detection method for multi-spectral images [7],[8];. Even though the CVA is well-accepted methodology for multi-spectral images, it is new for optical and SAR integration.

For all land cover/use status, we assume that the quantity of land cover/use status in optical and SAR response, *f*, can be expressed as follows:

$$f = f(N, B) \quad (5.4)$$

Where *N* denotes NDVI obtained from optical sensor and *B* denotes backscatter from SAR, respectively. When we take a partial derivative of Eq. (5.4) with respect to t, Eq. (5.5) is derived:

$$\frac{df}{dt} = \frac{df}{dN}.\frac{dN}{dt} + \frac{df}{dB}.\frac{dB}{dt} \quad (5.5)$$

Assuming *N* and *B* are independent to each other, amplitude of the change, *A* can be written as:

$$A = \left|\frac{df}{dt}\right| = \sqrt{\left(\frac{df}{dN}.\frac{dN}{dt}\right)^2 + \left(\frac{df}{dB}.\frac{dB}{dt}\right)^2} \quad (5.6)$$

Now, we assume *f* as a simple linear function in Eq. (5.7)

$$f = a_1 N + a_2 B + a_3 \quad (5.7)$$

Eq. (5.6) can be rewritten as Eq. 5.8:

$$A \approx \sqrt{a_1^2\left(\frac{\Delta N}{\Delta t}\right)^2 + a_2^2\left(\frac{\Delta B}{\Delta t}\right)^2} \quad (5.8)$$

From the histogram presented in Fig. 5.5, it is clear that all the pixels in both NDR and NDVI differences are concentrated around 0. Mathematically, all the pixels in NDR images are within -1 to 1, but all the pixels in the NDVI difference image is also appeared in the same range in an experiment. This is because, even though the possible range of NDVI is -1 to 1, the changes of NDVI from one end to another end

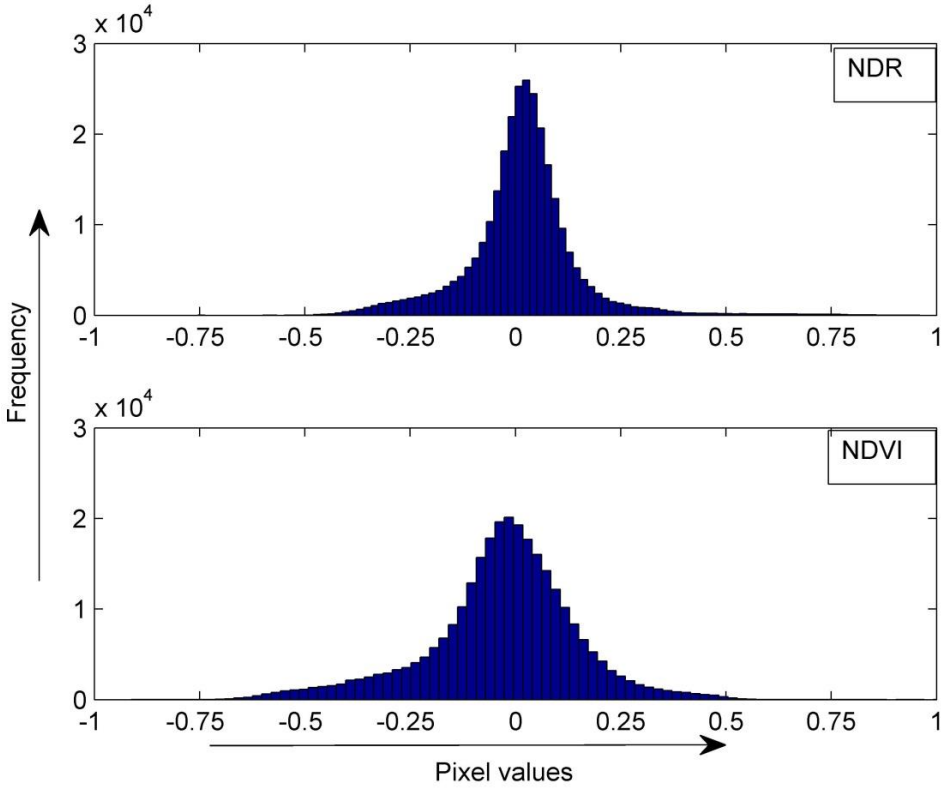

Figure 5.5 Histogram of NDR and NDVI difference imge, in both majority of pixels are concentrated around 0.

is unlike to happen and thus almost all pixels fall in between-1 and 1. Therefore, we can assume that that $|a_1|=|a_2|$, and Eq.(5.9) is derived:

$$A \approx \sqrt{a_1^2\left(\frac{\Delta N}{\Delta t}\right)^2 + a_2^2\left(\frac{\Delta B}{\Delta t}\right)^2} \approx \sqrt{\Delta N^2 + \Delta B^2} \quad (5.9)$$

Now, $\Delta N = NDVI(t_2) - NDVI(t_1) = \Delta NDVI$ and we assume $\Delta B = B(t_2) - B(t_1) \approx NDR(t_1,t_2)$, expressed by Eq. (5.1). Then Eq. (5.9) can be rewritten in the form of $\Delta NDVI$ and NDR as follows:

$$A = \sqrt{\Delta NDVI^2 + NDR^2} \quad (5.10)$$

Eq. (5.10) represents a change magnitude from both optical and SAR images. A threshold value in this image was identified by manual trial and error procedure that can segment change and no-change area. The overall procedure is presented in Fig. 5.5 (b)

5.4.4. Automatic change labeling

In order to detect the change area in NDR image or in Δ NDVI image, two threshold values are necessary. These threshold values segmented the change image into three classes, namely: increase-backscattering area, decrease backscattering area and no-change in case of SAR images, and increase, decrease and no change in NDVI for Δ NDVI. While combining these two change images with associated threshold values; we can have 9 zones as shown in Fig. 5.6. All of these nine zones represent a unique change type, thus, a relationship between Δ NDVI and NDR is possible to

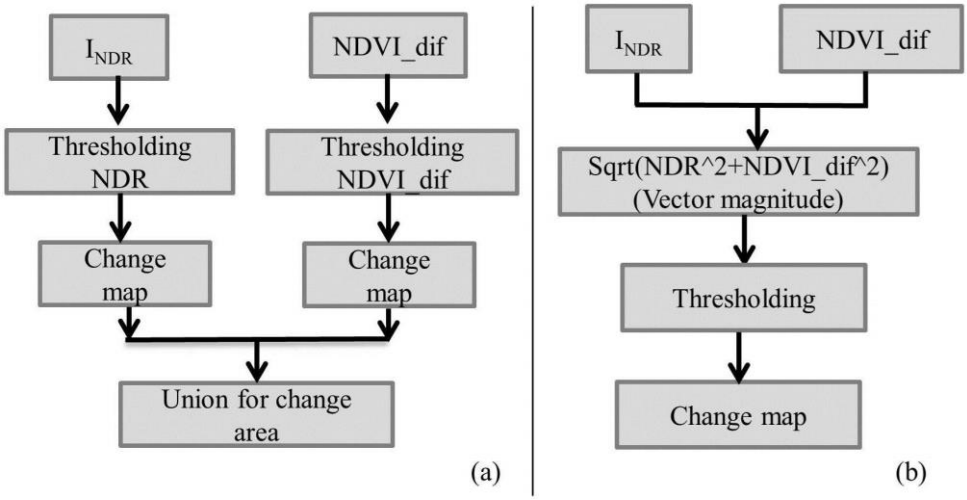

Figure 5.6 . SAR and optical information fusion procedure, (a) Decision level fusion and (b) CVA based fusion.

develop that allows us to detect the multi-class change automatically.

Based on the responses of different change features in SAR and optical sensor presented in Fig. 5.3 and the scatter diagram in Fig. 5.7, a relationship between NDR and Δ NDVI was developed and their associated location in Δ NDVI vs. NDR plane was also identified empirically. The developed relationship, their associated position in the Δ NDVI vs. NDR plane along with the possible change type and available example are presented in Table 5.2. As the NDVI and the backscattering intensity for all major land cover features are known and assumed to be stable and independent to the locations, the developed relationship is believed to be valid all over the World.

5.4.5. Accuracy assessment

The effectiveness of the proposed fusion method was evaluated with visual analysis, and quantitative capability. A visual comparison of the change image generated from individual sensors and proposed fusion techniques and corresponding change map was done for the selected change sites, this gave the overall idea of the effectiveness of the generated change images. In addition to that, the change detection map obtained from proposed methodology was evaluated with the change map obtained from the high-resolution AVNIR images and very high-resolution images from Google Earth interactively in selected areas.

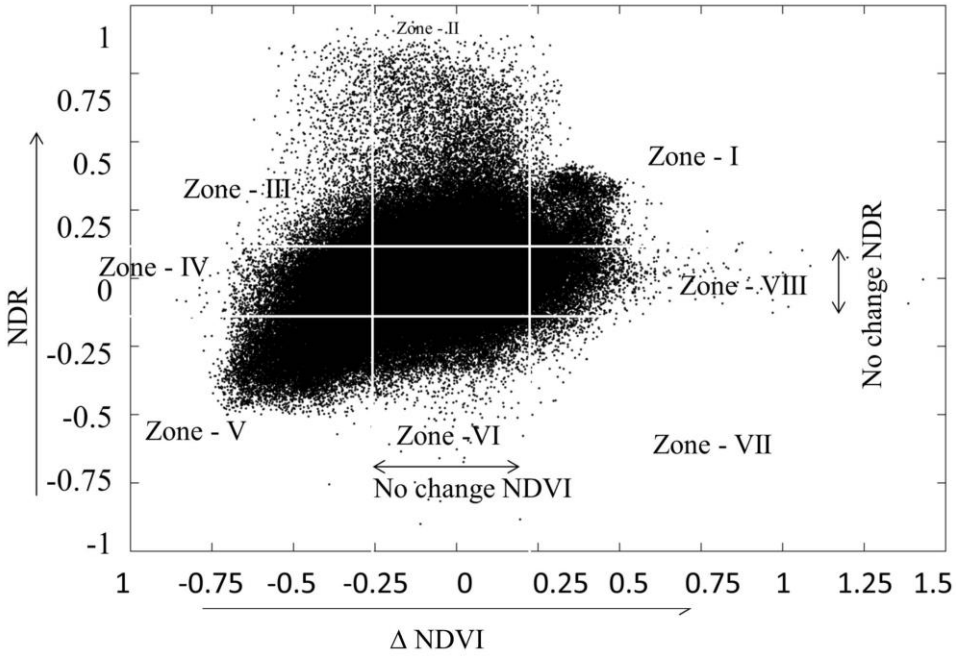

Figure 5.7 Scatter diagram, Δ NDVI vs. NDR.

In order to evaluate the results quantitatively, confusion matrix was used. This allocates the change and no change class and its expected value is derived using those in a corresponding so-called a ground reference data set. The confusion matrix allows to derive numerous summary measures of the accuracy of the allocated classes and amount of change that has occurred. The considered accuracy measures are user`s accuracy, producer`s accuracy, error of omission, error of commission, overall accuracy and kappa index [57].

5.5. Results and discussion

5.5.1 Change detection

The change map was generated through the proposed fusion techniques. The obtained results were compared with the results obtained from Δ NDVI, NDR and widely used multi-spectral change vector analysis (CVA) for Landsat imagery [7],[8]. Threshold values for each of the input change images was obtained with MTEP and implemented in an ENVI 5.0 that segmented the changed area from no-change area.

For the visual analysis, a false color composite of Landsat imagery was used. Fig. 5.8 represents the false color composite of Landsat imageries in (a) 2007 and (b) 2011 and (c) and (d) are the interested zoom-in sites corresponding to the images

Table 5.2 Relationship between NDR and NDVI difference with land use/cover change type, and associated zones in ΔNDVI VS. NDR plane.

Observation		**Zone**	**Change type**	**Example**
NDR	Δ NDVI			
Increase	Increase	I	Bare land to vegetation	Bare land to forest, or pasture land or agriculture etc.
Increase	No change	II	Bare land to build-up	Bare land to building
Increase	Decrease	III	Vegetation to built-up	Pastureland, agriculture or forest to built-up.
No change	Increase	VIII	Increased greenness	Pastureland getting seasonal greenery
No change	No change	Center	No - change	No-Change
No change	Decrease	IV	Decreased greenness	Pastureland getting dry
Decrease	Decrease	V	Vegetation to bare land	Deforestation, crop harvesting, inundation
Decrease	No change	VI	Built-up to bare land	Building collapse
Decrease	Increase	VII	Built-up to vegetation	Building to forest, or other vegetation, agriculture land etc.

acquired on 2007 and 2011 respectively. These figures and interested zoom-in sites were considered as a ground truth and the results obtained from each input change image were compared with a simple visual inspection.

Fig. 5.9 illustrates the change image, corresponding change map and zoom-in change map with interested sites corresponding to the interested sites in Fig. 5.8 for all input datasets. Fig. 5.9 (a) –(c) represents the change vector magnitude (CVM) from Tasseled cap transformation of Landsat-7 ETM+, corresponding change map and zoom-in map of the interested areas, similarly Fig. 5.9 (d) – (f) are for the NDVI, Fig.5.9 (g) – (i) are for the NDR, Fig.5.9 (j) – (l) for proposed CVM generated from △NDVI and NDR and Fig.5.9 (m) – (n) are for the union of change map obtained from △NDVI and NDR.

While comparing the grayscale change image in Fig. 5.9 (a), (d), (g) and (j), some images are better than others, even though all of them are in the same spatial resolution. NDVI difference (Fig. 5.9 (d)) and NDR (Fig.5.9 (g)) appear to be smoother than other two, however, NDR images are not as smooth to NDVI difference. In these images, bright and dark colors represent the change areas, whereas the moderately gray area is for no-change. Regarding the change images obtained from the CVM using Tasseled cap transformation (Fig. 5.9 (a)) and CVM uses △NDVI and NDR (Fig. 5.9 (j)), both appear to be more contrast between change and no-change area. In these images, the bright color represents the change area and dark color represents no-change area.

As far as the change map results and their corresponding zoom-in areas are concerned, the change map obtained only from optical or SAR imageries have several errors of commission and omission. For example, using only optical imageries (Fig 5.9 (b), (c)) site (ii) has a big error of omission and the site (iv) has a big error of commission. However, while considering the NDR image (Fig 5.9 (e), (f)) site (iv) all are missing and almost all detected areas are not even close to the actual shape in the field. Similarly, while comparing the results obtained by integrating the results from NDR and △NDVI, in Fig. 5.9 (m), (n) the omission error is reduced significantly, however the commission error is huge i.e. because the union operation resulting the consideration of all commission error from both sensors. In contrast to that, the NDR and NDVI integration using CVA approach is better. See in site (iv) the

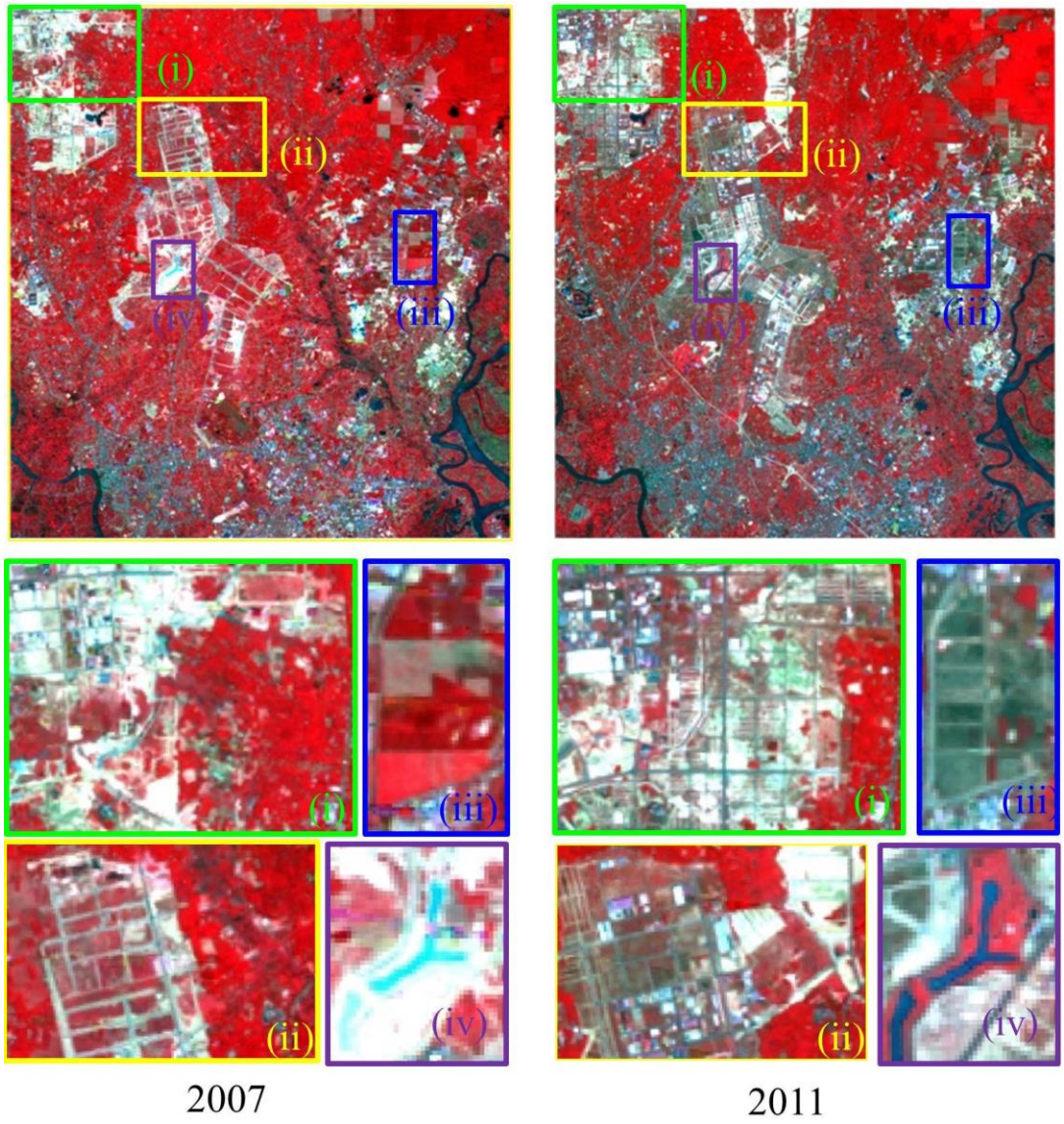

Figure 5.8 Study area false color combination 2007 and 2011, (i) site 1, (ii) site-2, (iii) site 3 and (iv) site 4.

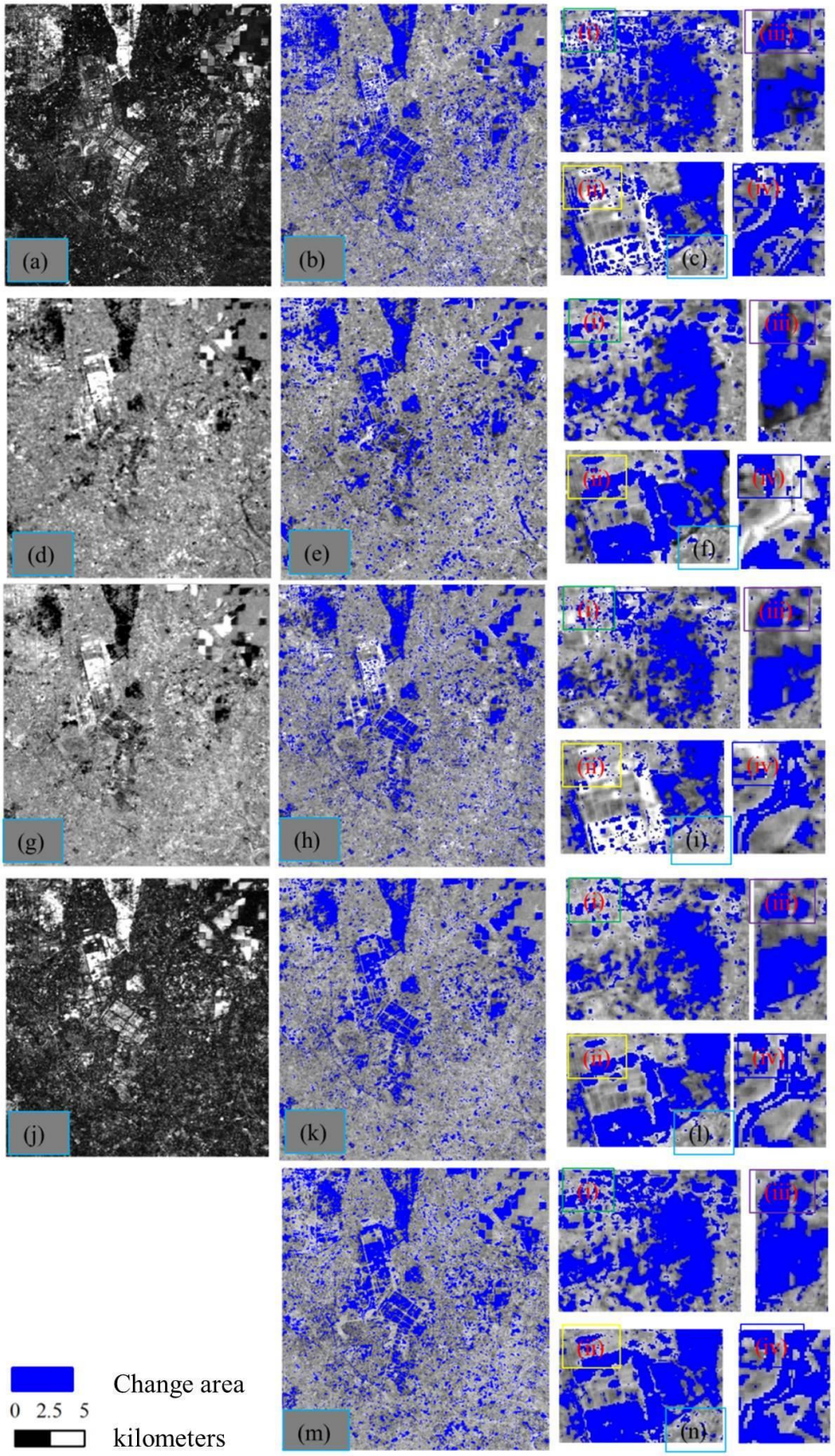

Figure 5.9 Change map obtained from different input datasets and corresponding zoom-in map for selected sites, (a) - (c) CVA with Tesselled cap transformation, (d) - (f) NDR, (g) – (h) NDVI difference, (j) – (l) CVA – NDVI difference and NDR, and (m) – (n) union of NDR and NDVI difference.

overestimation seen in a water body while using optical imagery was reduced and the site (ii) is also reasonably better in comparison to NDR and optical imagery. The commission error in SAR is reduced in site (ii) and omission error site (iv).

Table 5.3 summarizes the accuracy assessment done in this study. The Kappa index is improved by 0.16 and 0.17 while using the proposed CVA based fusion approach in comparison to the NDR image, and NDVI difference respectively. It is improved by 0.13 while comparing the CVA in Landsat imageries with significant decrements in false and missing alarm.

In general, the SAR image can detect almost all kinds of changes except the small changes that do not make much difference in the surface roughness, e.g. small vegetation; however, the performance improvement is significant. This is because the results obtained from the SAR image have lack of clear boundary line in most of the detected sites. This limitation can easily be overcome by using SAR and optical image fusion operation. In addition to that, several changes related to urban extensions are not sensitive to greenness and brightness for example bare land to built-up area and some vegetation changes such as forest to bush or grassland could not be detected properly in optical images. Similarly, some water body with different level of turbidity is also appearing as changed in the Tasseled cap transformation. As a result, the false change appears in the generated change map. Additionally, building structure in bare land that does not alter the greenness, wetness and brightness significantly is not possible to detect. All of these errors of commissions and omissions can be reduced considerably while implementing the CVA technique with NDR and NDVI differences.

5.5.2. Automatic multi-class change labeling

The change map developed through the CVA based SAR and optical information fusion approach was subjected to multi-class change labeling. The results obtained from the relationship presented in Table 5.2 suggested that the increase or

Table 5.3. Change detection accuracy assessments for several approaches.

Input data set	NDVI difference	NDR	CVA - Tesselled cap transformation	Union - NDVI and NDR	CVA - NDVI, NDR
Over all accuracy	88.23	89.13	90.36	85.69	94.7
Kappa	0.73	0.74	0.75	0.69	0.88

decrease in NDVI without altering NDR is very rare. Those changes, which do not alter the surface roughness significantly, such as bare land to pasture land or grassland and vice versa, which are characterized as increased or decreased vegetation are shown in Fig. 5.10; this includes the boundary line of the change areas, mainly due to the changes in vegetation. Here, two examples are presented, (i) site 1, that is decrease in NDVI – smoothing of some agricultural area that is associated with decrease in vegetation area (Zone VIII in Fig. 5.7) and (ii) increase NDVI area, growth of small vegetation/greenness, that is associated with increase vegetation area (Zone IV as in Fig. 5.7). Thus, these zones were merged with associated zones i.e. (Zone VIII to Zone I and Zone IV to Zone V as in Fig. 5.7).Now we have six change classes and one no-change class as with the generalized relationship presented in Table 5.4.

In order to compare the results of the proposed change labeling approach with optical and SAR information, an automatic labeling with optical imageries using

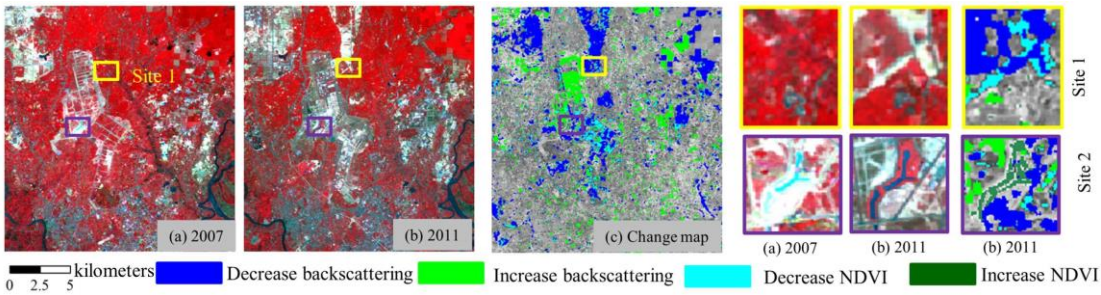

Figure 5.10 Change area with no-change in NDR, (a) reference image in 2007, (b) reference image in 2011 and (c) change map with no-change in NDR and interested zoom-in sites.

Table 5.4. Generalized relationship between NDR and NDVI difference with land use/cover change type.

Class	**Response**		**Change types**
	NDR	NDVI	
Class 1	Increase	Increase	Increase vegetation
	No change	Increase	
Class 2	Increase	No change	Bare land to built-up
Class 3	Increase	Decrease	Vegetation to built-up
Class 4	No change	Decrease	Vegetation to bare land
	Decrease	Decrease	
Class 5	Decrease	No change	Built-up to bare land
Class 6	Decrease	Increase	Built-up to vegetation

Tasseled cap transformation – brightness and greenness index [7],[8] was implemented. The Fig. 5.11 (a) is the change labeling map using the proposed optical and SAR information fusion and Fig. 5.11 (b) is the change labeling map obtained using the optical imagery only. While interpreting the resulted map visually, all the areas classified as class 2, class 3 and class 4 (vegetation or bare land to built-up and decrease a vegetation area according to the relationship in Table 4) were classified in a single class 3 (decrease NDVI and increase brightness) in the optical imagery based on the brightness and greenness index obtained from the tasseled cap transformation in Landsat 7 images. These are the major change classes in the urban extension; therefore, the change labeling using the optical information in an urban information is suffering from a poor performance. Such misclassification obtained while implementing the brightness and greenness index is due to the lack of enough information in considered index. These indexes are highly correlated negatively (-0.8). i.e. decrease in the greenness increases the brightness. On the other hand, the NDR and NDVI differences are linearly independent (0.33), thus, they can have more

Regarding the other combinations of optical imageries' derived indices such as brightness vs. wetness or greenness vs. wetness, all are linearly dependent to each other and they have a very good positive or negative correlation coefficient. Add to all, only the optical imagery does not provide enough information for discriminating

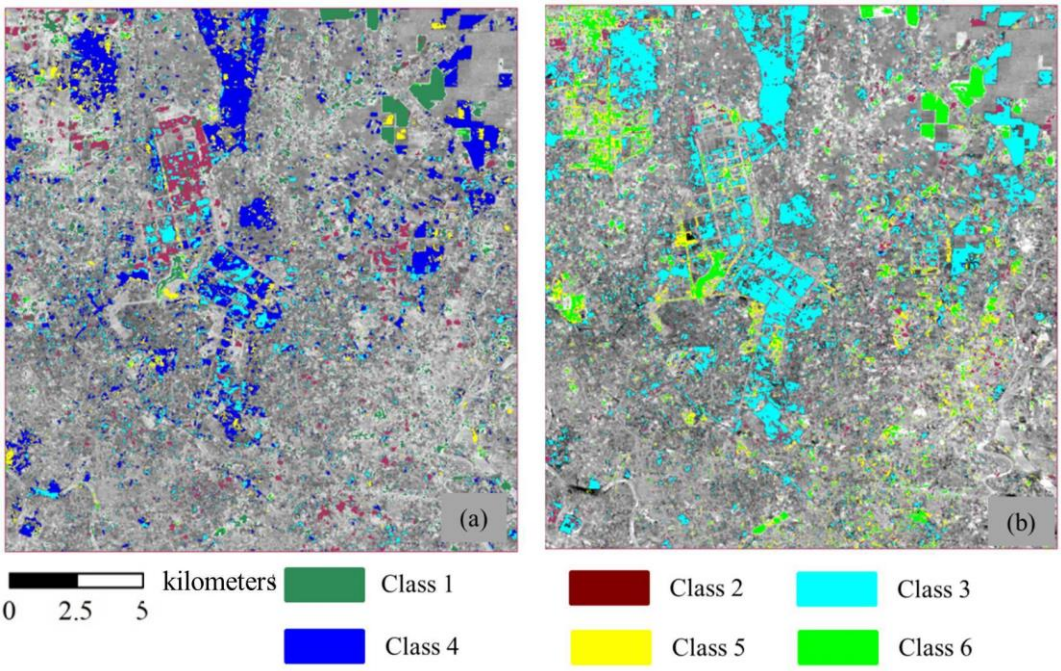

Figure 5.11 Change map with change type labeling, (a) CVA with NDR and NDVI difference, (b) CVA with brightness and greenness obtained from Tesselled cap transformation in Landsat images.

several classes automatically. Thus, a quantitative accuracy assessment is not done for the automatic change type labeling using optical imageries. Table 5.5 illustrates the accuracy assessment of the change labeling using NDR and NDVI difference. The obtained overall accuracy is 87.97% and the Kappa index is 0.78.

Of course, results obtained from optical imagery's are better in several aspects, like shape delineation or tracking vegetation dynamics and many others, however, several changes, including bare land to urban extension or forest to agricultural or bushes or pastureland changes are not detected properly. In contrast to

Table 5.5. Confusion matrix for automatic change labeling in CVA - NDR and NDVI difference.

	Zone I and VIII	**Zone II**	**Zone III**	**Zone IV or V**	**Zone VI**	**NO-change**	**Total**	**Producers' accuracy (%)**	**Error of omission (%)**
Zone I or VIII	**1385.00**	34.00	0.00	0.00	0.00	262.00	1681.00	82.39	17.61
Zone II	38.00	**417.00**	21.00	8.00	0.00	0.00	484.00	86.16	13.84
Zone III	0.00	31.00	**251.00**	24.00	0.00	53.00	359.00	69.92	30.08
Zone IV or V	0.00	96.00	76.00	**1325.00**	49.00	193.00	1739.00	76.19	23.81
Zone VI	0.00	0.00	0.00	67.00	**123.00**	0.00	190.00	64.74	35.26
No-change	171.00	78.00	76.00	111.00	49.00	**7008.00**	7493.00	93.53	6.47
Total	1594.00	656.00	424.00	1535.00	221.00	7516.00	11946.00	**Over all accuracy = 87.97**	
User's accuracy(%)	86.89	63.57	59.20	86.32	55.66	93.24			
Error of commission (%)	13.11	36.43	40.80	13.68	44.34	6.76		**Kappa index = 0.78**	

that SAR image derived index NDR is very good to locate such changes. Yes, SAR images are not good at delineating the proper shape of the changed objects and do not detect these objects, which do not alter the surface roughness significantly, such as bare land to pastureland or grassland. Therefore, the combined use of the SAR and optical images would be very effective to detect the change area and its potential is presented in section 5.5.1. In addition to that, as mentioned in the previous section, the responses of SAR and optical sensor from the change in ground feature, is known and stable. Their relationship is also very powerful in order to track the change type automatically and received a very good accuracy as presented in this section.

5.6. Conclusions

With the availability of multi-sensor data, a multi-sources data processing and analysis technique is required to capture all changes. In a very complex urban sprawl area, an automatic multi-class change detection with an empirical relationship between the response of surface feature to optical and SAR imagery has shown to be effective. Similarly, the CVA technique for information fusion also proved its capability of fulfilling their requirement for change detection. Given a huge potential of multi-source data, continue expansion of the quantity of diverse sensor types of remote sensing data, CVA might provide a capability of fusion of increasing demand of multi-source information for full-fledged change detection and a relationship among the responses of the Earth surface feature's to these sensors would provide a broader-dimension of change type detection. By further analyzing the response of each change feature to optical and SAR imagery or using ancillary dataset, this method can be further extended for disaster monitoring, crop monitoring, etc. In addition to that, an automatic adaptive thresholding would enhance the results by protecting from the human biases and error and make the system fully automatic.

6 SYNOPSIS

This chapter highlight by chapter progress achieved, and their practical implications, and finally outlook for possible extension.

6.1 Introduction

Migration from rural to urban area is increasing every year. Thus, urbanization is in the highest increasing rate ever experienced in the word and it is likely to increase in the coming years. Development associated with urbanization not only decrease the proportion of agricultural land, forest, open space and other land cover types but also affects the local as well as global environments. Because of its essence in several applications including land policy development, site selection, demographic and environmental issues at national, regional or global scale as well as in promoting better decision-making, information on land use/cover and their changing patterns is always an important topic.

Accurate and up-to-date information of the land cover and use pattern in cost effective manner is interest of all. Collecting the changed information from the ground-based survey would always better than any other options in terms of accuracy. However, it is impractical to do a ground based change mapping regularly in a short interval in rapidly growing urban areas. The remote sensing is the best available technique to update such changes [3][3][3][3]timely and cost effectively. Therefore, land cover and use change detection using a satellite based remote sensing is a promising research topic for several thematic areas including , land cover/use dynamics, disaster assessment, urban monitoring, infrastructure planning and development, environmental monitoring etc.

Accordingly, this research focuses on timely and accurate urban change mapping approach through the use of polarimetric images acquired in different modes and integration of optical and SAR images. Following the explanation, the following specific research objective were defined: (i) to devise a simple technique to detect a temporal changes using single polarization SAR imagery (Chapter 3), (ii) to identify the most sensitive polarimetric descriptors for various change detection, and fusion of pair of polarimetric descriptors to detect the full-fledge change detection (Chapter 4) and (iii) to develop an information fusion framework to enhance the change detection performance and automatic change pattern tracking (chapter 5).

6.2 Achieved results

6.2.1 Better change image generation from multi-temporal SAR images

Generating change image from multi-temporal SAR images is a very first step towards detecting a change. Analysis on SAR image becomes extremely complex due to the presence of multiplicative nature of speckle noise. While generating a change image from multitemporal SAR images using difference operator, the noise in the developed image will propagate significantly from the two source images, and thus, to reduce the effective noise in the resulted change image, ratio image was recommended and already accepted in the community because it minimize such noise notably but that is not still perfect. In this research, we devise a new change image generation operator named normalized difference ratio operator (NDR), that can give the change image with less noise than widely accepted ratio operator.

6.2.2 Threshold determination approach

The thresholding is the most common approach to segment the change area from no-change background. Most of the change detection algorithms are intended for bi-level thresholding. The histogram of the image is assumed to have one valley between two peaks. The peaks represent the background and objects respectively. A thresholding value is usually identified by assuming the same distribution in change and no-change area in such cases. Assumption of a specific distribution in no-change area would be reasonable; however, it is pretty unpredictable for change-area, that that could be erroneous while finding the threshold value. Therefore, in order to address this issue we devise a thresholding algorithm by assuming a Gaussian distribution in no-change area only while implementing with the change image generated by the proposed NDR operator.

6.2.3 Coupling of thresholding and region growing algorithm

Pixel wise change detection methodologies that are based on the threshold value(s) only use the backscatter information of the pixel. It simply ignores the spatial context and it is almost impossible to segment change and no-change areas with a specific threshold value perfectly. However, thus far, spatial information is common only in the high resolution (HR) or very high-resolution (VHR) images. Although it is gaining popularity in image segmentation and change detection for HR and VHR, such methods are not applicable in the medium to low-resolution SAR images.

Therefore, in this study, we make use of spatial information through the coupling of thresholding and region growing algorithm in the low-resolution SAR images. The developed methodology was tested with simulated and real SAR images associated to the geographical locations and achieved a very good performance.

6.2.4 Identifying the best polarimetric descriptor for different change feature

The availability of several processing techniques and the possibility of generating several polarimetric descriptors from fully PolSAR images have created a good opportunity to conduct a sensitivity study to find the most effective descriptors for detecting different types of changes. Thus, in this study a sensitivity analysis has been carried out for twelve most common polarimetric descriptors and found the best descriptors for the different types of the changes. In addition to that, the best pairs of complementary components have been identified so that a full-fledge change detection is possible through the PolSAR images.

6.2.5 Information fusion of polarimetric descriptor

As number of polarimetric descriptors are possible to generate through the several processing techniques from PolSAR images, different polarimetric descriptors are sensitive to the different types of the land cover/use changes. Some of them have complementary information and can detect all types of changes if they can use together. In order to include the full-fledge change in an urban environment pairs of complementary couple of polarimetric descriptors are necessary to use. Accordingly, in this study, a fusion approach for the pairs of polarimetric descriptors has been proposed and implemented successfully for change mapping.

6.2.6 SAR and optical information fusion framework for change detection

With the analysis of multi-temporal SAR and PolSAR imagery, we concluded that, SAR signals are good to detect various types of changes that are sensitive to the backscatter. However, some changes are not sensitive to all SAR frequencies and most importantly; the proper shape delineation is difficult due to the presence of speckle noise. Therefore, SAR and optical information fusion are inevitable for the best result. Several SAR and optical information fusion approaches are also available in the literature; however, they mainly focused on the pan sharpening or some specific purpose than the change detection. If available for change detection, they mainly focused on some specific land cover or used pattern, not for the generic types that can

address the urban area of extremely complex land use/cover pattern. Thus, a SAR and optical information fusion approach is proposed and implemented in this study that gives a very good result compare to the results obtained from single sensor..

6.2.7 Framework for automatic change pattern detection

Automatic change pattern detection is not only very important in an urban environment but also extremely challenging. Some change pattern detection approach using MSI images is available in the literature. They are based on change vector analysis on different indicators generated from MSI but their discriminated classes are very limited due to the lack of enough information. In this study, thus, we implemented the unique and independent information acquired by the SAR and optical sensors to develop a relationship. It is known that the unique signature of SAR and optical images for each land use/cover feature is stable and site independent, in the similar weather and light condition for optical imagery and same acquisition configuration in case of SAR images, the developed relationship is independent to the location. The developed relationship was deployed successfully in the outskirts part of the Ho Chi Minh City that successfully delineates six change patterns in an urban environments.

6.3 Practical implications of the achieved results

The methods developed and tested in this study help in producing a better change map and monitoring of the change in urban environments over time. A PALSAR images of different polarimetric mode and free imagery available from Landsat ETM plus have been utilized in this study. The work mainly focused on three types of dataset (a) single polarization SAR images, (b) fully PolSAR images and (c) a single polarization SAR image and Landsat ETM+. The best result is possible only with the combined use of SAR and optical images. Therefore, the appropriate approach can be applied upon the availability of the dataset. As all the proposed methods implemented successfully in urban environments, in a very complex land cover/use patterns, these methods can extend easily in several other thematic areas. The application may include but not limited to: agricultural monitoring, flood monitoring, snow and glacier monitoring, forest monitoring, and other environmental monitoring etc. It would be extremely useful for decision-makers for sustainable development and management of urban environments.

The change image generation is one of the most fundamental tasks while developing a change map. The proposed approach allows to generate a better change image that has the least amount of noise in comparison to the other approaches such as ratio, difference etc. As the fundamental processing gives better results than its influence will reflect to the overall processing, and thus enhance the change detection capacity. The thresholding and coupling of thresholding and region growing algorithms gives the better change map while using the multi-temporal SAR images.

The other part of the work has two achievements, they are (a) the best polarimetric descriptors to describe a particular change and their complementary couple and (b) fusion approach for such complementary couple of polarimetric descriptors. These two achievements along with the NDR operator, a better change map can be developed in an urban area, and have a good prospect to extend other environments as well.

A multi-sources data processing and analysis technique can capture all changes from multi-sensor data. The CVA technique for information fusion proved its capability of fulfilling this requirement for change detection. Given a huge potential of multi-source data, continue expansion of the quantity of diverse sensor types of remote sensing data, CVA might provide a capability of fusion of increasing demand of multi-source information for full-fledged change detection. In addition to that, in a very complex urban sprawl area, a change pattern detection with an empirical relationship between the response of the feature's to optical and SAR imagery has shown to be effective. The developed relationship among the responses of the earth's surface feature to these sensors would provide a broader-dimension of change pattern detection.

6.4 Relevance, utility and possible impact on large programs and organizations

The proposed methods are extremely useful to get an accurate estimation of the status of land cover/use change pattern. It can help to assess land use, land cover situation, and monitor it in regularly with more accurately and efficiently according to the availability of the data. The automatic pattern recognition approach is extremely useful to update the thematic map in a regular interval in a cost effective manner. Because of the simplicity and ease of the method, the methodology proposed can implement without having the expert knowledge in the field. Additionally, the

interpretation is also very straightforward due to the clarity in developed change pattern. Thus, this method is useful for monitoring of the most important indicators of the development by a city government locally or in a national level.

The techniques developed can contribute to address partly in the requirement of several public organizations such as United Nations Human Settlements Program (UN-Habitat) for the sustainable development, FAO land use and land cover information program and Intergovernmental Panel on Climate Change (IPCC).

6.5 Recommendations for future research

- In some cases an apparent change in the water body has been detected that may be the influence of several factors such as: the wind direction or different level of turbidity, a detailed analysis is required to identify the underlying reason of the apparent changes in the water body.
- The developed change approaches in this dissertation are the cases of urban area and thus, the methods are extendable for several other thematic areas such as agricultural monitoring, forest monitoring, seasonal vegetation monitoring, disaster monitoring etc. with a small change. Therefore, an extension of this method to other application would be a promising research.
- Though, the work has been focused on SAR intensity information, the phase information could be sensitive to some changes in which intensity is not. A detail analysis by using phase and intensity information is recommended.
- Several indicators are possible to develop from optical images such as enhance vegetation index (EVI), soil adjusted vegetation index (SAVI), snow index, brightness index, etc. and they may pose complementary information with SAR backscatter and/or NDVI therefore, a detailed analysis is recommended to identify the most efficient index which may improve the change pattern detection capability.
- Additionally, by using ancillary dataset, the automatic change pattern method can be further extended for disaster monitoring, crop type monitoring, etc. In addition to that, an automatic adaptive thresholding approach can make the system fully automatic and would enhance the results by protecting from the human biases and error.

- The experiment and data analysis presented in the SAR and optical information fusion part of this research is for two indicators one derived from optical and another from SAR images. Uses of two indicators to obtain the change magnitude with equal weight appeared to be effective for change detection, however, uses of several indices to obtain the change magnitude may reduce the proportion of the contribution of each indicator. That increases the change to diminish the effects, which are available in only one indicator. Theoretically, the method is feasible and applicable, but practically it may appear less effective. Thus, a proper weightage of each indicator is necessary before considering a large number of indicators.
- As far as the information fusion for change pattern detection is concerned, the basic idea of this fusion and the division of the plane are appeared to be straightforward and effective. However, the complexity is increased exponentially, as increase the number of input parameters and require to do generalization to keep track the appropriate number of classes. Therefore, direct implementation of the additional dimension of information is not recommended. However, the change classes can divide further in depth by using the information from other sources or indicators. For example, the change of vegetation to build up, or bare land, the used data sources cannot track the seasonal changes. This is possible through low frequency images such as C-band or X-band images with the coupling of L-band images. In this way, the method can be extended with arbitrarily large numbers of input bands. This allows to generate a sufficiently large amount of information in each changed phenomenon.

BIBLIOGRAPHY

[1] A. Singh, "Review Article Digital change detection techniques using remotely-sensed data," *Int. J. Remote Sens.*, vol. 10, no. 6, pp. 989–1003, Jun. 1989.

[2] U. Nations, *World Population Prospects: The 2012 Revision. United Nations, New York*. 2012.

[3] B. Mishra, M. S. Babel, and N. K. Tripathi, "Analysis of climatic variability and snow cover in the Kaligandaki River Basin, Himalaya, Nepal," *Theor. Appl. Climatol.*, Aug. 2013.

[4] R. S. Lunetta, J. F. Knight, J. Ediriwickrema, J. G. Lyon, and L. D. Worthy, "Land-cover change detection using multi-temporal MODIS NDVI data," *Remote Sens. Environ.*, vol. 105, no. 2, pp. 142–154, Nov. 2006.

[5] J. Chen, P. Gong, C. He, R. Pu, and P. Shi, "Land-Use/Land-Cover Change Detection Using Improved Change-Vector Analysis," *Photogramm. Eng. Remote Sens.*, vol. 69, no. 4, pp. 369–379, Apr. 2003.

[6] Y. Bazi, L. Bruzzone, and F. Melgani, "An Unsupervised Approach Based on the Generalized Gaussian Model to Automatic Change Detection in Multitemporal SAR Images," *IEEE Trans. Geosci. Remote Sens.*, vol. 43, no. 4, pp. 874–887, 2005.

[7] R. D. Johnson and E. S. Kasischke, "Change vector analysis: A technique for the multispectral monitoring of land cover and condition," *Int. J. Remote Sens.*, vol. 19, no. 3, pp. 411–426, Jan. 1998.

[8] W. A. Malila, “Change Vector Analysis : An Approach for Detecting Forest Changes with Landsat,” *LARS Symp.*, vol. 385, 1980.

[9] J. G. Lyon, D. Yuan, R. S. Lunetta, and C. D. Elvidge, “A Change Detection Experiment Using Vegetation Indices,” *Photogramm. Eng. Remote Sens.*, vol. 64, no. 2, pp. 143–150, 1998.

[10] M. Forkel, N. Carvalhais, J. Verbesselt, M. Mahecha, C. Neigh, and M. Reichstein, “Trend Change Detection in NDVI Time Series: Effects of Inter-Annual Variability and Methodology,” *Remote Sens.*, vol. 5, no. 5, pp. 2113–2144, May 2013.

[11] S. Berberoglu and A. Akin, “Assessing different remote sensing techniques to detect land use/cover changes in the eastern Mediterranean,” *Int. J. Appl. Earth Obs. Geoinf.*, vol. 11, no. 1, pp. 46–53, Feb. 2009.

[12] A. F. Alqurashi and L. Kumar, “Investigating the Use of Remote Sensing and GIS Techniques to Detect Land Use and Land Cover Change :,” *Adv. Remote Sens.*, vol. 2013, no. June, pp. 193–204, 2013.

[13] W. Dierking and H. Skriver, “Change detection for thematic mapping by means of airborne multitemporal polarimetric SAR imagery,” *IEEE Trans. Geosci. Remote Sens.*, vol. 40, no. 3, pp. 618–636, Mar. 2002.

[14] B. Mishra and J. Susaki, “Coupling of thresholding and region growing algorithm for change detection in SAR images,” *Prog. Electromagn. Res.*, vol. 143, no. November, pp. 519–544, 2013.

[15] M. Liao, L. Jiang, H. Lin, B. Huang, and J. Gong, “Urban Change Detection Based on Coherence and Intensity Characteristics of SAR Imagery,” *Photogramm. Eng. Remote Sens.*, vol. 74, no. 8, pp. 999–1006, Aug. 2008.

[16] Y. Ban and O. a. Yousif, “Multitemporal Spaceborne SAR Data for Urban Change Detection in China,” *IEEE J. Sel. Top. Appl. Earth Obs. Remote Sens.*, vol. 5, no. 4, pp. 1087–1094, Aug. 2012.

[17] F. M. Henderson and Z. Xia, “SAR Applications in Human Settlement Detection , Population Estimation and Urban Land Use Pattern Analysis : A Status Report,” *IEEE Trans. Geosci. Remote Sens.*, vol. 35, no. 1, pp. 79–85, 1997.

[18] E. J. M. Rignot and J. J. van Zyl, “Change detection techniques for ERS-1 SAR data,” *IEEE Trans. Geosci. Remote Sens.*, vol. 31, no. 4, pp. 896–906, Jul. 1993.

[19] F. Pacifici, S. Member, F. Del Frate, C. Solimini, and W. J. Emery, “An Innovative Neural-Net Method to Detect Temporal Changes in High-Resolution Optical Satellite Imagery,” vol. 45, no. 9, pp. 2940–2952, 2007.

[20] Y. Bazi, L. Bruzzone, and F. Melgani, “Automatic Identification of the Number and Values of Decision Thresholds in the Log-Ratio Image for Change Detection in SAR Images,” *IEEE Trans. Geosci. Remote Sens.*, vol. 3, no. 3, pp. 349–353, 2006.

[21] P. Uprety and F. Yamazaki, “Detection of Building Damage in the 2010 Haiti Earthquake Using High-Resolution Sar Intensity Images,” *J. Japan Assoc. Earthq. Eng.*, vol. 12, no. 6, pp. 21–35, 2012.

[22] Dekker R. J., “Speckle filtering in satellite SAR change detection imagery,” *Int. J. Remote Sens.*, vol. 19, no. Nov 2010, pp. 37–41, 2010.

[23] K. Amolins, Y. Zhang, and P. Dare, “Wavelet based image fusion techniques — An introduction, review and comparison,” *ISPRS J. Photogramm. Remote Sens.*, vol. 62, no. 4, pp. 249–263, Sep. 2007.

[24] Z. Dong, Z. Wang, D. Liu, B. Zhang, P. Zhao, X. Tang, and M. Jia, “SPOT5 multi-spectral (MS) and panchromatic (PAN) image fusion using an improved wavelet method based on local algorithm,” *Comput. Geosci.*, vol. 60, pp. 134–141, Oct. 2013.

[25] P. Du, S. Liu, J. Xia, and Y. Zhao, “Information fusion techniques for change detection from multi-temporal remote sensing images,” *Inf. Fusion*, vol. 14, no. 1, pp. 19–27, Jan. 2013.

[26] U. G. Gangkofner, P. S. Pradhan, and D. W. Holcomb, “Optimizing the High-Pass Filter Addition Technique for Image Fusion,” *Photogramm. Eng. Remote Sens.*, vol. 74, no. 9, pp. 1107–1118, Sep. 2008.

[27] N. Koutsias, M. Karteris, and E. Chuvieco, “The Use of Intensity-Hue-Saturation Transformation of Landsat-5 Thematic Mapper Data for Burned Land Mapping,” *Photogramm. Eng. Remote Sens.*, vol. 66, no. 7, pp. 829–839, 2000.

[28] G. Hong, Y. Zhang, and B. Mercer, “A Wavelet and IHS Integration Method to Fuse High Resolution SAR with Moderate Resolution Multispectral Images,” *Photogramm. Eng. Remote Sens.*, vol. 75, no. 10, pp. 1213–1223, Oct. 2009.

[29] G. Hong, A. Zhang, F. Zhou, and B. Brisco, “Integration of optical and synthetic aperture radar (SAR) images to differentiate grassland and alfalfa in Prairie area,” *Int. J. Appl. Earth Obs. Geoinf.*, vol. 28, pp. 12–19, May 2014.

[30] H. McNairn, C. Champagne, J. Shang, D. Holmstrom, and G. Reichert, “Integration of optical and Synthetic Aperture Radar (SAR) imagery for delivering operational annual crop inventories,” *ISPRS J. Photogramm. Remote Sens.*, vol. 64, no. 5, pp. 434–449, Sep. 2009.

[31] J. Im and J. Jensen, “A change detection model based on neighborhood correlation image analysis and decision tree classification,” *Remote Sens. Environ.*, vol. 99, no. 3, pp. 326–340, Nov. 2005.

[32] T. Freeman, “What is Imaging Radar ?,” *http://www.eorc.jaxa.jp/JERS-1/en/GFMP/SEA-2A/docs/html/imgv3.htm; Accessed on May 2014*, 2014. .

[33] J. R. Jensen, *Introductory Digital Image Processing : A Remote Sensing Perspective , Third Edition*, 3rd editio., no. August. New York: Prentice-Hall, Inc., 2004.

[34] F. Garestier, P. Dubois-fernandez, X. Dupuis, P. Paillou, and I. Hajnsek, “PolInSAR Analysis of X-Band Data Over Vegetated and Urban Areas,” *IEEE Trans. Geosci. Remote Sens.*, vol. 44, no. 2, pp. 356–364, 2006.

[35] T. Lillesand, R. W. Kiefer, J. Chipman, and S. More, *Remote Sensing and Image Interpretation , 6th Edition*, 6th Editio. New Jersey, 2008, p. 645.

[36] S. C. Liew, "Principles of remote sensing," *http://www.crisp.nus.edu.sg/~research/tutorial/rsmain.htm; Last accessed: May, 2014*, 2001. .

[37] S. W. W. Mccandless and C. R. Jackson, "Chapter 1 . Principles of Synthetic Aperture Radar," in *SAR Marine User's Manual*, 1978, pp. 1–23.

[38] K. Chureesampant and J. Susaki, "Automatic GCP Extraction of Fully," *IEEE Trans. Geosci. Remote Sens.*, vol. 52, no. 1, pp. 137–148, 2014.

[39] D. Small and Erich Meier, "SAR Geocoding," *http://www.geo.uzh.ch/en/units/rsl/research/radar-remote-sensing-sarlab/research-projects/sar-geocoding ; Last access: May 2014*, 2014. .

[40] J. S. Lee and E. Pottier, *Polarimetric Radar Imaging From Basics to Applications*, vol. 0. CRC Press, 2009.

[41] S. Jutz, S. Loekken, and European space agency, "4. polarimetric decompositions 4.1," *http//earth.eo.esa.int/polsarpro/Manuals/ ; Last accessed May 2014*, 2014.

[42] A. Freeman, S. Member, and S. L. Durden, "A Three-Component Scattering Model for Polarimetric SAR Data," *IEEE Trans. Geosci. Remote Sens.*, vol. 36, no. 3, pp. 963–973, 1998.

[43] S. R. Cloude, S. Member, and E. Pottier, “An Entropy Based Classification Scheme for Land Applications of Polarimetric SAR,” *IEEE Trans. Geosci. Remote Sens.*, vol. 35, no. 1, pp. 68–78, 1997.

[44] Y. Yamaguchi, A. Sato, W. Boerner, and L. Fellow, “Four-Component Scattering Power Decomposition With Rotation of Coherency Matrix,” *IEEE Trans. Geosci. Remote Sens.*, vol. 49, no. 6, pp. 2251–2258, 2011.

[45] W. An, Y. Cui, J. Yang, and S. Member, “Three-Component Model-Based Decomposition for Polarimetric SAR Data,” *IEEE Trans. Geosci. Remote Sens.*, vol. 48, no. 6, pp. 2732–2739, 2010.

[46] G. Moser, S. B. Serpico, and S. Member, “Generalized Minimum-Error Thresholding for Unsupervised Change Detection From SAR Amplitude Imagery,” *IEEE Trans. Geosci. Remote Sens.*, vol. 44, no. 10, pp. 2972–2982, 2006.

[47] J. Kittler and J. Illingworth, “Minimum error thresholding,” *Pattern Recognit.*, vol. 19, no. 1, pp. 41–47, 1986.

[48] N. Ramesh, J.-H. Yoo, and I. K. Sethi, “Thresholding based on histogram approximation,” *IEEE Proc.-Vis. Image Signal Proces.*, vol. 142, no. 5, pp. 271–279, 1995.

[49] F. Albregtsen, “Non-Parametric Histogram Thresholding Methods - Error Versus Relative Object Area,” in *Proc. Eighth Scandinavian Conf. Image Analysis, Tromso, Norway*, 1993, no. 2, pp. 273–280.

[50] M. Hussain, D. Chen, A. Cheng, H. Wei, and D. Stanley, “Change detection from remotely sensed images: From pixel-based to object-based approaches,” *ISPRS J. Photogramm. Remote Sens.*, vol. 80, pp. 91–106, Jun. 2013.

[51] L. Cannavacciuolo, W. Emery, G. Moser, and S. B. Serpico, “A contextual change detection method for high-resolution optical images of urban areas,” *2007 Urban Remote Sens. Jt. Event*, pp. 1–7, Apr. 2007.

[52] W. A. Yasnoff, J. K. Mui, and J. W. Bacus, “ERROR MEASURES FOR SCENE SEGMENTATION,” *Pattern Recognit.*, vol. 9, no. 4, pp. 217–321, 1977.

[53] P. Mishra, D. Singh, and Y. Yamaguchi, “BY KNOWLEDGE BASED DECISION TREE CLASSI-,” *Prog. Electromagn. Res. B*, vol. 30, no. January, pp. 47–70, 2011.

[54] R. Adams and L. Bischof, “Seeded region growing,” *IEEE Trans. Pattern Anal. Mach. Intell.*, vol. 16, no. 6, pp. 641–647, Jun. 1994.

[55] T. Anahara, M. Schmitt, and M. Tamura, “A FILTER FOR HOMOGENEOUS AREAS IN VERY HIGH RESOLUTION SAR IMAGES Department of Civil and Earth Resources Engineering , Kyoto University , Kyoto , Japan Email : yav-rax@gmail.com Photogrammetry and Remote Sensing , Technische Universitaet Muenchen (TUM),” in *IGARSS 2012*, 2012, pp. 3588–3591.

[56] R. G. Congalton, “A Review of Assessing the Accuracy of Classifications of Remotely Sensed Data,” *Remote Sens. Environ.*, vol. 46, no. October 1990, pp. 35–46, 1991.

[57] G. M. Foody, “Assessing the accuracy of land cover change with imperfect ground reference data,” *Remote Sens. Environ.*, vol. 114, no. 10, pp. 2271–2285, Oct. 2010.

[58] D. R. Helsel and R. M. Hirsch, *Statistical Methods in Water Resources*, vol. 36, no. 3. 1994, p. 323.

[59] S.-E. Park, Y. Yamaguchi, and D. Kim, “Polarimetric SAR remote sensing of the 2011 Tohoku earthquake using ALOS/PALSAR,” *Remote Sens. Environ.*, vol. 132, pp. 212–220, May 2013.

[60] a. Saepuloh, K. Koike, and M. Omura, “Applying Bayesian Decision Classification to Pi-SAR Polarimetric Data for Detailed Extraction of the Geomorphologic and Structural Features of an Active Volcano,” *IEEE Geosci. Remote Sens. Lett.*, vol. 9, no. 4, pp. 554–558, Jul. 2012.

[61] P. Coppin, I. Jonckheere, K. Nackaerts, B. Muys, and E. Lambin, “Review ArticleDigital change detection methods in ecosystem monitoring: a review,” *Int. J. Remote Sens.*, vol. 25, no. 9, pp. 1565–1596, May 2004.

[62] M. Gianinetto and P. Villa, “Mapping Hurricane Katrina’s widespread destruction in New Orleans using multisensor data and the normalized difference change detection (NDCD) technique,” *Int. J. Remote Sens.*, vol. 32, no. 7, pp. 1961–1982, Mar. 2011.

[63] N. Otsu, “A Tlreshold Selection Method from Gray-Level Histograms,” *IEEE Trans. Syst. Man, Cybern.*, vol. 9, pp. 62–66, 1979.

[64] D. J. Hayes and S. A. Sader, “Comparison of ChangeDetection Techniques for Monitoring Tropical Forest Clearing and Vegetation Regrowth in a Time Series,” *Photogramm. Eng. Remote Sens.*, vol. 67, no. 9, pp. 1067–1075, 2001.

[65] A. F. Alqurashi and L. Kumar, “Investigating the Use of Remote Sensing and GIS Techniques to Detect Land Use and Land Cover Change :,” *Adv. Remote Sens.*, vol. 2013, no. June, pp. 193–204, 2013.

[66] F. Tupin and M. Roux, “Detection of building outlines based on the fusion of SAR and optical features,” *ISPRS J. Photogramm. Remote Sens.*, vol. 58, no. 1–2, pp. 71–82, Jun. 2003.

[67] P. Du, S. Member, S. Liu, P. Gamba, K. Tan, and J. Xia, “Fusion of Difference Images for Change Detection Over Urban Areas,” *IEEE J. Sel. Top. Appl. Earth Obs. Remote Sens.*, vol. 5, no. 4, pp. 1076–1086, 2012.

[68] K. Koide and K. Koike, “Applying vegetation indices to detect high water table zones in humid warm-temperate regions using satellite remote sensing,” *Int. J. Appl. Earth Obs. Geoinf.*, vol. 19, pp. 88–103, Oct. 2012.

[69] P. Scaramuzza, E. Micijevic, and G. Chander, “SLC Gap-Filled Products Phase One Methodology,” *Available from http//landsat.usgs.gov/documents/SLC_Gap_Fill_Methodology.pdf*, pp. 1–5, 2004.

[70] M. Cunningham, “More than Just the Kappa Coefficient : A Program to Fully Characterize Inter-Rater Reliability between Two Raters,” *Stat. Data Anal.*, vol. 242, pp. 1–7, 2009.

ANNEXES

Annex 1: Statistical and mathematical method

Quantile-Quantile plot

The quantile-quantile (q-q) plot is a visual method to determine if two data sets come from the population having same distribution. It is a plot of the quantile of one data set against the quantile of another data set. If both data set comes from the same distribution, then the outcome from Q-Q plot will align with a 45-degree reference line. The following steps will build a Q-Q plot to check how well a dataset fits a particular theoretical distribution. This is the most common purpose for Q-Q plots.

- Sort the data from smallest to largest. Compute the quantiles.
- Compute n evenly spaced points on the interval (0,1) where n is the sample size. These points are the cumulative probabilities for the quantiles. They will be used to calculate the quantiles for the theoretical distribution. The most commonly used method of choosing these n evenly spaced points is K/(n+1), k = 1,……n.
- Using the probabilities chosen in Step 2, compute the corresponding theoretical quantiles for the chosen theoretical distribution.
- Plot the sorted sample quantiles against the sorted theoretical quantiles.
- If the plotted points falls close to the identity line (y =x), then it is evidence to suggest that the sample data fit the chosen theoretical distribution as well.

A detail description is presented in table A1.1.

Table A1.1 Intrepretaiton of Q-Q plot.

Description of point pattern	Possible interpretation
all but few points fall on a line	outliers in the data
left end of plot is below the reference line, the right end is above the reference line	long tails in both side
left end of plot is above the reference line, the right end is below the reference line	short tail in both side
curved pattern with slope increasing from left to right	skewed to the right
curved pattern with slope decreasing from left to right	skewed to the left
staircase pattern	discrete date

Source: http://support.sas.com/

Kappa index

The kappa coefficient is a widely used statistic for measuring the degree of reliability between raters. Therefore, Kappa index has been adopted in this study to compare the strength of agreement of MOD10A1 snow cover area with ASTER snow cover area. A kappa index is defined as [70].

Table A1.2 Kappa index explanation.

		Source B		
		Yes	No	Total
Source A	Yes	a	b	a+b
	No	c	d	c+d
	Total	a+c	b+d	N

Kappa coefficient, K is calculated as:

$$k = \frac{P_o - P_e}{1 - P_e} \quad \text{(A1.1)}$$

where $P_o = \frac{(a+d)}{N}$ and $P_e = \frac{(a+c)(a+b)+(b+d)(c+d)}{N^2}$

Interpretation: The values of kappa range from -1 to +1, with -1 indicating perfect disagreement and +1 indicating perfect agreement between the raters. Landis and Koch categorized the values of kappa to indicate the strength of this agreement is shown in A1.3 which is the widely referenced categorization [70] and is been used in this study also.

Table A1.3 Kappa index interpretation.

Kappa static	**Strength of agreement**
≤0.0	Poor
0.0-0.2	Slight
0.2-1-0.4	Fair
0.41-0.6	Moderate
0.61-0.8	Substantial
0.81-1.0	Almost Perfect

Otsu thresholding

In Otsu's method we thoroughly search for the threshold that minimizes the intra-class variance (the variance within the class), defined as a weighted sum of variances of the two classes:

$$\sigma_{\omega}^2(t) = \omega_1(t)\sigma_1^2(t) + \omega_2(t)\sigma_2^2(t) \quad \text{(A1.2)}$$

Weights are the probabilities of the two classes separated by a threshold and variances of these classes.

Algorithm

- Compute histogram and probabilities of each intensity level
- Set up initial $w_i(0)$ and $\mu_i(0)$
- Step through all possible threshold t = 1 …. Maximum intensity
- Update w_i and μ_i
- Compute $\sigma^2{}_b(t)$
- Desired threshold corresponds to the maximum $\sigma_b^2(t)$.

Annex 2: Satellite images, products and correction

ALOS satellite

ALOS satellite was lunched on January 24, 2006 and stop on 2011. It had three remote sensing instruments: the Panchromatic Remote-sensing Instrument for Stereo Mapping (PRISM), the Advanced Visible and Near Infrared Radiometer type 2 (AVNIR-2), and the Phased Array type L-band Synthetic Aperture Radar (PALSAR).

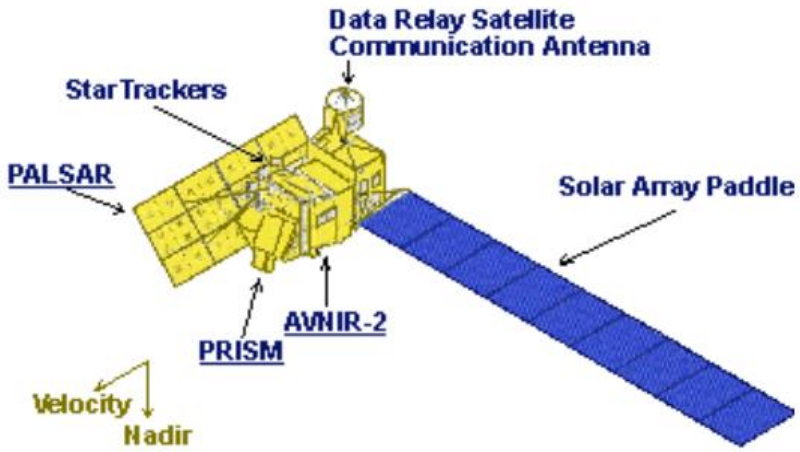

Figure A2.1 Advanced Land Observing Satellite, source: ALOS PALSAR technical outline and mission concepts.

The ALOS PALSAR sensor

The Phased Array type L-band Synthetic Aperture Radar (PALSAR) is a L-band active microwave spaceborne sensor equipped in the ALOS satellite. PALSAR is a SAR using microwave so that it can observe regardless of weather or time of the day. The acquired images are suitable for mapping on the scale of 25,000:1 without having on points of reference on the grounds (http://www.satimagingcorp.com /satellite-sensors/other-satellite-sensors/alos/).

PALSAR is a fully polarimetric instrument, operating in fine-beam mode with single polarization (HH or VV), dual polarization (HH, HV or VV, VH) or full polarimetry (HH, HV, VH, VV). It also has wide-swath ScanSAR mode with single polarization (HH or VV). The Table A2.1 shows the data acquision mode and main characteristics of PALSAR sensor.

Table A2.1 ALOS PALSAR sensor characteristics.

PALSAR acquisition mode	**Fine beam single polarization (FBS)**	**Fine beam double polarization (FBM)**	**Polarimetry (PLR)**
Central frequency	1270 MHz (L-band)		
Data rate [Mbps]	240		
PRF	1500-2500 Hz (discrete stepping)		2×FBS PRF
Off-nadir angle [deg]	9.9-50.8		9.7-26.2
Incidence angle [deg]	7.9-60.0		8-30
Swath width [km]	40-70		20-65
Bit quantization [bits]	5		3 or 5
Range sampling frequency [MHz]	32	16	16
Chirp bandwidth[MHz]	28	14	14
Polarization	HH or VV	HH, HV or VV,VH	HH, HHV, VH, VV

The PLR, FBD, and FBS modes data are available in three different processing levels (http://gds.palsar.ersdac.jspacesystems.or.jp/e/guide/pdf /U_Guide_en.pdf).

Level 1.0: This is the raw data product generated after detecting the operational errors and performing a basic processing of byte-unit arrangement etc. It is in CEOS format without radiometric corrections.

Level 1.1 product: This is derived from level 1.0 and is in single look complex (SLC) format. The following operations are done to generate level 1.1 product.

- Range compression using Fast Fourier Transformation.
- Secondary range compression using range migration compensation.
- Range migration curvature corrections
- Azimuth compression.
- Polarization calibration (for polarization data)

The number of look is one in both range and azimuth direction, and the data are in complex number format on slant range that include amplitude and phases.

Level 1.5: This is the high level product with following operation in level 1.1.

- Multi-looking processing
- Conversion from slant range to ground range.

The main difference between level 1.1 and 1.5 are multi-looking and geo-reference, additionally, geo-coded image are also available. Both geo-referenced and geo-coded images are products that are projected at 0 meter above sea level (http://gds.palsar.ersdac.jspacesystems.or.jp/e/guide/pdf/U_Guide_en.pdf).

Landsat image

Calibrated DN to Spectral Radiance Conversion

During 1G product rendering image pixels are converted to units of absolute radiance using 32 bit floating point calculations. Pixel values are then scaled to byte values prior to media output. The following equation is used to convert DN's in a 1G product back to radiance units (http://landsathandbook.gsfc.nasa.gov/):

Radiance = gain * DN + offset (A2.1)

which is also expressed as:

$$\text{Radiance} = ((L_{MAX}-L_{MIN})/(QCAL_{MAX}-QCAL_{MIN})) * (QCAL-QCAL_{MIN}) + L_{MIN} \quad \text{(A2.2)}$$

where: $QCAL_{MIN}$ = 1 (LPGS Products)
= 0 (NLAPS Products)
$QCAL_{MAX}$ = 255
QCAL = Digital Number

The LMINs and LMAXs are the spectral radiances for each band at digital numbers 0 or 1 and 255 (i.e QCALMIN, QCALMAX), respectively. LPGS (EOS Data Gateway) uses 1 for QCALMIN while NLAPS (EarthExplorer) uses 0 for QCALMIN. Other product differences exist as well. One LMIN/LMAX set exists for each gain state. These values will change slowly over time as the ETM+ detectors lose responsivity. Table A2.2 lists two sets of LMINs and LMAXs. The first set

should be used for both LPGS and NLAPS 1G products created before July 1, 2000 and the second set for 1G products created after July 1, 2000.

Table A2.2 ETM+ Spectral Radiance Range watts/(meter squared * ster * μm).

Band Number	**Before July 1, 2000**				**After July 1, 2000**			
	Low Gain		High Gain		Low Gain		High Gain	
	L_{MIN}	L_{MAX}	L_{MIN}	L_{MAX}	L_{MIN}	L_{MAX}	L_{MIN}	L_{MAX}
1	-6.2	297.5	-6.2	194.3	-6.2	293.7	-6.2	191.6
2	-6.0	303.4	-6.0	202.4	-6.4	300.9	-6.4	196.5
3	-4.5	235.5	-4.5	158.6	-5.0	234.4	-5.0	152.9
4	-4.5	235.0	-4.5	157.5	-5.1	241.1	-5.1	157.4
5	-1.0	47.70	-1.0	31.76	-1.0	47.57	-1.0	31.06
6	0.0	17.04	3.2	12.65	0.0	17.04	3.2	12.65
7	-0.35	16.60	-0.35	10.932	-0.35	16.54	-0.35	10.80
8	-5.0	244.00	-5.0	158.40	-4.7	243.1	-4.7	158.3

Radiance to Reflectance

For relatively clear Landsat scenes, a reduction in between-scene variability can be achieved through a normalization for solar irradiance by converting spectral radiance, as calculated above, to planetary reflectance or albedo. This combined surface and atmospheric reflectance of the Earth is computed with the following formula:

$$\rho_p = \frac{\pi \cdot L_\lambda \cdot d^2}{ESUN_\lambda \cdot \cos\theta_S} \qquad \text{(A2.3)}$$

where ρ_p= Unitless planetary reflectance

L_λ= Spectral radiance at the sensor's aperture

d= Earth-Sun distance in astronomical units from nautical handbook or interpolated from values listed in Table A1.2

$ESUN_\lambda$= Mean solar exoatmospheric irradiances from Table A2.3

θ_S= Solar zenith angle in degrees

Table A2.3 ETM+ Solar Spectral Irradiances.

Band	watts/(meter squared * µm)
1	1969.000
2	1840.000
3	1551.000
4	1044.000
5	225.700
7	82.07
8	1368.000

Table A2.4 Earth-sun distance in astronomical units.

Julian Day	Distance	Julian Day	Distance	Julian Day	Distance	Julian Day	Distance	Julian Day	Distance
1	.9832	74	.9945	152	1.0140	227	1.0128	305	.9925
15	.9836	91	.9993	166	1.0158	242	1.0092	319	.9892
32	.9853	106	1.0033	182	1.0167	258	1.0057	335	.9860
46	.9878	121	1.0076	196	1.0165	274	1.0011	349	.9843
60	.9909	135	1.0109	213	1.0149	288	.9972	365	.9833

Tasseled cap transformation for Landsat images

The Tasseled cap transformation in remote sensing is the conversion of the readings in a set of channels into composite values; i.e., the weighted sums of separate channel readings. One of these weighted sums measures roughly the brightness, greenness and yellowness i.e. wetness of the soil. The weight for tasseled cap transformation for Landsat 7 ETM + is presented in Table A2.5.

Table A2.5 Weights for Tasseled cap transformation of thematic mapper data.

Component	Channel 1	Channel 2	Channel 3	Channel 4	Channel 5	Channel 7
Brightness	0.3037	0.2793	0.4343	0.5585	0.5082	0.1863
Greenness	-0.2848	-0.2435	-0.5436	0.7243	0.0840	-0.1800
Wetness	0.1509	0.1793	0.3299	0.3406	-0.7112	-0.4572

PUBLICATION LIST

Full paper reviewed publications

Mishra, B., and Susaki, J. (2014*),* Fusion of L-band polarimetric data for urban land cover change detection, *Journal of Selected Topics in Applied Earth Observations and Remote Sensing* [Accepted].

Mishra, B., and Susaki, J. (2014). Optical and SAR information fusion for automatic multi-class change detection, *ISPRS Annals of the Photogrammetry, Remote Sensing and Spatial Information Sciences,* Vol. II-7, 2014

Mishra, B., and Susaki, J. (2013). Coupling of thresholding and region growing algorithm for change detection in SAR images, *Progress in Electromagnetic Researches*, Vol. 143, pp. 519-544.

Mishra, B., and Susaki, J. (2013). Unsupervised change detection in an Urban environment using multitemporal PolSAR images, *Proceeding of JURSE April 21-23-Sao Paulo- Brazil,* pp.45-48 [oral].

Mishra, B., and Susaki, J. (2012). Generation of pseudo-fully polarimetric data from dual polarimetric data for land cover classification, *Proceeding of CVRS Dec. 16-18 Xamen China*, 978-1-4673-1274-5/12 IEEE [oral].

Abstract reviewed publications

Mishra, B., and Susaki, J. (2014). SAR and optical data fusion for land use and cover change detection, *Proceedings of the International Geoscience and Remote Sensing Symposium (IGARSS)* 2014, July 13-18, Quebec, Canada, pp. 4691-4694 [oral].

Mishra, B., and Susaki, J. (2013*),* Urban and suburb change detection using multi-temporal polarimetric SAR images, *Proceeding of ACRS October 20-24-Bali, Indonesia*, pp. SC01-55 – SC01-62, 2013 [poster].

Mishra, B., and Susaki, J. (2013). Automatic thresholding for land cover change detection in SAR images, Proceedings of the International Geoscience and Remote Sensing Symposium (IGARSS) 2013, July 21-26, Melbourne- Australia, pp.3347-3350 [oral].

Mishra, B., and Susaki, J. (2012). Land cover classification comparisons among dual polarimetric, pseudo-fully polarimetric and fully polarimetric SAR imagery, *Proceeding of SPIE,* Vol. 8524, 852408 [oral].